Faculty of Electrical Engineering, Mathematics and Computer Science

Master Thesis

Time-Domain Electromagnetic Leaky Waves Radiation from a Long Slot

Author: Junhong Gu (ID 5245087)

Supervisor: Ioan E. Lager

Delft University of Technology

TeraHertz Sensing Group

Data: October 15, 2022

Acknowledgement

I'd like to thank Prof. Dr. Andrea Neto, Prof. Dr. Nuria Llombart, and Dr. Daniele Cavallo for providing me with the best education during my first year at TUDelft. The knowledge you have imparted to me has greatly stimulated my interest in studying at the TeraHertz Sensing Group.

I would like to thank Prof. Dr. Andrea Neto for offering me the precious chance to do my thesis project in our wonderful group.

I would also like to thank my colleagues in the TeraHertz Sensing Group, who are really excellent and enthusiastic people. It was my pleasure and honour to work with you in the past year.

My most sincere gratitude goes to my supervisor and mentor, Prof. Dr. Ioan E. Lager. During the year I spent with you, I deeply felt your serious and responsible attitude towards academic work. You are humorous, gentle, and elegant. When I am negligent and slack, you will correct my attitude in time, and when I have a breakthrough, you are generous with praise and encouragement. You are not only my academic mentor but also my life mentor.

My sincere thanks also go to my parents, who worked really hard to afford my tuition fee. It was your silent support behind me that made me. I feel very guilty about my immaturity and not being responsible enough over the past several years. I really hope that in the near future, I can truly learn to take care of my family and reduce your burden.

Last but not least, I want to say something to my ex-girlfriend, Katherine Lu. Qiaoyun, thank you for your company over the past year. During my time with you, I learned to control my emotions and how to live a good life. Although we chose different paths and different lives in the end, your existence still left an unforgettable memory in my mind. Thank you and I wish you all the best in your future life.

Contents

Chapter 1

Introduction

1.1 Background

Over the second half of the 20th century, one of the most active fields of study in microwave engineering was leaky waves [1]. They have been demonstrated to predominate the near-field of a number of open wave-guiding structures, which is very important for adjusting their radiation, guidance, and filtering characteristics. Elegant theoretical analyses and profound physical discoveries in this field, produced in an era with constrained computer resources, offer a basic scientific legacy that is still highly applicable in the current engineering society and beyond. Regarding this, the importance of leaky-wave ideas has recently gained more attention from a wider scientific community, including physics and optical societies. Since the 1940s, when a rectangular waveguide with slots was developed, leaky-wave antennas (LWAs) have been in use [2]. Since then, the sector has continued to advance steadily, with current discoveries focused in particular on planar LWAs, which have the benefit of being low profile and simple to manufacture [3]. Since entering the 21st century, with the development of terahertz technology and the requirement for a high data rate, the leaky-lens antenna (LLA) has gradually gained its reputation with its numerous applications. Under such circumstances, unlike the majority of the studies on LWs, TD research on the LW phenomena in the planarly-fed LLAs has become increasingly more important.

1.2 State of the Art

1.2.1 Leaky-waves generalities

It is well known that the radiation from a continuous longitudinal slot in a uniform lossless waveguide may commonly be characterized by a travelling wave with a complex propagation constant. This travelling wave moves more quickly than the speed of light through the waveguide and attenuates as it does so, suggesting a steady loss of energy. Those waves are known as *leaky waves* if they exhibit this particular tendency [4]. The basic property of the FD leaky wave concept was properly explained in [5], and later in [1] and [6]. Since the concept of leaky wave came into being, it has been almost a pure frequency domain concept for decades, and thus the majority of the LW research is carried out in the FD.

It should be highlighted that [7], [8], [9] did a frequency-domain (FD) study, much like the great bulk of the literature on leaky-wave (LW) radiation, a decision based on the usefulness of the relevant analytic tools. However, the suitability of this route may provide issues for ultra-high data rate systems: Unavoidable extraordinarily high-frequency digital modulation of the carrier, regardless of code optimization [10], raises severe questions regarding the validity of the steady-state (FD) assumption. The agile beam scanning will exacerbate these issues in multi-user situations, with the networks of unmanned aerial vehicles (UAV) discussed in [11] serving as an extreme case.

Based on the FD study of the LW, many of its applications in AE have emerged one after another in the past several decades. Among them, the design of radiating systems (leaky wave antenna), as well as the explanation and interpretation of a number of electromagnetic spectrum phenomena, including Cherenkov radiation, Wood's anomalies, and extraordinary optical transmission, particularly prominent [1]. For example, [4] and [12] interpret the leaky-wave antenna designs for the rectangular waveguide and circular waveguide, respectively, based on a microwave network approach. Furthermore, the theoretical basis of complex guided modes, developed in the mid-20th century, may be linked to systematic research on leaky-wave antennas. Since then, the technology has been advancing steadily, and leaky-wave antennas have gained popularity in the microwave spectrum due to their appealing qualities, particularly the ability to realize highly directional antennas without the requirement for intricate feeding networks typical of phased arrays. For the convenience of the readers, quite a few examples of leaky-wave antennas and the corresponding design can be found in [13–16].

Terahertz technology is widely regarded as crucial to both current and prospective (6G) networks due to the increasing demand for ultra-high data throughput and low latency that propels the development of wireless communication [10]. Any strategy's viability at the channel level depends on the availability of powerful radiators. In this regard, one very special type of leaky-wave antenna, namely the planarly-fed, leaky-lens antenna

(LLA), described in [7,17], has solidified its position as the standard for (sub-)terahertz, non-dispersive applications, with a wide range of implementations of this concept [18–28] convincingly confirming its unquestionable perfection.

1.2.2 Time-domain analyses of the leaky-wave-type propagation

Compared with the FD strategy, TD research has the added advantage of establishing precise, comprehensible limits on the applicability of FD techniques. The existing literature is quite limited when it comes to the time-domain (TD) investigation of LW phenomena [29]: The authors of [30] examined specific joint-transform strategies to convert the terms of a hybrid ray-mode series expansion with regard to the horizontal-electric-dipole excited fields within a grounded slab. [31] then uses a sophisticated analytical strategy to substitute a branch-cut integral with a sum of pole-related residue contributions on a "non-physically acceptable" Riemann sheet. The analysis of both line- and point-source excited TD LWs in a grounded slab is done in great depth in [32], which also follows a similar line of thought. The discussion in [33] is also highly instructive in this regard, identifying TD LWs in the Laplace-transform domain expression for the 1-D plane-wave field reflected on a grounded slab and discussing them in the context of line-source-excited HW occurrences.

1.2.3 Time-domain investigations of relevance for the analysis of LLAs

LLAs require the study of slot propagation, and in [29], the author looked at certain LW radiation-related configurations including an electric-current excited infinite slot, and developed relationships between normal LW properties and the pseudo-LW (pLW) phenomena. In that paper, a causality-preserving interpretation of the electromagnetic (EM) leaky-wave (LW) propagation in both space and time was put forward for the first time. However, that study only examined electromagnetic (EM) problems that are amenable to an analytical approach in order to concentrate on conceptual explanations. It then purposefully left out two of the LLAs' distinctive structures that don't appear to lend themselves to an analytical TD treatment: the gap-fed slot at the air-dielectric interface and the one with an extra air gap on top of the slot. Functionally, the LLA uses radiation from a gap-fed slot that is situated at an air-dielectric interface; [8], [9] provide in-depth analyses of this canonic structure, while the key accomplishment of [7] was to significantly improve the beam focusing by introducing an air gap between the slot and the dielectric half-space. Therefore, the relevant investigations into this topic must be supplemented by purely numerical studies.

1.2.4 Computational EM in EM research

Commercial computational electromagnetics (CEM) simulation software is widely used in EM research. A very recent phenomenon is that the availability and applicability of simulation tools have profoundly altered how research is conducted. Commercial CEM solutions can act as a virtual lab bench for scientific investigation or a quick optimization tool for engineering design challenges, so the users can profit greatly from their broad usage [[34]]. CEM problems require high numerical precision computations [35], resulting in high requirements for the accuracy of the EM simulation model. In this scenario, the evaluation of an EM simulation model starts to play a more and more essential role in the field of CEM. There is even an IEEE standard for validating CEM computer modelling and simulation in [36], which reflects the importance of assessing the numerical tools.

Currently, commercial software tools are widely used in antenna engineering (AE), and numerical validations using these tools have nearly become a must for publishing results. The standard validation instruments among them are CST Studio Suite ® and Ansys HFSS (HFSS), with the usage of other software tools being restricted to specialized fields. Even well-supported (semi-)analytical frameworks are sometimes only accepted inasmuch as they are supported by some numerical validation using one of these two packages since they play such a prominent role in the field. For example, a numerical simulation tool for a 2D wide slot antenna with a dielectric layer built in the CST Studio environment, written in [37], successfully validates the analytical results provided in [38].

TD simulations require, in general, more care. To begin with, TD explorations must ensure strict causality (see the argument in [39]). The quantum theoretical concept of locality (or microcausality) stands in stark contrast to causality as it is explained in [40]. In contrast to the space-like phenomena seen in quantum physics, causality is a unique attribute of time-like events (with classical EM clearly coming within this category) [40]. Furthermore, from a theoretical perspective, causality is essential to proving the uniqueness of the EM initial value problem, and implementing the reciprocity theorem (another fundamental EM result) to the case of unbounded domains again necessitates the use of causal sources with bounded spatial support [41]. Surprisingly, standard TD excitations in commercial software, in general, and in CST Studio, in particular, are derived from the Gaussian pulse shape, which is non-causal, and thus it is important to import some user-defined causal excitations before conducting any EM simulation.

Among all causal excitations, two families of model pulses—power-exponential (PE) and windowed-power (WP)—with an implicitly causal behaviour are carefully studied in [42] and [43]. Among them, [42] highlighted the theoretical and practical advantages of employing these pulses and convincingly proved their superiority to other excitations that are frequently employed in antenna systems. Examples of PE pulse applications can be found in [38] and [44]. Additionally, [45] interprets not only the WP pulse but

the windowed families of pulses, which have finite temporal support compared with the PE pulses, even more precisely. In conclusion, these useful TD causal pulses greatly facilitate EM simulations.

Moreover, subtle details in the signatures often require careful meshing and time sampling, and the even bigger problem is that certain boundary conditions (BCs) setups are not effective in commercial software. For example, periodic BCs are extremely popular in FD but make less sense in TD experiments. Conversely, TD studies also offer specific opportunities, e.g. performing time-gated simulations using time-windowed excitations in conjunction with sufficiently large domains of computation (see [45]) – an approach emulating genuinely reflectionless EM radiation.

1.3 Problem Formulation

The primary goal of this thesis is to infer a time domain leaky wave counterpart of the frequency domain leaky wave, and in order to achieve that, some sub-problems listed below have to be solved. It will focus on a few technical aspects of time-domain (TD) electromagnetic (EM) analysis, and the discussion will be limited to CST Studio simulations; however, the derived findings may be applied to HFSS. First, the numerical tools for a wide slot antenna with a dielectric layer should be identified and validated. Then, the EM problems in a gap-fed long slot at an air-dielectric interface (Configuration A) and in the one containing an extra air gap (Configuration B), shown in Fig. 1.1 should be solved.

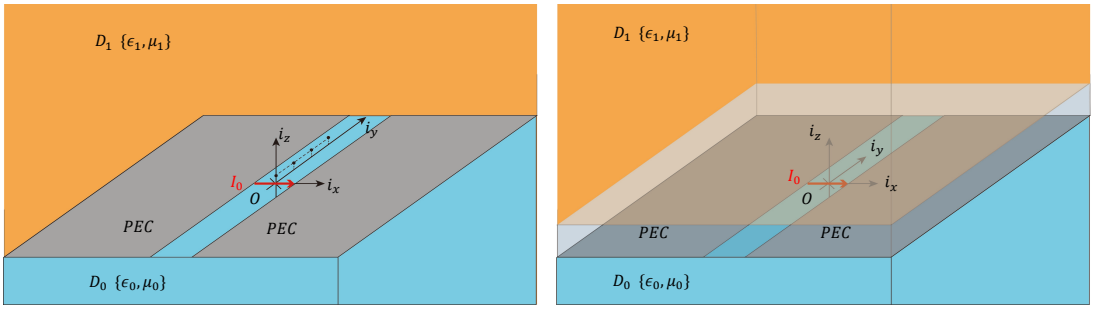

(a) Configuration A

(b) Configuration B

Figure 1.1: Two different gap-fed long slot configurations of LLAs.

In the first part of the thesis, the analytical results of the 2D wide slot antenna with a dielectric layer proposed in [38] should be validated numerically. Despite the simplicity of the model configuration, the building of the simulation tool in CST Studio is not trivial at all. The difficulty of this problem lies in how to set the proper boundary conditions and how to reasonably simulate the field radiation results of the 2D model

in the CST 3D environment. Finally, the design of the CST simulation tool for the 2D wide slot antenna with a dielectric layer should set a solid foundation for the numerical analysis of the 3D long slot configurations.

In the body parts of this thesis, the work in [29] will be supplemented by a thorough TD EM numerical analysis of these layouts, which particularly relates pLW-type properties to the LLAs' operation principles. A special focus will be placed on thoroughly verifying all used equipment throughout the procedure. The setups and the primary simulation options will be introduced at the beginning of the account. The next step will be to show that, in the case of Configuration A, the simulated TD signatures and the impulse response are practically identical. Then, the study of the field propagation in planes longitudinal and transverse to it for the two designs will be covered in the next two following chapters. Conclusions will be given at the end of the thesis.

1.4 Outline of the Thesis

Chapter 1 provides the background information, a brief introduction of the state of the art, a problem statement section and the thesis outline.

Chapter 2 introduces some prerequisites of all the studies in this thesis.

Chapter 3 covers the introduction of the 2D wide slot configuration and the analytical results obtained in MATLAB and provides the numerical validation of those results via CST Microwave Studio ®.

Chapter 4 first introduces the building of a CST simulation tool which directly generates the impulse response (time-domain Green's function) for a 3D long-slot configuration between a dielectric and a vacuum half-space at selected observation points. Moreover, in this chapter, feature analysis was performed in both transverse and longitudinal cross-sections to search for the time domain leaky wave. The results of the feature analysis include the evidence of the time domain leaky wave, the mapping of the time domain signature on the corresponding longitudinal snapshots, as well as the observation and evidence of the ringing caused by pulses of comparable or narrower spatial extent compared with the slot width and their effect on the radiated field, which is highly relevant when trains of pulses are studied.

Chapter 5 performs the feature analysis for a different configuration, in which there is an extra air gap between the dielectric half-space and the slot. Similarly, the time domain wave constituents are studied thoroughly at longitudinal and transverse cross-sections. Furthermore, this chapter also contains a comparison of results with the previous chapter.

Chapter 6 finishes the thesis by drawing some conclusions and providing some suggestions for future work.

Chapter 2

Prerequisites

2.1 Notation Conventions

The Cartesian coordinate system applied in the configurations that appear in this thesis is written as $\{x_1,\, x_2,\, x_3\}$, or sometimes $\{\boldsymbol{i}_x,\, \boldsymbol{i}_y,\, \boldsymbol{i}_z\}$ or simply $\{x,\, y,\, z\}$. The partial differentiation of x_m is denoted by ∂_m, while the time coordinate and its first-order derivative are denoted by t and ∂_t.

The permittivity and permeability of the free-space and dielectric material are written as

$$\{\varepsilon, \mu\} = \begin{cases} \{\varepsilon_0, \mu_0\} & \text{in} \quad \mathcal{D}_0 \\ \{\varepsilon_1, \mu_0\} & \text{in} \quad \mathcal{D}_1 \end{cases} \tag{2.1}$$

or

$$\{\varepsilon, \mu\} = \begin{cases} \{\varepsilon_0, \mu_0\} & \text{in} \quad \mathcal{D}_0 \\ \{\varepsilon_0 \varepsilon_{\mathrm{r}}, \mu_0\} & \text{in} \quad \mathcal{D}_1 \end{cases} \tag{2.2}$$

in which $\mathcal{D}_0$ and $\mathcal{D}_1$ represent the domain of free-space and dielectric material, respectively, and ε_r represents the dielectric constant. The wave speeds in the vacuum and the dielectric material are denoted by c_0 and $c_1 = c_0/\sqrt{\varepsilon_{\mathrm{r}}}$. The wave impedance of the plane wave in the free space and the dielectric slab is $Z_0 = \sqrt{\frac{\mu_0}{\varepsilon_0}}$ and $Z_1 = \sqrt{\frac{\mu_0}{\varepsilon_1}}$.

2.2 Examined Quantities

The examined field quantities in this thesis are $\boldsymbol{E}(\boldsymbol{r},t)$ and $\boldsymbol{H}(\boldsymbol{r},t)$, in which $\boldsymbol{r} = x\boldsymbol{i}_x + y\boldsymbol{i}_y + z\boldsymbol{i}_z$. Those field quantities obey the TD Maxwell's equation listed in Eq. (2.3) to Eq. (2.6)

$$\nabla \times \boldsymbol{E} = -\frac{1}{c}\frac{\partial \boldsymbol{B}}{\partial t} \tag{2.3}$$

$$\nabla \cdot \boldsymbol{B} = 0 \tag{2.4}$$

$$\nabla \times \boldsymbol{B} = \frac{1}{c}\frac{\partial \boldsymbol{E}}{\partial t} + \frac{4\pi}{c}\boldsymbol{j} \tag{2.5}$$

$$\nabla \cdot \boldsymbol{E} = 4\pi\rho \tag{2.6}$$

with $\boldsymbol{E}$ and $\boldsymbol{B}$ representing the vectors of the electric field strength and the magnetic flux density, $\boldsymbol{j}$ denoting the volume electric current density and ρ symbolizing the volume electric charge density. Note that, the relation between the magnetic field strength $\boldsymbol{H}$ and the magnetic flux density $\boldsymbol{B}$ is expressed as $\boldsymbol{B} = \mu_0\boldsymbol{H}$.

The interface boundary conditions (BCs) of the electric field $\boldsymbol{E}$ and the magnetic field $\boldsymbol{H}$ require that

$$\lim_{\boldsymbol{n}\downarrow d} \boldsymbol{n} \times \{\boldsymbol{E}, \boldsymbol{H}\} = \lim_{\boldsymbol{n}\uparrow d} \boldsymbol{n} \times \{\boldsymbol{E}, \boldsymbol{H}\} \quad \text{for all } t \text{ and points at the interface} \tag{2.7}$$

in which $\boldsymbol{n}$ denotes the unit vector along the normal to the dielectric-air interface, and $\boldsymbol{n} \downarrow d$ means and $\boldsymbol{n} \uparrow d$ mean to be below or above the interface, respectively.

2.3 Spectral Representation of the Field Quantities

The analytical time domain expressions of the field quantities can be analyzed in the spectral domain by employing the modified Cagniard method (the Cagniard-De Hoop method), which first applies a unilateral Laplace transform [38, 44, 46, 47] with respect to the time of the kind

$$F(s) = \int_{t=0}^{\infty} \exp(-st) f(t) \mathrm{d}t \tag{2.8}$$

and then a spatial Fourier transform [38, 44, 46, 47] with respect to the spatial extent x on top of the spectral domain expression $F(s)$ via

$$\mathscr{F}(\alpha, y, s) = \int_{-\infty}^{\infty} \exp(is\alpha x) F(x, y, s) \mathrm{d}x \tag{2.9}$$

in which $\alpha = -ip$ and p is a complex variable in the p-plane. After the unilateral Laplace transform and spatial Fourier transform, the time domain field quantities are transformed into the so-called slowness domain, in which a solution can be found.

After appropriate integral transformations and field representations are introduced, the solution is expressed in terms of generalized ray constituents successively arriving at a certain observation point, whose space-time equivalents are created by applying the Cagniard-De Hoop technique [46]. Note that this technique was originally developed for seismic problems and later expanded to the EM field.

The spectral-domain analysis of the EM propagation allows establishing two type of causal wave constituents: *body wave* and *head wave*. For homogeneous isotropic subdomains, the only wave constituent is the *body wave* (BW), which always exists. In this case, the time-domain Green's function can be easily implemented. However, for a subdomain with stratification, another ray constituent called *head wave* (HW) starts to arise in a certain bounded region, in which the incident angle ϑ is larger than the critical refraction angle ϑ_c, and in this scenario, there is no simple expression of the time-domain Green's function.

Physically, the head waves correspond to the arrival of the first disturbance at a certain point of observation located in that bounded region because it propagates along the interface at the wave speed of the optically rarer medium and forms a cone-shaped wavefront in the half-space of the optically denser medium, while the body wave is the last to arrive. Note that the details of the Cagniard-De Hoop (CdH) method and its relation with the BW and HW can be found in Appendix A.

2.4 Causality and Excitations

Since TD research requires strict causality, all the excitation signals applied in this thesis are causal. Those excitations consist of a power exponential (PE) pulse, a windowed power (WP) pulse and a unipolar triangular pulse.

The power exponential (PE) pulse [38, 44] is characterised by

$$V_0(t) = V_{\max}(t/t_r)^{\nu} \exp[-\nu(t/t_r - 1)] H(t) \tag{2.10}$$

with $\nu = 0, 1, 2, ...$, where $V_{\max}$ represents the *pulse amplitude*, ν the *rising exponent* of the pulse, t_r the *pulse rise time*, and $H(t)$ the *Heaviside unit step function*.

The expression of the windowed power (WP) pulse [42, 45] is given by

$$V_0(t) = V_{\max} t'^{\nu} (2 - t')^{\nu} H(t') H(2 - t') \tag{2.11}$$

with $\nu = 0, 1, 2, ...$, in which $V_{\max}$ represents the *pulse amplitude*, ν the *rising exponent* of the pulse, $t' = t/t_r$ the normalized time coordinate, and $H(t)$ the *Heaviside unit step function*, with t_r being the *pulse rise time*. Different from the PE pulse, which has a infinite tail, the WP pulse has a finite temporal support $t_w = 2t_r$, and t_w is also called *pulse time width*.

The triangular pulse [48] is written as

$$V_0(t)/V_{\max} = \begin{cases} 0, & t < 0 \\ t', & 0 \le t \le t_r \\ 2 - t', & t_r < t \le t_w \\ 0, & t > t_w \end{cases} \tag{2.12}$$

in which $V_{\max}$ represents the *pulse amplitude*, t_w corresponds to the *pulse time width* or the *base length*, $t_r = t_w/2$ denotes the *pulse rise time*, and $t' = t/t_r = 2t/t_w$ refers to the normalized time coordinate. More information about the causal feeding pulses is put in Appendix B.

Chapter 3

2D Wide Slot Configuration

3.1 Analytical Model

The examined configuration introduced in this section that was first mentioned in [38], is composed of a wide slot, a dielectric slab $\mathcal{D}_1$ and a vacuum layer $\mathcal{D}_0$ on top of it. As is shown in Fig. 3.1, position is specified with respect to a Cartesian reference frame $\{x_1, x_2, x_3\}$ with origin O and the observation points from A to D are located at the dielectric-air interface. Point A is exactly on top of the slot, so no head wave can reach it; Point B can only receive the head wave from the left edge of the slot; Point C and D can receive the head wave from both edges. The width of the slot and the thickness of the dielectric slab are denoted by w and d, respectively. The configuration contains an unbounded perfectly electrically conducting screen $\mathcal{S} = \{(-\infty < x_1 < -w/2) \cup (w/2 < x_1 < \infty), -\infty < x_2 < \infty, x_3 = 0\}$, a feeding aperture $\mathcal{A} = \{-w/2 < x_1 < w/2, -\infty < x_2 < \infty, x_3 = 0\}$, a covering dielectric layer $\mathcal{D}_1 = \{-\infty < x_1 < \infty, -\infty < x_2 < \infty, 0 < x_3 < d\}$, and a vacuum half-space $\mathcal{D}_0 = \{-\infty < x_1 < \infty, -\infty < x_2 < \infty, d < x_3 < \infty\}$. The infinite embedding is taken to be the vacuum half-space with permittivity ε_0, permeability μ_0 and wavespeed $c_0 = (\varepsilon_0\mu_0)^{-1/2}$, while the dielectric slab is characterised by its relative permittivity ε_r and relative permeability μ_r. The experiments will first focus on the power-exponential (PE) [38] and then windowed-power (WP) [42] families of pulses, with $\nu \geq 2$ being their integer raising power, and $t_\mathrm{r} > 0$ their pulse rise-time. The configuration is excited via a slot in the PEC along which $E_x(t)$ has a prescribed, power exponential (PE) pulse-shaped temporal behaviour. The ensuing EM problem is two-dimensional (2D) and lends itself to a semi-analytic solution using the Cagniard-de Hoop (C-dH) method [47], thanks to plane-parallel invariance in the y-direction. The relevant information about the Cagniard-de Hoop (C-dH) method and the power exponential pulse can be found in Appendix A and B, respectively.

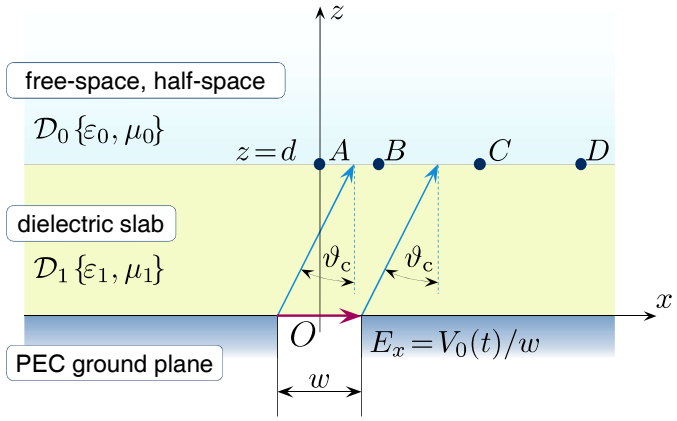

Figure 3.1: Configuration in the case of the "wide slot" problem. Location of observation points: A $\leftrightarrow x = 0$, B $\leftrightarrow x = d$, C $\leftrightarrow x = 3d$ and $D \leftrightarrow x = 5d$.

3.2 Analytical Results

The analytical signatures at the dielectric-air interface obtained from MATLAB serve as the reference signatures and are later compared to the CST simulated signatures to verify the feasibility of the CST model. Fig. 3.2 to Fig. 3.5 provide the normalized field components E_{x} and H_{y} at observation points A to D. For the convenience of the readers, the detailed analysis of those analytical results can be found in [38], and the time domain expressions of different wave constituents following the Cagniard-de Hoop (C-dH) method and corresponding MATLAB scripts can be found in Appendix C.

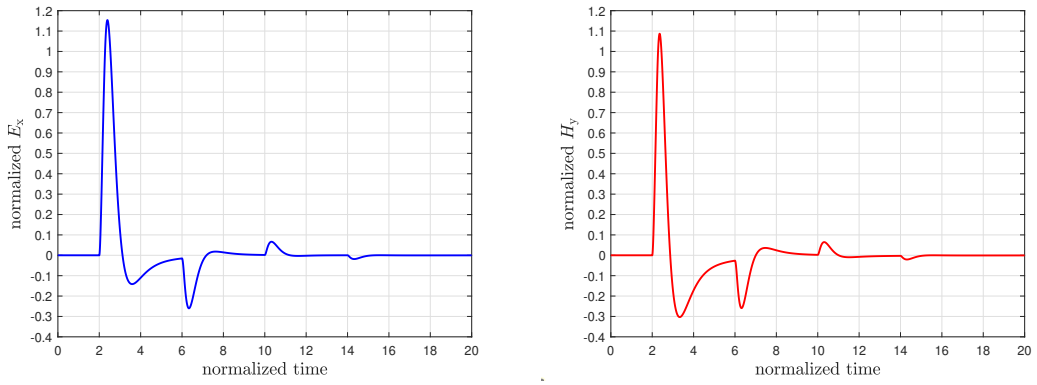

(a) normalized E_{x} (b) normalized H_{y}

Figure 3.2: Reference signatures at observation point A.

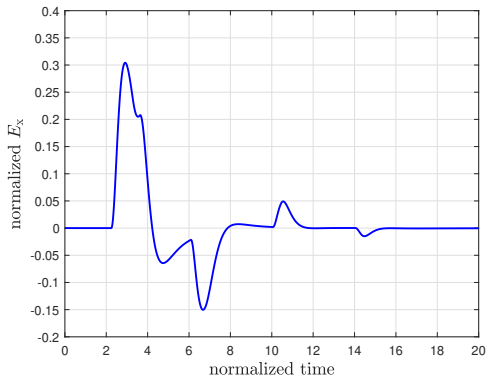

(a) normalized E_{x}

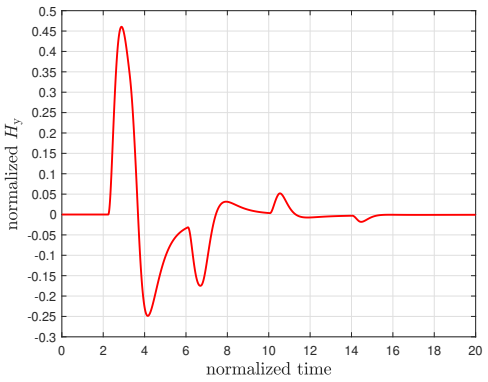

(b) normalized H_{y}

Figure 3.3: Reference signatures at observation point B.

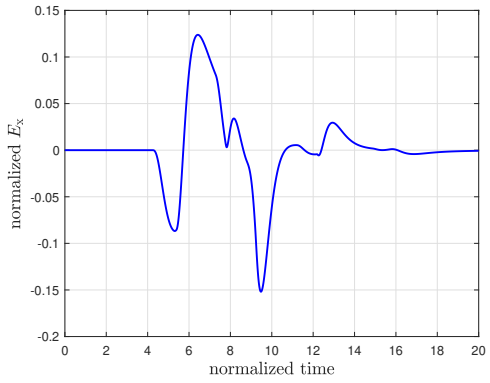

(a) normalized E_{x}

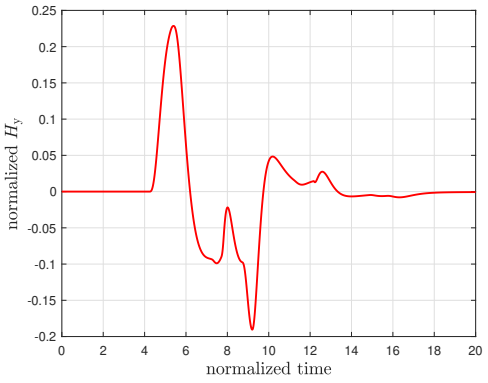

(b) normalized H_{y}

Figure 3.4: Reference signatures at observation point C.

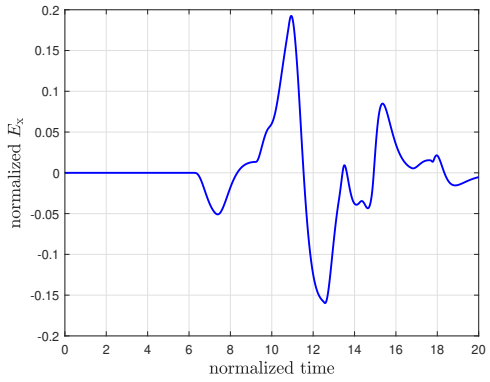

(a) normalized E_{x}

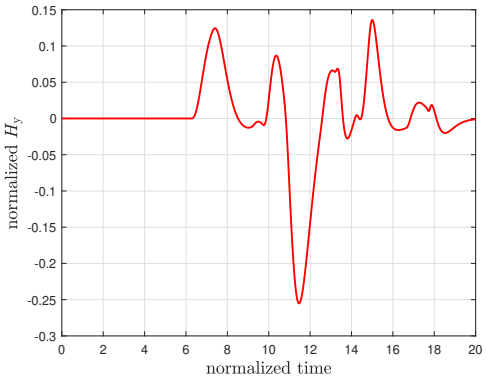

(b) normalized H_{y}

Figure 3.5: Reference signatures at observation point D.

3.3 Numerical Validation via CST Microwave Studio ®

This section will concentrate on the numerical validation of the pulsed EM field radiating from a wide slot antenna with a dielectric layer, whose analytical results has been well explained in the last section and more exhaustively in [38]. Note that the contents in this section are restricted to CST Studio simulations and can be found in [37]. After motivating the need for this study and introducing some simulation choices, results and analysis will be provided, and finally a brief summary of conclusions will be given at the end of this section.

3.3.1 Motivation

In the context of the increasing importance of CEM simulation, the numerical validation of theoretical models has also become increasingly more important. A pivotal source of concern in TD EM simulations refers to excitation. Even when resorting to strictly causal pulse-shapes, CST Studio raises some (im)practicality issues: the standard Dirichlet and Neumann BCs are not available. This spatial meshing results, in turn, in extremely small time steps, as required by the Courant-Friedrichs-Lewy condition [49] – such a temporal discretisation is often an overkill for the problem at hand. Despite this, these limitations can still be sidestepped by making use of the facility that is readily available in CST studio.

3.3.2 Simulation Choices

As mentioned in the introduction chapter, the default excitation signal in CST Microwave Studio ® is a non-causal Gaussian pulse. However, time-domain research requires strict causality [39] and, therefore, a causal time-domain excitation pulse has to be defined. The one used in [38] is a power exponential (PE) pulse, which provides a convenient mathematical model to accommodate parameters including the pulse amplitude, rising exponent, and pulse rise time. Fig. 3.6 gives an example of how the shape of the PE pulses changes when ν equals to different values. Note that for all the results that will be shown in this section, the PE pulse has a rising exponent $\nu = 2$, and a pulse rise time t_r being selected such that $c_0 t_\mathrm{w}/d = 0.9236$. Additionally, the domain of computation was chosen as extremely thin in the y-direction, with magnetic-wall boundary conditions on the two faces in the y direction ensuring the 2D character of the field, while the mesh size and was selected to be reasonably small to guarantee accurate simulations.

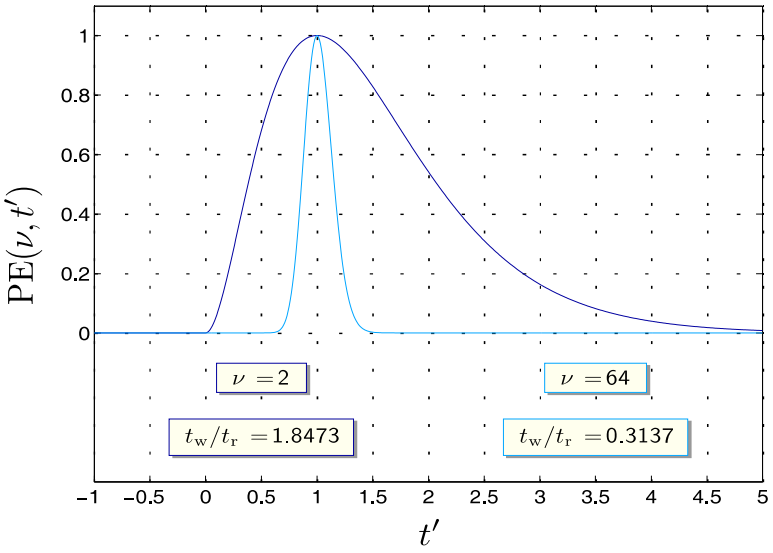

Figure 3.6: Causal excitation: power exponential (PE) pulse.

Although the configuration depicted in Fig. 3.1 appears to be simple, it is not easy to be simulated in CST Microwave Studio ®. Since the Dirichlet Boundary Conditions are not available, one may consider using a waveguide port to form a parallel-plate waveguide excitation. However, this is not an option because a parallel-plate waveguide has a non-uniform field distribution in the x direction with corner singularities. Apart from that, the waveguide aperture has a certain admittance and is penetrable, while the reference model leaves an impenetrable PEC wall after the exciting pulse is radiated. Another idea is to place a magnetic current sheet above the PEC, according to the equivalence theorem. However, a time-domain magnetic current sheet cannot be implemented in CST Microwave Studio ®.

The solution turns out to be a *discrete port*, which is readily available in CST studio. The discrete port model that will be shown in Fig. 3.7 in the next chapter, has clear advantages over the waveguide port model for the following reasons. First, when a single discrete port is applied to mimic the electric field at the aperture, the thickness of the model in the y direction should be infinitely small to get as close to the 2D analytical model as possible. In this case, the model size is greatly reduced, and so is the calculation time. Meanwhile, the smaller model size makes it possible to apply denser meshes, which greatly improves the simulation accuracy. Second, in this model, the wide slot antenna is replaced by a thin PEC wall, and since the discrete voltage port is put just on top of it, the wave coming from the dielectric-air interface can be fully reflected at the aperture, which properly mimics the Dirichlet Boundary Condition.

3.3.3 Results and Analysis

The result analysis consists of the comparisons between components of some reference electric $E(\boldsymbol{r}, t)$ or magnetic $H(\boldsymbol{r}, t)$ field signatures and their corresponding CST simulated counterparts, with $\boldsymbol{r} = x\boldsymbol{i}_x + y\boldsymbol{i}_y + z\boldsymbol{i}_z$ and t the time coordinate. All plots will be created for normalized data, with the reference values serving as the normalization quantity and the CST Studio signatures aligned to the reference so that the maximum absolute values are equal. The time coordinate will also be normalised and the two types of signatures will be time-aligned within the interval $\mathcal{T}$ over which both of them are available (with t' of the reference signatures being taken as the leading quantity). The deviation between signatures will be evaluated based on the global replication error

$$\mathrm{Err}_{\%} = \frac{\int_{\mathcal{T}} |V_{\mathrm{norm}}(t') - \tilde{V}_{\mathrm{norm}}(t')| \mathrm{d}t'}{\int_{\mathcal{T}} |V_{\mathrm{norm}}(t')| \mathrm{d}t'} \times 100 \tag{3.1}$$

in which $V_{\mathrm{norm}}(t')$ denotes the normalized reference quantity (analytical value), and $\tilde{V}_{\mathrm{norm}}(t')$ the normalized replicated quantity (CST simulated value).

The comparisons between the reference field components $E(r, t)$ and $H(r, t)$ and the CST simulated ones are shown in Fig. 3.8 to Fig. 3.11. The signatures correspond to the normalised $E_{\mathrm{x}} w/V_{\max}$ and $Z_0 H_{\mathrm{y}} w/V_{\max}$ field quantities and $t = c_0 t/d$ at observation points A, B, C and D.

The plots demonstrate the excellent replication of even the small details in the examined signatures. At point A and C, the normalized replication errors are all around 5%, while at point B, the value even drops to about 3%. At point D, the deviation increases a little bit, especially for the magnetic field, but the normalized replication error still remains low level. Note that the global errors calculated via equation (3.1) for all observation points are given in Table 3.1, with the largest replication error being of 8.5%.

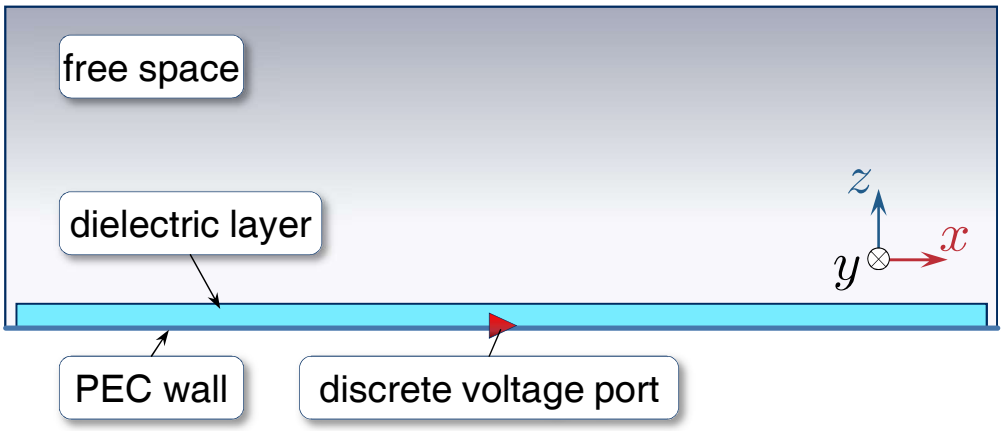

Figure 3.7: Discrete port CST studio model.

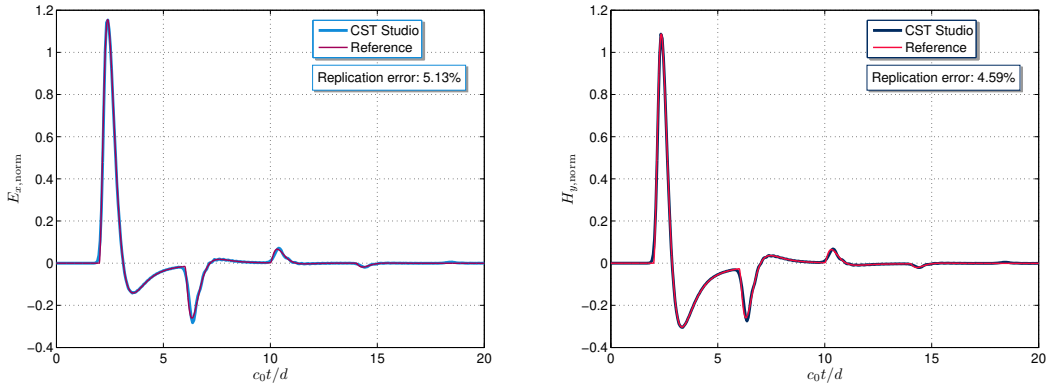

Figure 3.8: Comparison of the reference and CST Studio simulated signatures at point A (at $x/d = 0$).

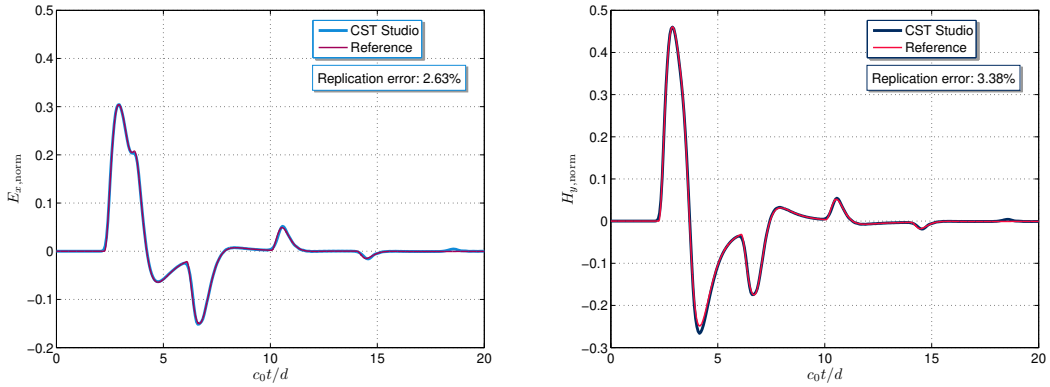

Figure 3.9: Comparison of the reference and CST Studio simulated signatures at point B (at $x/d = 1$).

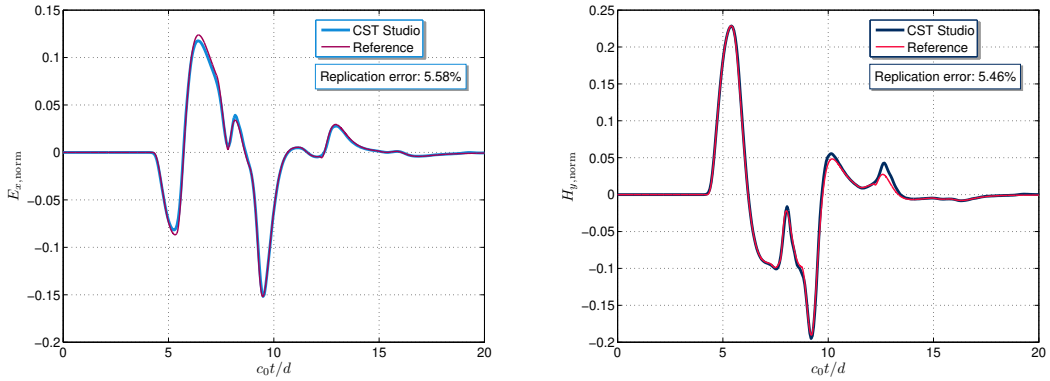

Figure 3.10: Comparison of the reference and CST Studio simulated signatures at point C (at $x/d = 3$).

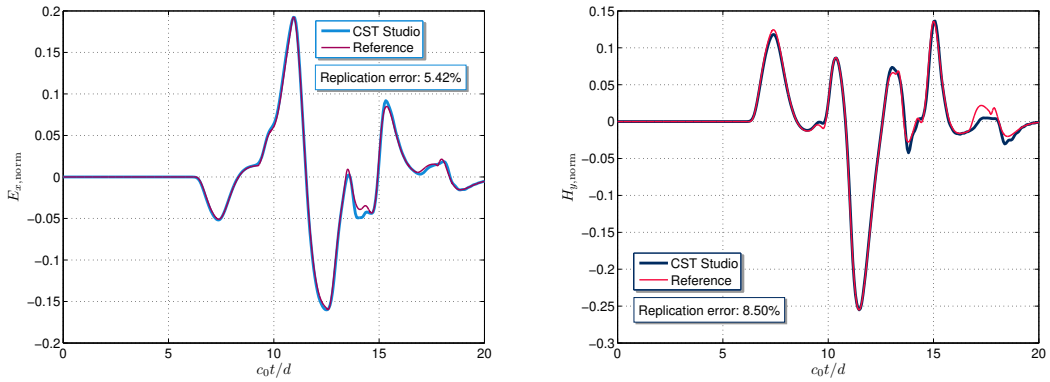

Figure 3.11: Comparison of the reference and CST Studio simulated signatures at point D (at $x/d = 5$).

Table 3.1: Replication errors in the case of the "wide slot" problem.

Field point	Replication error for $E_{x,\mathrm{norm}}$	Replication error for $H_{y,\mathrm{norm}}$
A	5.13%	4.59%
B	2.63%	3.38%
C	5.58%	5.46%
D	5.42%	8.50%

3.3.4 Conclusions

To sum up this chapter, the discrete port excitation perfectly fulfills the task of reproducing the analytical results in CST Studio with the largest replication error lower than 10% and the deviation between the maximum absolute values of unaligned simulated and reference signatures lower than 5% at all observation points. Apart from the high replication accuracy, the CST model also faultlessly reproduces the original model without excessive computational costs. In other words, a reliable tool was successfully built in CST that will provide convenience for the numerical validation of the 2D pulsed electromagnetic (EM) field radiation from a wide slot antenna with a dielectric layer on top of it.

Chapter 4

3D Electric-Current Excited Long Slot

This chapter will complement the study in [29] with a detailed TD EM numerical examination of Configuration A, by specifically bridging pLW-type features to the operation principles of the LLAs. In the process, a particular attention will be given to carefully validating all employed instruments. The account will start by introducing the configuration and the main simulation choices. The next step will be demonstrating the (almost) identity between the simulated TD signatures and the impulse response in the case of Configuration A. The main part will cover the analysis of the field propagation along the slot and in planes transverse to it, and finally conclusions will be given at the end of this chapter.

4.1 Motivation

As previously indicated, [29] looked at a few LW radiation-related configurations and discovered correspondences between conventional LW properties and the pseudo-LW (pLW) phenomena. (Note that the phrase "pseudo-LW" used in this chapter refers particularly to some wave components (rays) that reach a given field point after the head wave but before the body wave.) In order to concentrate on conceptual explanations, the study in [29] only looked at electromagnetic (EM) problems that can be handled analytically. The gap-fed slot at the air-dielectric interface (Configuration A) and the one with an extra air gap (Configuration B), which do not appear to permit an analytical TD treatment, were purposefully left out. To comprehend the LW phenomena for those two configurations, computational EM (CEM) simulations are necessary.

4.2 Investigated Configuration and Computational Choices

In this chapter, the EM waves excited along a infinite (long) slot that lies in between a dielectric half-space and a free-space half-space will be investigated thoroughly. The investigated configuration shown in Fig. 4.1 consists of a infinite slot that occupies the space $\mathcal{S} = \{-w/2 < x < w/2, 0 < y < l, z = 0\}$, in which $w > 0$ denotes its relatively small width and $l > 0$ represents its length. The PEC screen is located at the interface between the two unbounded homogeneous half-spaces $\mathcal{D}_0 = \{-\infty < x < \infty, -\infty < y < \infty, z < 0\}$ and $\mathcal{D}_1 = \{-\infty < x < \infty, -\infty < y < \infty, z > 0\}$, characterised by scalar parameters $\{\varepsilon_{0,1}, \mu_0\}$. Accordingly, the wave speeds are given by $c_0 = (\varepsilon_0\mu_0)^{-1/2}$ and $c_1 = (\varepsilon_1\mu_0)^{-1/2}$. Note that the two-media problem that will be solved in this chapter is not limited to x, y and z. Here the defined domains are just a specific case, and it can be extended to other cases.

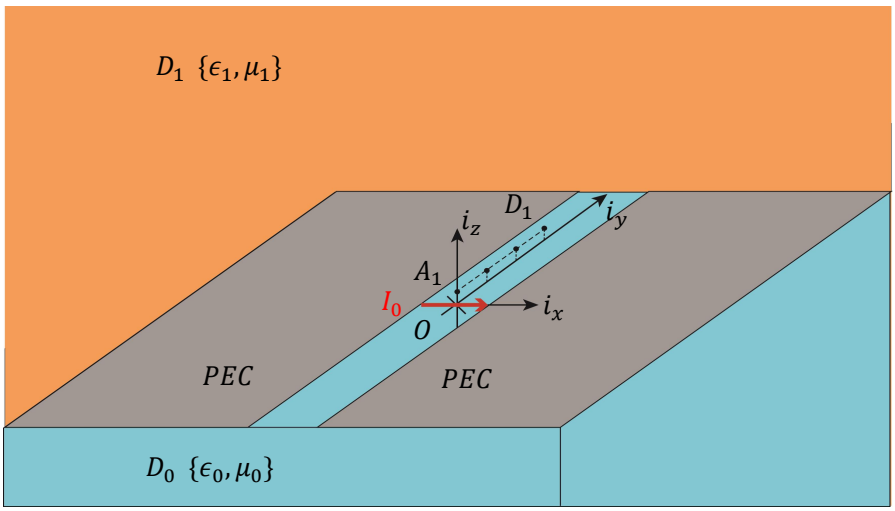

Figure 4.1: Configuration A: long slot between a dielectric and a vacuum half-space.

However, CST studio does not allow to build a model with unbounded space, therefore, the slot can not be infinitely long, and the model space must be bounded. Apart from that, the PEC screen must has a finite thickness for being able to describe its properties. In spite of this, the slot model can still be configured to imitate an infinitely long and zero-thickness slot, and the dimensions of the half-spaces can also be set to be relatively large. In this case, the actual space occupied by the long slot with very thin PEC screen is $\mathcal{S} = \{-w/2 < x < w/2, 0 < y < l, 0 < z < 0.1\text{mm}\}$. The truncated domains occupied by the vacuum and dielectric half-spaces are $\mathcal{D}_0 = \{-w_c/2 < x < w_c/2, 0 < y < l_c, -5\text{mm} < z < 0\}$ and $\mathcal{D}_1 = \{-w_c/2 < x < w_c/2, 0 < y < l_c, 0.1\text{mm} < z < 5.1\text{mm}\}$, characterised by scalar parameters $\{\varepsilon_{0,1}, \mu_0\}$, with w_c referring to the configuration width and l_c the configuration length. Note that the heights of the dielectric and vacuum half-spaces are both set to 5mm. For all the simulation results shown in this chapter, the dielectric constant ε_r of the dielectric half-space was set to 16, which means c_1 is a

quarter of c_0. The slot width and length w and l are set to 1mm and 40mm, while the configuration width and length, w_c and l_c are set to 30mm and 40mm, respectively.

The slot is excited by a discrete electric current source of unit amplitude defined by

$$\partial J_x(x, y, t) = I_0 \Pi_w(x) \delta(y) \mathrm{H}(t) \tag{4.1}$$

in which I_0 (in A) denotes the electric-current amplitude and $\Pi_w(x)$ represents a rectangular function of width w. In other words, $\Pi_w(x) = 1$ if and only if $x \in [-w/2, w/2]$ and $\Pi_w(x) = 0$ elsewhere. The Delta Dirac function and the Heaviside Unit Step function are denoted by $\delta(y)$ and $\mathrm{H}(t)$, respectively. The radiated field constituent E_x in the dielectric slab at four selected observation points A_1, B_1, C_1 and D_1 along the y axis is monitored to study the time-domain wave propagation mechanism. The vertical offset (in the z direction) is set to be a fixed 1mm, while the horizontal offsets (in both x and y directions) for four consecutive observation points are 0mm, 4mm, 8mm and 12mm, respectively. As is shown in Fig. 4.2, those four observation points along y and on the line $\{x = 0, z = 1\text{mm}\}$ are named A_1, B_1, C_1 and D_1, while those along x and on the line $\{y = 0, z = 1\text{mm}\}$ are named A_1, A_2, A_3 and A_4.

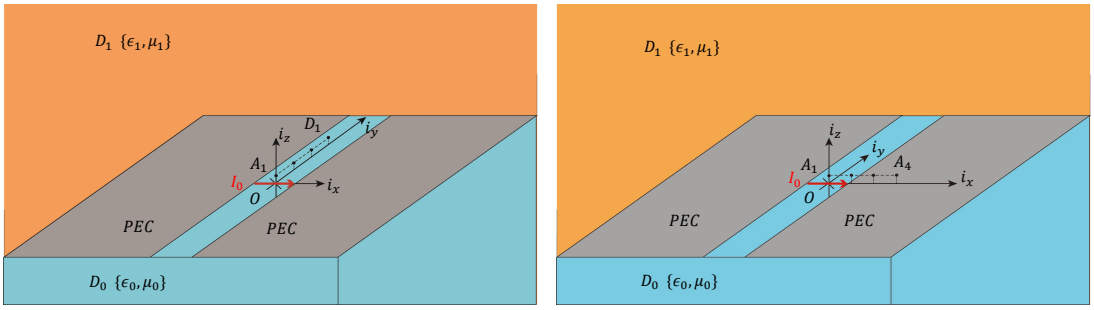

(a) Points along y (b) Points along x

Figure 4.2: Selected observation points along the x and y axis.

The frequency range in CST studio was set to be $0-40$GHz and the mesh size is set to be reasonably small to guarantee the accuracy of the simulation results. The time window of the excitation signal is from 0 to 0.5ns, with a time step of 0.5ps and a pulse width of 10ps. The feeding pulses applied in this chapter include a uni-polar triangular pulse with a pulse width t_{w} and a WP pulse characterized by pulse rising power ν and pulse rise time t_{r}. Note that the monitored field constituent in the CST Microwave Studio ® is the electric field along the x axis, namely E_x.

Inspired by the research in [29], the ray trajectory of different wave constituents can be drawn for the investigated configuration. As is shown in Fig. 4.3, the brown, white, and green segments with arrows at the top represent the body wave, head wave, and (pseudo-)leaky wave trajectories, respectively. The head wave consumes the least time

to travel from the origin O to the observation point. However, the travelling distance is not necessarily the shortest. By contrast, the body wave travels straight from the origin to the observation point, but in the meantime, it takes the longest time. As for the (pseudo-)leaky wave, it arrives after the head wave but before the body wave.

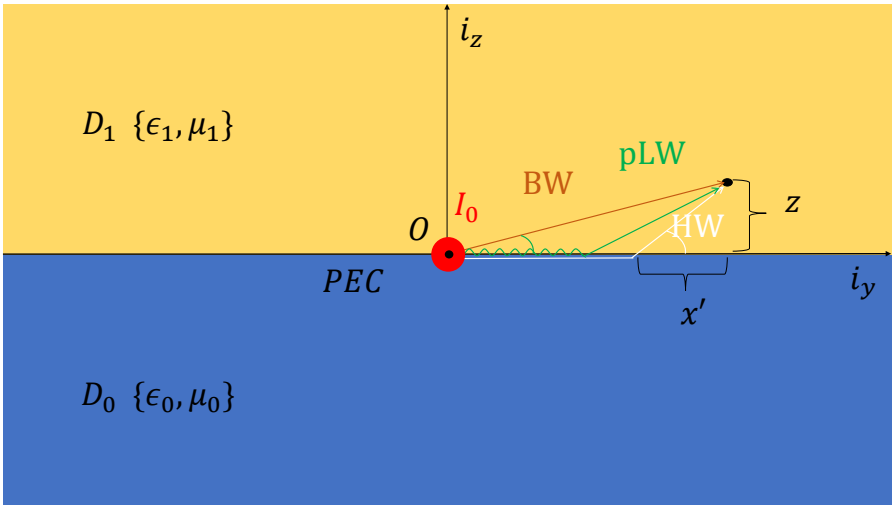

Figure 4.3: Ray trajectories of the head wave, (pseudo-)leaky wave and body wave constituents.

The arrival times of the body wave and head wave are calculated following the equations in [38]

$$T_{\mathrm{B}} = \frac{(x^2 + z^2)^{1/2}}{c_1} \tag{4.2}$$

$$T_{\mathrm{H}} = \frac{x}{c_0} + z(c_1^{-2} - c_0^{-2})^{1/2} \tag{4.3}$$

The equation for computing the arrival time of the (pseudo-)leaky wave was first derived in [29] for a different configuration, but it is assume to be of relevance for this study, as well.

$$T_{\mathrm{L}} = \frac{|x|}{\sqrt{2}}(c_1^{-2} + c_0^{-2})^{1/2} + \frac{z+h}{\sqrt{2}}(c_1^{-2} - c_0^{-2})^{1/2} \tag{4.4}$$

Unlike the body wave, which always exists, the occurrence of the head wave and the (pseudo-)leaky wave is limited to a bounded region of space. The head-wave shows up only in the region $|x|/(x^2 + z^2)^{1/2} > \sin(\vartheta_{\mathrm{H}}^{\mathrm{c}}) = c_1/c_0$, while the (pseudo-)leaky wave arises only if $|x|/(x^2 + z^2)^{1/2} > \sin(\vartheta_{\mathrm{L}}^{\mathrm{c}}) = c_1/\overline{v} = (1+c_1^2/c_0^2)^{1/2}/\sqrt{2}$. $\vartheta_{\mathrm{H}}^{\mathrm{c}}$ and $\vartheta_{\mathrm{L}}^{\mathrm{c}}$ represent

the critical angles for the head-wave and (pseudo-)leaky wave, respectively, and $\overline{v}$ denotes the (pseudo-)leaky wave speed at which the (pseudo-)leaky wave propagates along the dielectric-air interface. Details about the propagation of the waves in the vicinity of a planar dielectric – free-space interface can be found in Appendix D.

4.3 Establishing the Validity of the Impulse Response

4.3.1 Goals and Selection of the Feeding Pulse

The goals of this section are to find clear features of different wave constituents and match the calculated arrival times of each wave constituent to these features so as to understand the TD LW propagation mechanism.

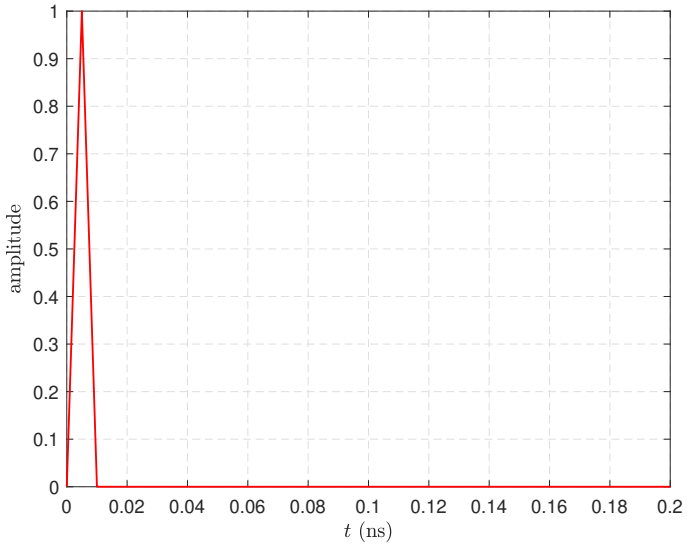

Figure 4.4: Uni-polar triangular feeding pulse of unit amplitude with $t_{\mathrm{w}} = 0.01$ns.

As is shown in Fig. 4.4, the first excitation signal used in this chapter is a unipolar triangular pulse of unit amplitude with $t_{\mathrm{r}} = 0.005$ns and $t_{\mathrm{w}} = 2t_{\mathrm{r}}$. Its spatial extent is calculated by $l_{\mathrm{tri}} = c_0 t_{\mathrm{w}} = 3$mm, which is much smaller than the slot length ($l = 40$mm), but comparable with respect to the slot width ($w = 1$mm). The former is a prerequisite in order to meet the 'long slot' assumption, while the latter can affect the intensity of ringing that will be mentioned in later sections of this chapter. Additionally, the uni-polar triangular pulse is used in this section for the following reasons.

1. A good approximation of the Delta Dirac function

2. Relatively simple analytical expression

3. Convenience for the deconvolution

4.3.2 Smoothing and Calibration

Before analyzing the field constituents of the CST simulated signatures, the results should first be smoothed and calibrated. Smoothing helps eliminate the mesh artefacts, while calibration contributes to the alignment of the time scaling. A common case is that the time scaling of the simulated signatures is ahead of that of the actual signatures, therefore, calibration is done by supplementing some zeros at the beginning of the signals, while smoothing is usually done by imposing a moving average calculation on the signatures. To sum up, smoothing and calibration are crucial for the analysis of the arrival times of different wave constituents, which will be used frequently in the following sections.

4.3.3 CST Simulated Signatures

The raw CST simulated signatures are shown in Fig. 4.5. Parts of the oscillations in each signature are due to the CST mesh artefacts. To be more specific, the CST mesh can not be infinitely small due to the limit of computer memory and calculation time, therefore, the CST simulated results are only valid in a certain frequency range. Those oscillations can be eliminated by imposing the moving average multiple times on the raw CST simulated signatures. However, those results should not be over-smoothed because parts of the oscillations are due to the ringing and the body waves, which follow the first body wave and arrive at the observation points at subsequent instants one after another. This will be discussed exhaustively in later sections.

To eliminate the mesh artefacts and better expose the features of each wave constituent, smoothing and calibration are applied to process the data from CST. The smoothed and calibrated CST results can be found in Fig. 4.6.

The arrival times of the HW, pLW and BW are represented in the figures by $\tau_{\mathrm{a;HW}}$, $\tau_{\mathrm{a;p-LW}}$ and $\tau_{\mathrm{a;BW}}$, respectively. A very notable change is that those small spikes at the tails of the signatures almost disappeared. The first wave constituent arrived at each point is used to calibrated result, and thus the arrival times of the body wave at A_1 or the head wave at B_1, C_1 and D_1 are well matched to the points where the signatures start to deviate from zero. From Fig. 4.6(b), 4.6(c), and 4.6(d), it is clear that the arrival times of the leaky wave is always close to the minimum points of the signatures, while those of the body waves get farther and father away from the minimum point and closer and closer to the peak point. In addition, there are still some subtle oscillations

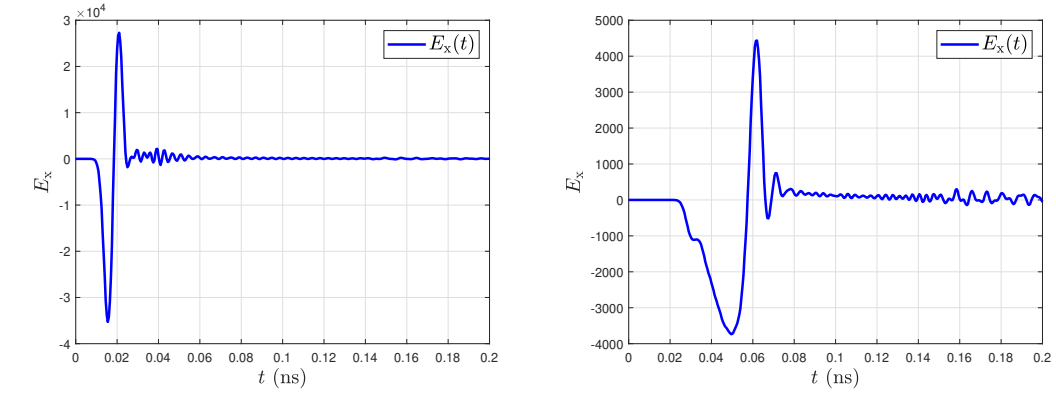

(a) A_1

(b) B_1

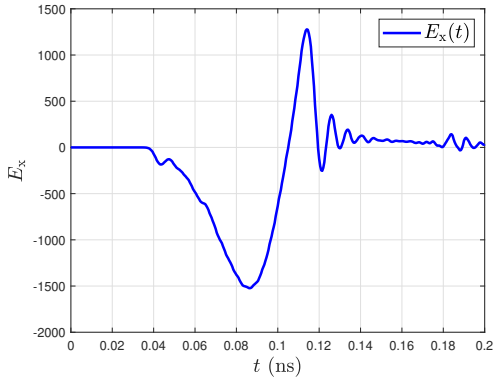

(c) C_1

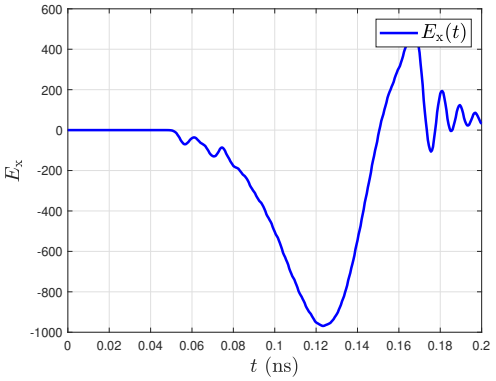

(d) D_1

Figure 4.5: Raw CST simulated signatures at observation points A_1, B_1, C_1, D_1.

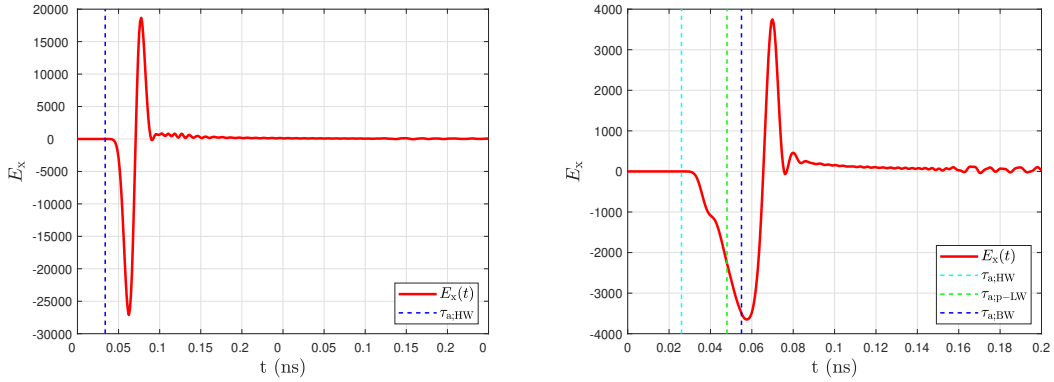

(a) A_1 (b) B_1

(c) C_1 (d) D_1

Figure 4.6: Smoothed and calibrated CST simulated signatures at observation points A_1, B_1, C_1, D_1.

in the figures, the reasons for which are worth careful study. These will be revisited and investigated in later sections.

4.3.4 The Need for the Impulse Response (TD Green's Function)

However, the conclusions above are relatively trivial and not rigorous. To get more convincing conclusions, one of the most effective methods is to calculate the impulse response of the investigated configuration at selected observation points. In general, the characteristics of different wave constituents can be clearly observed from the impulse response, also called TD Green's function. The approach of deriving the impulse response is via *deconvolution*, and two effective deconvolution strategies will be introduced in the next subsection.

4.3.5 Deconvolution Strategies

This subsection covers two different time-domain deconvolution approaches that can be compared later to verify the deconvolution results. The first approach is to directly apply the MATLAB in-built function *deconv*, while the second is the so-called Laplace Transform Method. The scripts used for deconvolution can be found in Appendix E.

MATLAB Function *deconv*

The MATLAB in-built function *deconv* helps calculate the deconvolution in a fast and convenient way. Its two input parameters are the TD radiated field and the applied feeding pulse, while the output parameters are the TD Green's function and the residue. The signatures have to be smoothed by *movmean* function, which calculates the moving average value of the signatures by choosing a reasonable time step. Note that the signatures should be smoothed once before and after the deconvolution, and then calibrated by adding certain numbers of zeros at the beginning of the vector.

Laplace Transform Method

In order to verify the deconvolution result obtained by *deconv* function, the so-called Laplace Transform method is applied as an alternative way of deconvolution. However, this method is restricted to the triangular pulse, therefore, the latter is selected to be the feeding pulse to verify the deconvolution results. The results obtained by the two methods form a straightforward comparison and can help build some confidence in the deconvolution tool. The derivation of the equations of the Laplace transform method can be found in Appendix F. Similarly, the signatures have to be smoothed once before and

after the deconvolution, and then calibrated. The deconvolution results at observation point C_1 obtained by two different approaches are compared in Fig. 4.7.

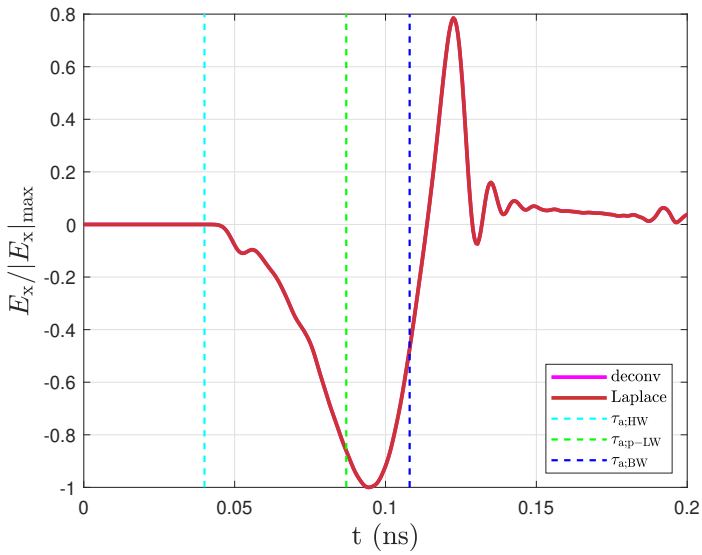

Figure 4.7: Comparison between the two deconvolved signatures by *deconv* and Laplace domain method at Point C_1 ($x = 0$, $y = 8$mm, $z = 1$mm).

Since the normalized deviation between the two results is smaller than 0.01%, the deconvolution tools are successfully verified. For later calculations, the *deconv* strategy is set to be the default tool.

Then, the deconvolved signatures (the TD Green's functions) are also compared with the smoothed and calibrated CST simulated signature at Point C_1 in Fig. 4.8. The normalized deviation between them is computed by

$$\mathrm{Err}_{\%} = \frac{|E_{\mathrm{x,CST,norm}} - G_{\mathrm{x,norm}}|}{\int_{t_{\min}}^{t_{\max}} |E_{\mathrm{x,CST,norm}}| \mathrm{d}t/(t_{\max} - t_{\min})} \times 100 \tag{4.5}$$

in which $E_{\mathrm{x,CST,norm}}$ represents the normalized and smoothed CST simulated signature, $G_{\mathrm{x,norm}}$ denotes the normalized and smoothed Green's function, $t_{\min}$ and $t_{\max}$ correspond to the start and end time of the time window. ($t_{\min} = 0$ and $t_{\max} = 0.2$ns)

Similarly, the calculated deviation between them is totally negligible, therefore, as long as the spatial extent of the triangular pulse is much smaller than the slot length $l = 40$mm, the triangular feeding pulse can be approximated to a Delta Dirac function, and thus the smoothed and calibrated CST signatures can be approximately regarded as the impulse responses. Therefore, from now on, the CST simulated signatures will be taken as the

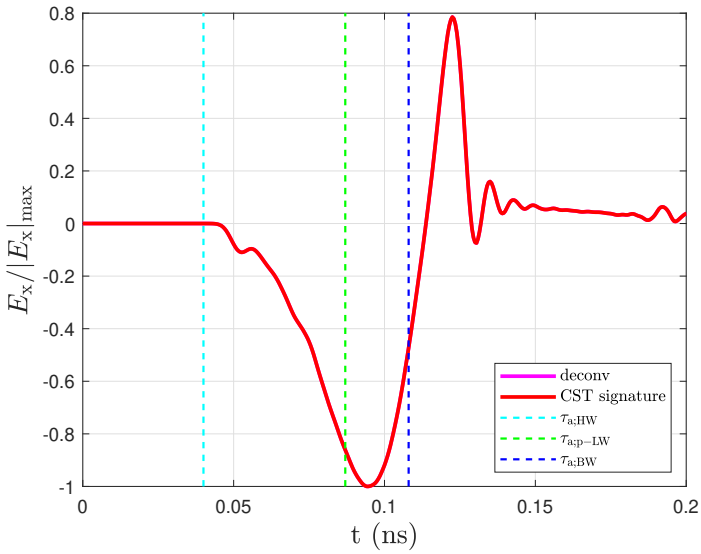

Figure 4.8: Comparison between the CST simulated signature and the deconvolved signature by *deconv* at point C_1 ($x = 0$, $y = 8$mm, $z = 1$mm).

impulse responses as long as the feeding pulse width is sufficiently small compared with the slot length.

4.3.6 Analysis of the impulse and step response

The arrival times computed by equation (4.2) to equation (4.4) mentioned in section 3.2 are listed in Table 4.1.

Table 4.1: Arrival Times of Body wave, Head wave and (pseudo-)Leaky wave

	A_1	B_1	C_1	D_1
Head Wave	NaN	0.026	0.040	0.053
(Pseudo-)Leaky Wave	NaN	0.048	0.087	0.126
Body Wave	0.013	0.055	0.108	0.161

As mentioned before, the purpose of obtaining the impulse responses is to better observe the features of each wave constituent. However, now we realize that those smoothed and calibrated CST signatures analyzed before are already the impulse responses. Another plausible approach is to resort to the step response, an idea inspired by [29]. The step response plays an essential role in analyzing the features of TD radiation in the 2D model, and thus it is also worth attempting to use it in a 3D configuration case. The impulse responses and step responses at A_1, B_1, C_1 and D_1 are listed in the Fig. 4.9 to

Fig. 4.12, marked by the red and green lines, respectively.

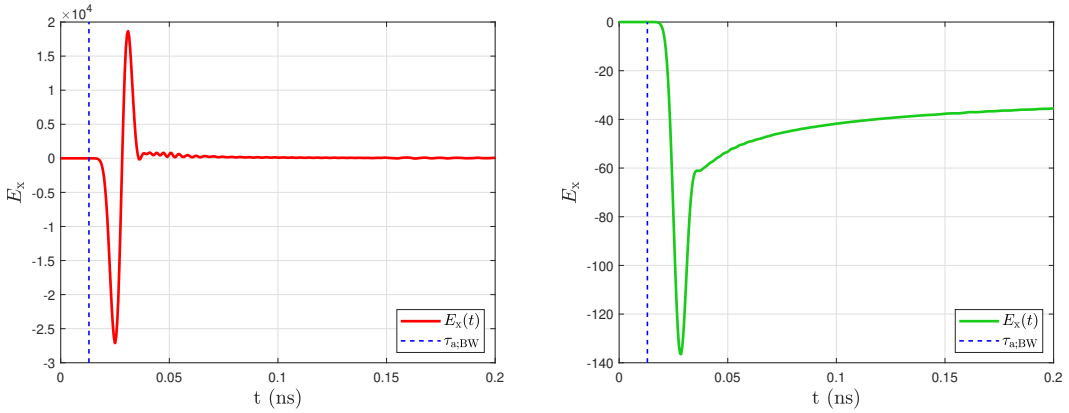

(a) Impulse response (b) Step response

Figure 4.9: Impulse and step response of the time domain Green's function at point A_1.

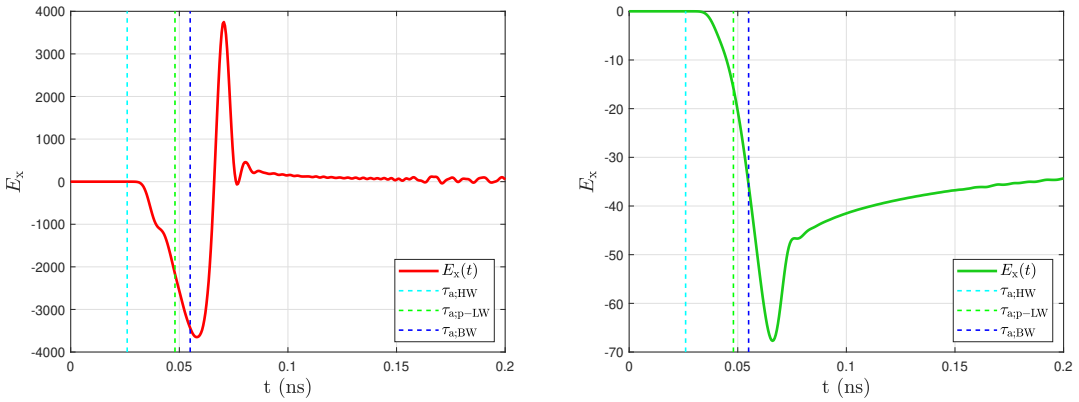

(a) Impulse response (b) Step response

Figure 4.10: Impulse and step response of the time domain Green's function at point B_1.

By comparing the two, basically two features can be observed from the step responses. First, the arrival times of the LW roughly correspond to the point, which has the largest slope. The other feature is that as the observation points become farther away from the origin, the arrival times of the body wave gradually get closer to the minimum point. However, those results are a bit trivial and not as good as expected, since the results are still not convincing enough to fully describe the features of different wave constituents. In other words, LW and BW are not dominant enough such that to be clearly observed. Unlike the case of the 2D model, in which the body wave is a root square singularity that can be seen clearly from the TD signatures [29], its arrival is relatively inconspicuous in

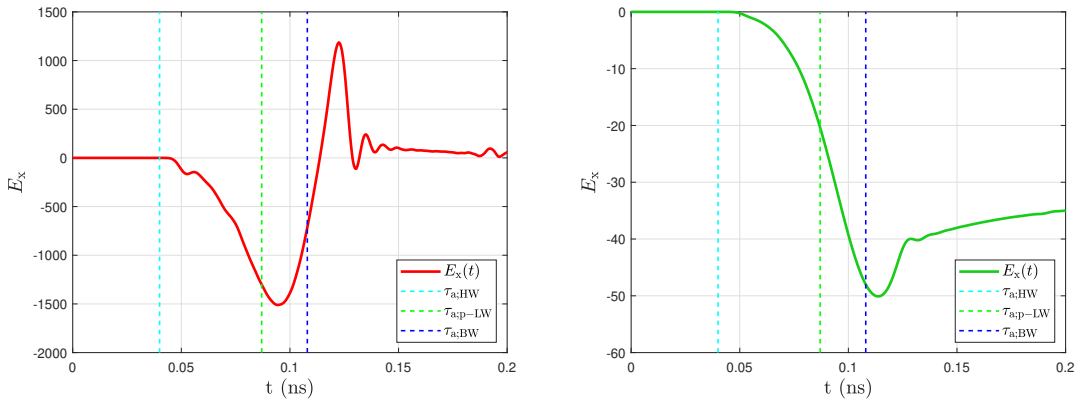

(a) Impulse response (b) Step response

Figure 4.11: Impulse and step response of the time domain Green's function at point C_1.

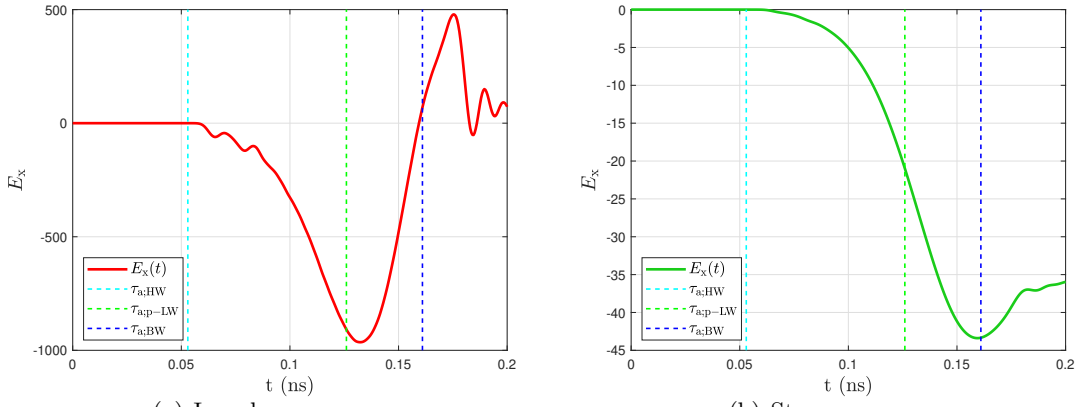

(a) Impulse response (b) Step response

Figure 4.12: Impulse and step response of the time domain Green's function at point D_1.

a 3D configuration. Although the step response is a really effective tool in the 2D case, it seemingly does not provide any extra information in the 3D configuration case. One possible reason is due to the limitation of the triangular feeding pulse. Therefore, in the next section, a better choice, the windowed power (WP) pulse, will be applied instead. Apart from that, through these experiments we can basically realize that merely the TD signatures are not enough for the study of the TD Leaky wave. Therefore, the spatial analysis will also be supplemented to better observe and analyze the leaky wave in the following section.

4.4 Feature Analysis

4.4.1 Goals and Selection of the Feeding Pulse

The goal of this feature analysis section is to study the TD leaky-wave both temporally and spatially. This subsection will concentrate on introducing the necessity of using the windowed power feeding pulse and the choices for the WP parameters. The windowed power feeding pulse, like those shown in Fig. 4.13 [45], is preferred over the triangular one for the following reasons. First, the WP pulse has a higher degree of differentiability when the pulse rising power ν is set to be reasonably large. Besides, a physical circuit for its generation is readily available. To be more specific, the WP pulse is backed by a circuit which creates a really good approximation of the so-called WP monocycle pulse (∂_tWP pulse), therefore, a very nice WP pulse can be generated from it by integration. By contrast, the triangular pulse is really hard to be replicated by a circuit, especially when the pulse width is extremely small. However, the experiments obtained via the triangular pulse are not meaningless. The advantage of the triangular pulse is that it allows a lot of analytic handling and offers a convenient tool for the comparison between the deconvolved results and the raw CST simulated signatures. Based on the solid foundation laid by those experiments, we can proceed safely with using the more preferred WP excitation signal once we establish important analytic results. More information about the triangular and WP pulses can be found in Appendix B

4.4.2 Longitudinal Analysis

TD Signatures

This subsection will focus on the longitudinal analysis, which is composed of the TD signatures at observation points A_1, B_1, C_1 and D_1 and the longitudinal snapshots at the cross-section $x = 0$ with the WP pulse as the feeding pulse. The TD signatures shown in Fig. 4.14 are the proper mimic of the impulse response (TD Green's function), in which the monitored field constituent $E_x(t)$ is denoted by the red solid line, and the

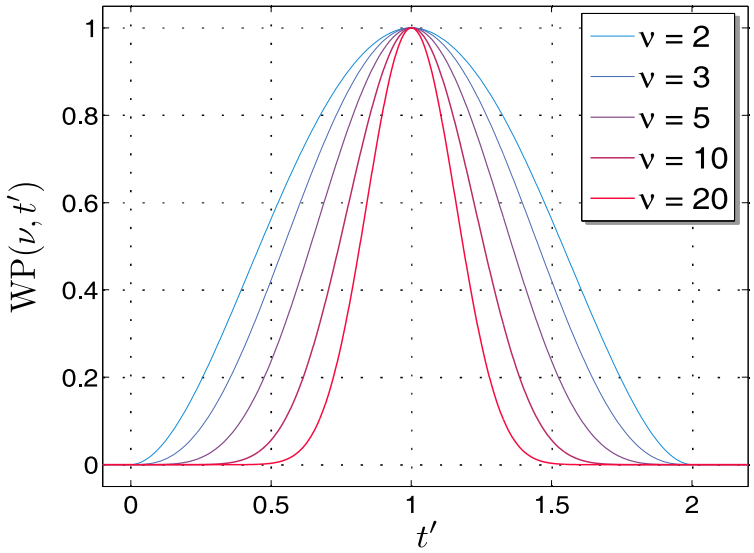

Figure 4.13: Windowed power (WP) feeding pulses of unit amplitude with ν equal to different values.

arrival times of BW, (pseudo-)LW and HW are marked by dashed lines in three different colors. Similarly, $\tau_{\alpha;\mathrm{BW}}$, $\tau_{\alpha;\mathrm{p-LW}}$ and $\tau_{\alpha;\mathrm{HW}}$ represent the arrival times of the BW, pLW and HW, respectively.

It can be seen from Fig. 4.14 that the first wave constituent, either BW (at point A_1) or HW (at point B_1, C_1 and D_1) arriving at the observation point matches the marked arrival time well because the calibration was done based on the first arrived wave constituent. In other words, the key point is to analyze the last two wave constituents at observation points B_1, C_1 and D_1. Basically, two points can be concluded from those three figures. Similar to the results obtained in the previous section, first, the arrival times of the (pseudo-)LW is really close to the minimum point of the curve, and second, as the observation points get farther and farther away from the origin, the arrival times of the body wave gradually deviate from the minimum point of the curve and gradually approach the maximum point. This means the change of the feeding pulse (from the triangular pulse to WP pulse) does not affect the impulse response much since the pulse width is already really small in both cases, and thus it is necessary to study the TD leaky wave phenomenon both temporally and spatially.

Longitudinal Snapshots

The last sub-subsection has covered the temporal analysis and initially analyzed the TD leaky wave phenomenon based on the computed arrival times and this sub-subsection is

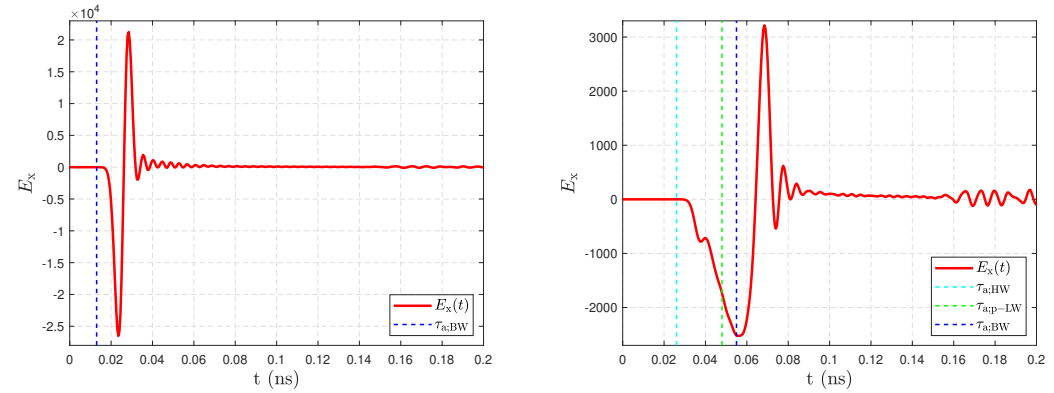

(a) A_1 (b) B_1

(c) C_1 (d) D_1

Figure 4.14: Impulse Response (TD Green's function) at observation points A_1, B_1, C_1, D_1.

going to move on to the spatial analysis part. Fig. 4.15 to Fig. 4.21 show the longitudinal snapshots at five consecutive instants (0.04ns, 0.08ns, 0.11ns, 0.16ns and 0.18ns). Unlike the TD signatures, the snapshots obtained from CST do not need to be smoothed because those snapshots are created by MATLAB *contourf* function, which integrates the data during its execution. Therefore, they are not affected by CST mesh artifacts.

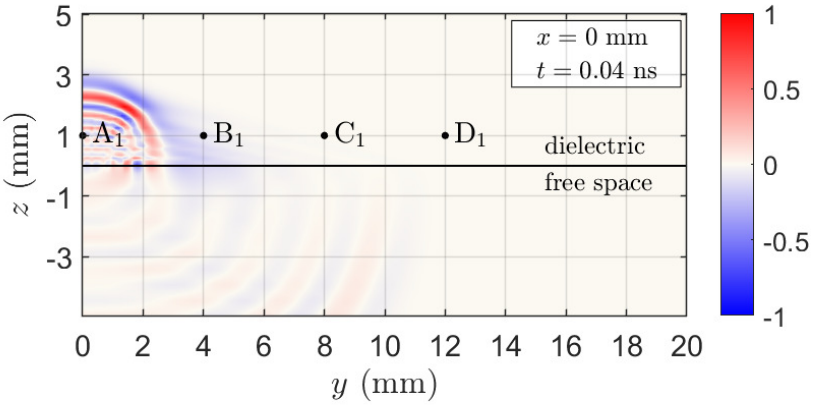

Figure 4.15: The normalized longitudinal snapshot at $x = 0$ cross-section at $t = 0.04$ns

At 0.04 ns, those arc-shaped wavefronts represent the body waves that propagate at different wave speeds. Since the dielectric permittivity of the upper half-space is $\varepsilon_r = 16$, the wave speed c_1 is a quarter of the speed of light c_0. Each point on a wavefront may be considered a source of secondary waves for the new wavefront at a later time, in accordance with Huygens' principle [50]. The waves radiated from those secondary sources travel diagonally upwards towards observation points B_1, C_1 and D_1. Before they travel upwards into to the dielectric half-space, they travel along the interface with the speed in free-space, which explains why the head wave is the first wave to arrive at observation points B_1, C_1 and D_1, even though its travelling distance is not necessarily the shortest. Around Point B_1, there are several slanting wavefronts parallel to each other. Among them, the top one represents the wavefront of the head wave, and at 0.04ns, it almost goes across point C_1, which remains consistent with the result shown in Fig. 4.14(c).

At 0.08ns, apart from those spherically spreading body waves in both half-spaces, there are other two notable features in the figure. First, there is a clear dark blue region below point C_1 and above the interface; Second, there are some standing waves travelling diagonally upwards behind the body wave and also some small "bullets" propagating along the interface. To clarify the reasons for these two phenomena, the snapshots at 0.04ns and 0.08ns should be enlarged so as to observe the details. The zoomed-in versions of Fig. 4.15 and Fig. 4.16 are shown in Fig. 4.17 and Fig. 4.18.

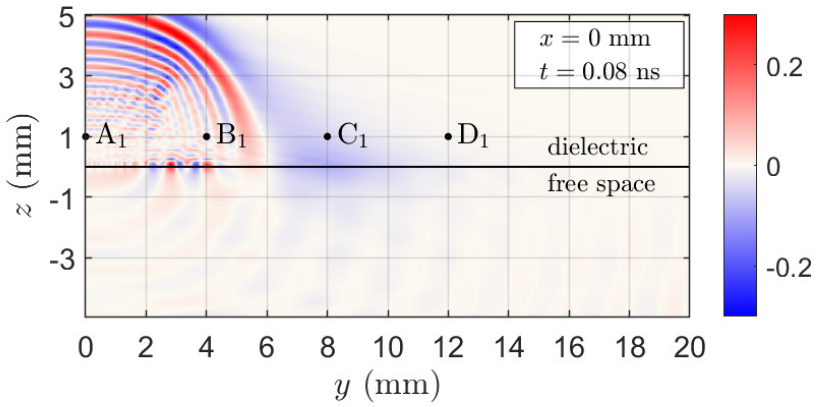

Figure 4.16: The normalized longitudinal snapshot at $x = 0$ cross-section at $t = 0.08$ns.

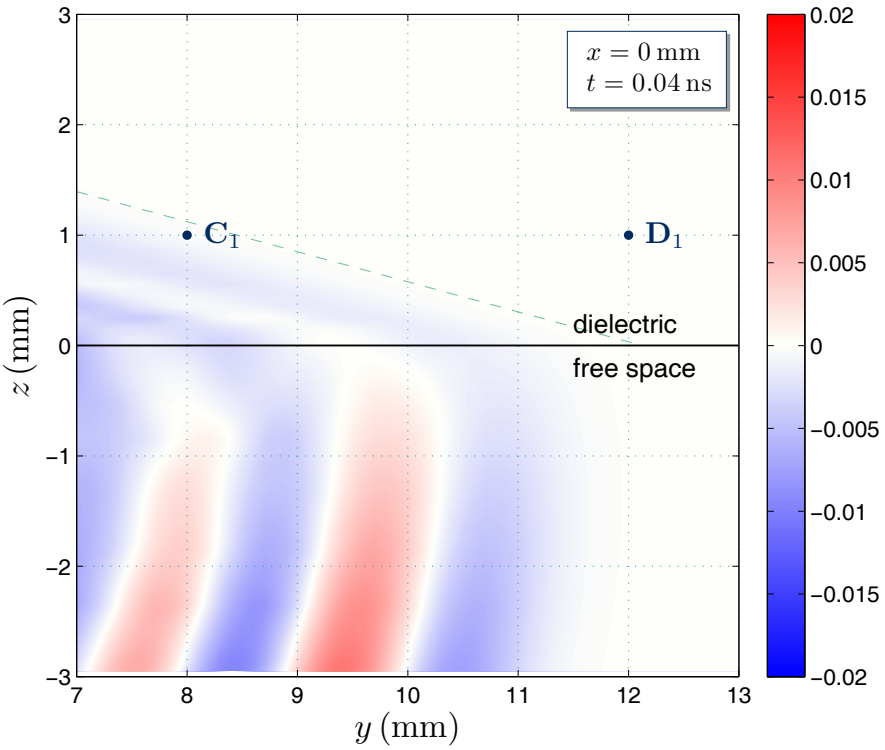

Figure 4.17: The zoomed-in normalized longitudinal snapshot at $x = 0$ cross-section at $t = 0.04$ns.

The wavefront of the HW is marked by a dashed line in Fig. 4.17 and the measured angle of the line is 164.77°. The theoretical angle that follows the calculations in Appendix D is 165.52°, which is around 1% off.

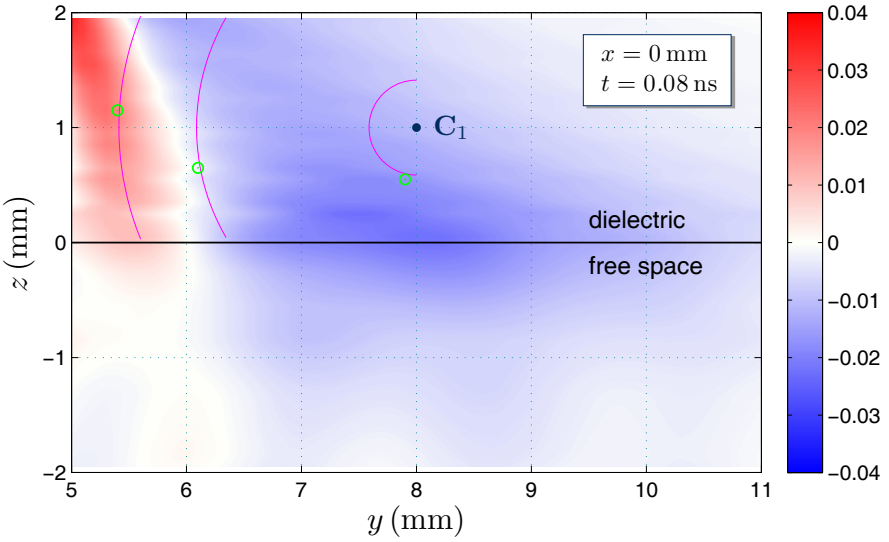

Figure 4.18: The zoomed-in normalized longitudinal snapshot at $x = 0$ cross-section at $t = 0.08$ns.

However, the snapshots at 0.04ns is not enough for the observation of the TD leaky wave, therefore Fig. 4.18 is used as a supplementary analysis. It can be seen from the figure that there are two areas with strong electric fields, the red area represents the body wave, and the blue area is the part worth analyzing. By matching the previous TD signature at point C_1 with this image point-to-point, the propagation trajectory of the wave passing through C_1 at several instants before and after can be roughly drawn, and the location of the leaky wave can be roughly determined according to the drawn trajectory. As expected, the leaky wave is right in the dark blue region. According to what we know about leaky waves, leaky waves are not causal (propagating) wave, but correspond to an enhancement of the electric field. By combining the above points, it can be determined that the dark blue area is the time-domain correspondent of the FD leaky wave.

Fig. 4.19 to Fig. 4.21 subtly explain the reason for the oscillations in the tails of the TD signatures. Take the TD signature at point C_1 as an example. From Fig. 4.14(c), it is clear that the body wave arrives at point C_1 at around 0.11ns, and in Fig. 4.19, the wavefront of the dark red area mentioned earlier formed by the BW exactly passes the point C_1, which verifies the previous conjecture. Additionally, from Fig. 4.14(c), in between 0.13ns and 0.17ns, is strongly oscillating in a manner that is reminiscent of a *Bessel function*. This is within the expectation because when the radiation caused by the peak point of the feeding pulse reaches C_1, it appears in the darkest color and when the

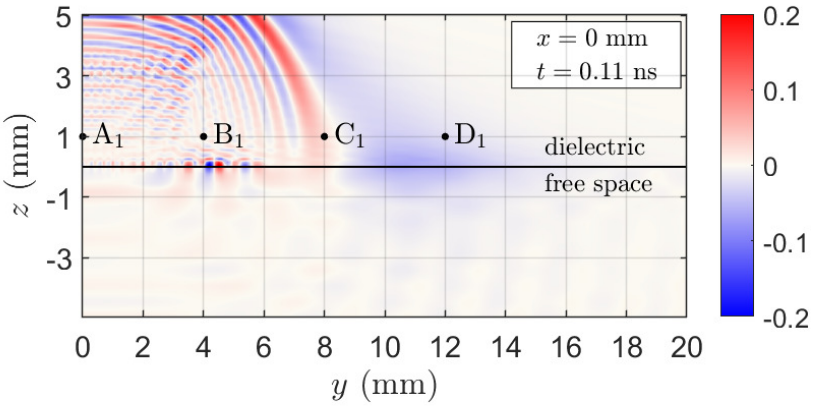

Figure 4.19: The normalized longitudinal snapshot at $x = 0$ cross-section at $t = 0.11$ns.

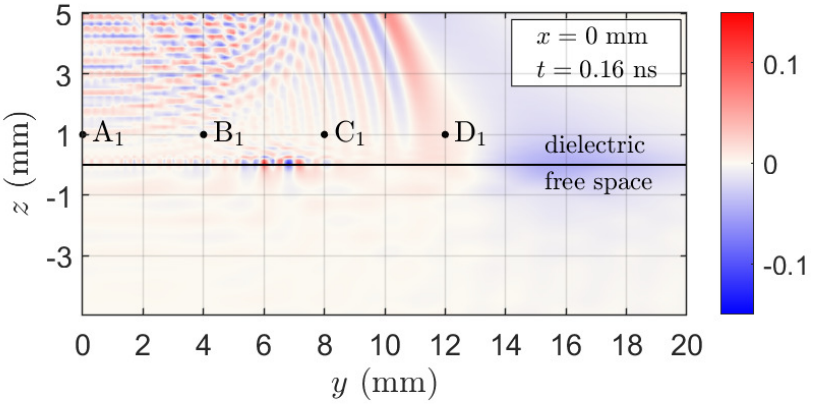

Figure 4.20: The normalized longitudinal snapshot at $x = 0$ cross-section at $t = 0.16$ns.

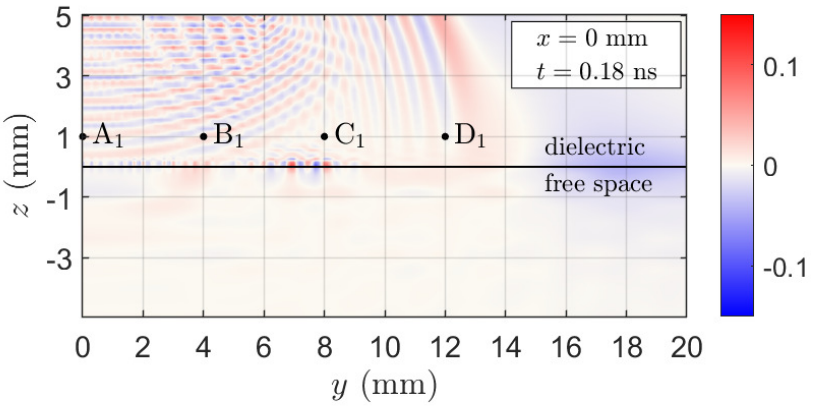

Figure 4.21: The normalized longitudinal snapshot at $x = 0$ cross-section at $t = 0.18$ns.

radiation caused by the points after the peak point of the feeding pulse reach point C_1, the color gets fainter. In between 0.13ns and 0.17ns, those body waves after the 'first' body wave pass one after another and from the snapshot at 0.16ns, it is obvious that the wave around point C_1 is just body waves. That well explains the *Bessel function*-like behavior. Last but not least, at 0.18ns, the TD signature restarts to oscillate. According to Fig. 4.21, the waves radiated from those small "bullets" has already reached point C_1 at 0.18ns, which means this part of the oscillation is not due to the body wave but to the wave radiated from the secondary sources at the interface.

Ringing

Additionally, as mentioned above, there are some small "bullets" travelling along the interface and some standing waves forming behind the body wave. In order to understand the reason for this phenomenon, the width of the feeding wave was tuned to observe the variation of the standing wave pattern and the spacing between each two "bullets". Fig. 4.22 to Fig. 4.25 basically illustrate how the pulse width affects the ringing phenomenon. When the pulse width is halved, the spacing between each two "bullets" and between each two standing wave wavefronts get smaller; When the pulse width is 1.5 times larger, the spacing becomes larger and the ringing is already very faint; When the pulse width is doubled, there is hardly any ringing in the snapshot. All in all, from the effect of pulse width on ringing, it can be concluded that the reason for the ringing phenomenon is the bouncing of feeding pulse between slot PECs. Furthermore, another conclusion can be drawn by comparing the distance between each two adjacent wavefronts in the dielectric half-space, interface and vacuum half-space that the speed of those "bullets" travelling along the interface is between the wave speed in the dielectric

half-space and the speed of light.

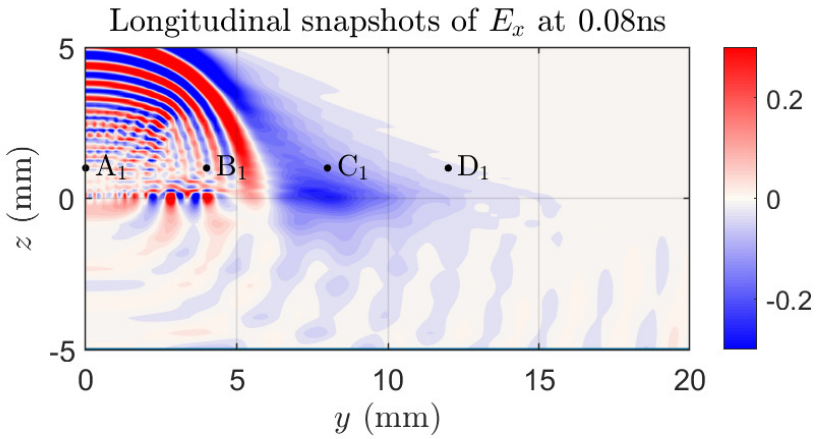

Figure 4.22: The normalized longitudinal snapshot at $x = 0$ cross-section at $t = 0.08$ns, with the WP pulse width equal to 10ps.

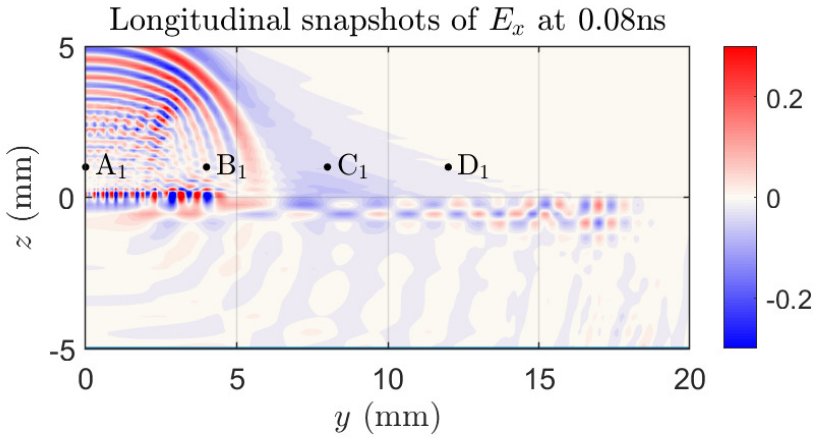

Figure 4.23: The normalized longitudinal snapshot at $x = 0$ cross-section at $t = 0.08$ns, with the WP pulse width equal to 5ps.

In summary, the ringing phenomenon caused by pulses of comparable or narrower spatial extent compared with the slot width and their effect on the radiated field is successfully evidenced, which is highly relevant when trains of pulses are studied. (The ringing phenomenon also reminds us that the precondition for assuming the smoothed and calibrated CST simulated signatures as the the impulse response is that the pulse width should be neither too small nor too large.)

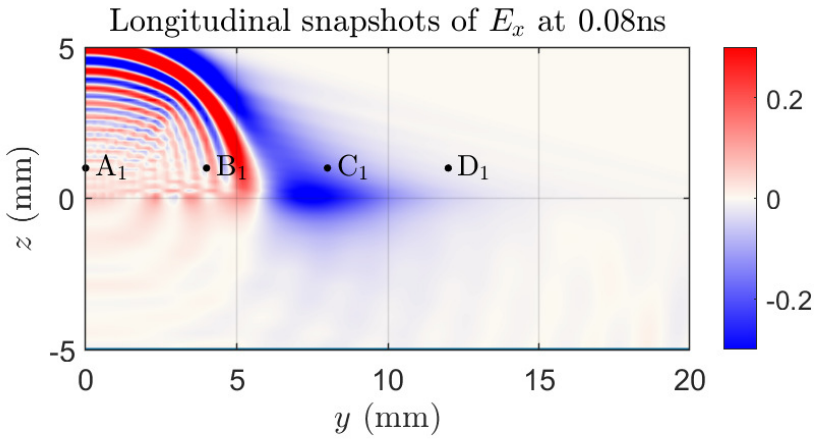

Figure 4.24: The normalized longitudinal snapshot at $x = 0$ cross-section at $t = 0.08$ns, with the WP pulse width equal to 15ps.

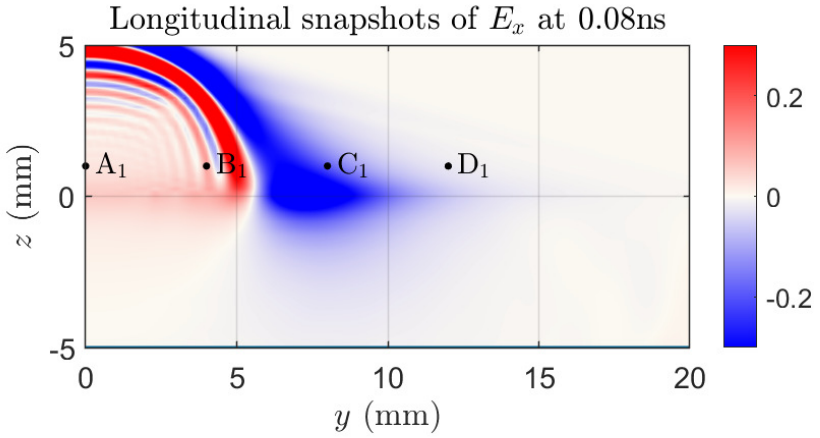

Figure 4.25: The normalized longitudinal snapshot at $x = 0$ cross-section at $t = 0.08$ns, with the WP pulse width equal to 20ps.

4.4.3 Transverse Analysis

TD Signatures

The other part of the feature analysis is carried out on the transverse cross-section. First, the smoothed and calibrated TD signatures at observation points A_1, A_2, A_3 and A_4 are shown in Fig. 4.26.

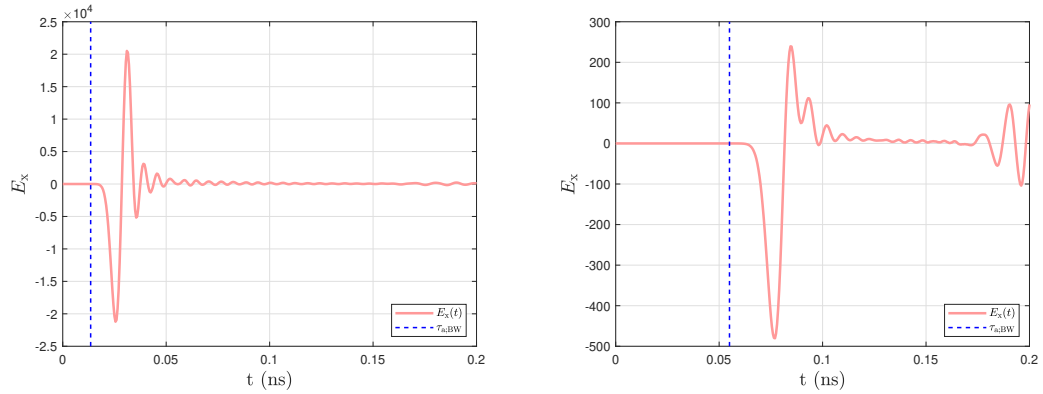

(a) A_1 (b) A_2

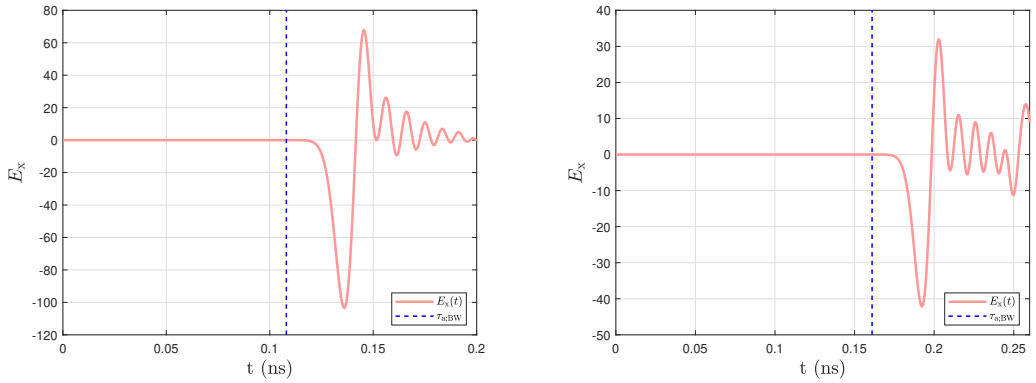

(c) A_3 (d) A_4

Figure 4.26: TD signatures at observation points A_1, A_2, A_3, A_4.

Unlike the previous case, the only wave constituent that can be noticed on the transverse TD signatures is the BW. One reason is that at the observation point A_1, the incident angle is not larger than the critical refraction angle of the HW and pLW, therefore, there is merely BW. The other reason is that the observation points A_2, A_3, A_4 are all just on top of the slot PECs, which forces the horizontal electric field E_x to zero when the field gets close to it, hence there is no chance for the HW and pLW to propagate along the dielectric-air interface between two half-spaces with the speed of light. The latter also explains why the amplitude of the curves drops dramatically as the point moves father inside the PEC.

Transverse Snapshots

Although the transverse analysis does not contribute a lot to the study of the LW phenomenon in the investigated configuration of this chapter, it is still worth analyzing the transverse snapshots so as to form a comparison with the previous longitudinal analysis. Eight transverse snapshots (normalized by the maximum absolute values of all transverse snapshots) on four different cross-sections ($y = 0$, $y = 4mm$, $y = 8mm$ and $y = 12mm$) can be found in Fig. 4.27 to Fig. 4.30

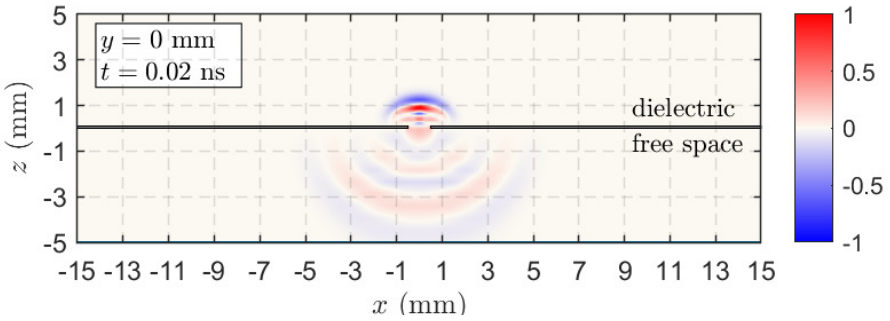

(a) $t = 0.02$ns

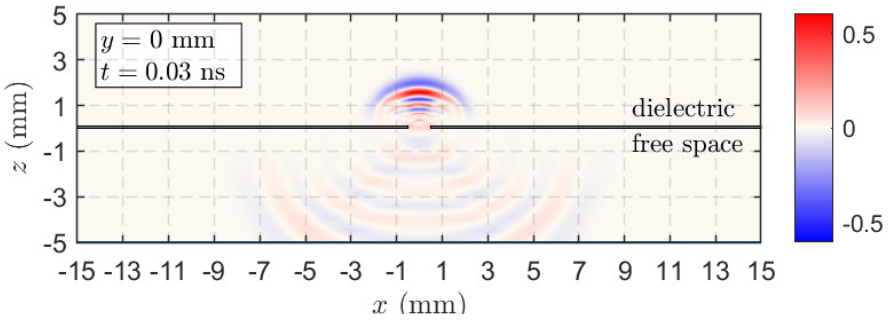

(b) $t = 0.03$ns

Figure 4.27: The normalized transverse snapshots at $y = 0$ cross-section.

The waves in Fig. 4.27 are basically spherically propagating BWs, with the wave speed of the wave in vacuum half-space four times faster than that of the wave in the dielectric half-space. At 0.03ns, there are already some standing waves travelling upwards behind the BWs, which verifies the previous analysis. In Fig. 4.28 to Fig. 4.30, the intensity of the radiation wave clearly drops, and the BWs in the bottom half-space already reach the bottom boundary. A clear standing wave pattern can be seen at 0.06ns, however, those reflections do not affect the experiment because the study concentrates on the field in the upper dielectric half-space. Only the signature behaviors between 0 and 0.2ns are considered in this thesis, and the model space is large enough that any reflection from the

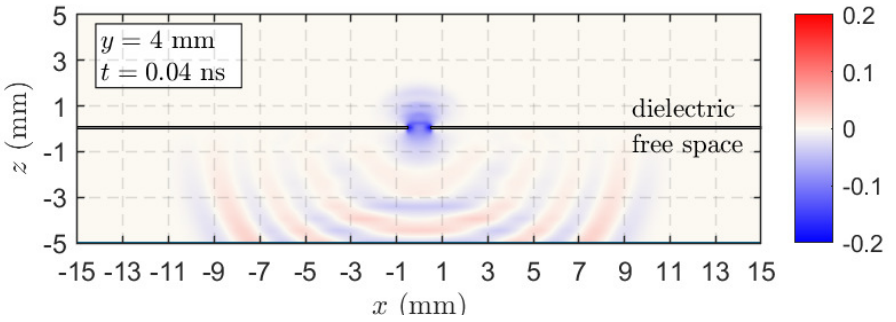

(a) $t = 0.04$ns

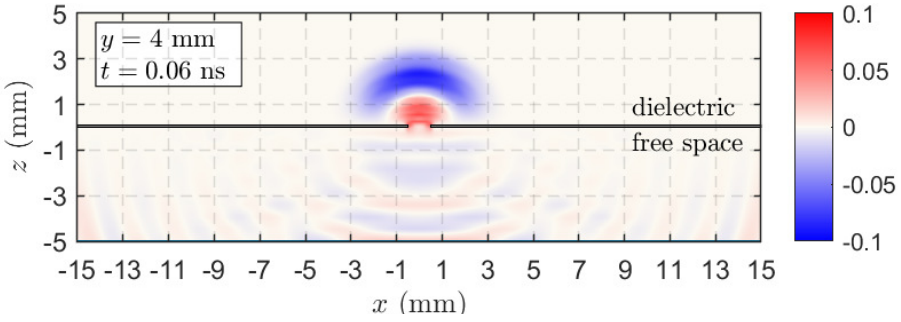

(b) $t = 0.06$ns

Figure 4.28: The normalized transverse snapshots at $y = 4$mm cross-section.

boundaries is not able to arrive at the observation points within the 0.2ns. In summary, limited by the structure of the configuration, the transverse analysis does not yield much valuable information about TD LW. In the next chapter, a new configuration will be proposed that can make better use of the transversal analysis.

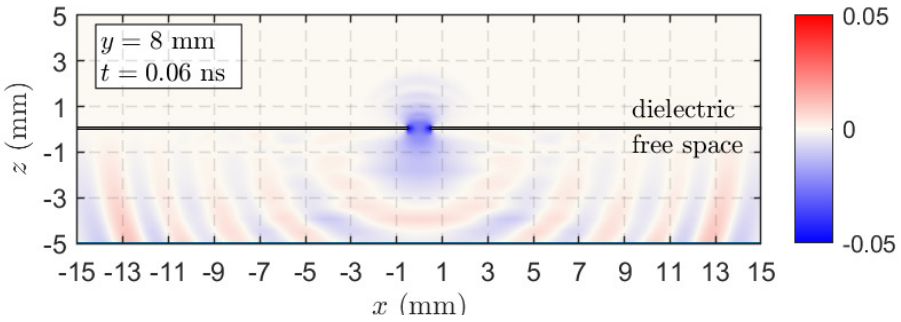

(a) $t = 0.06$ns

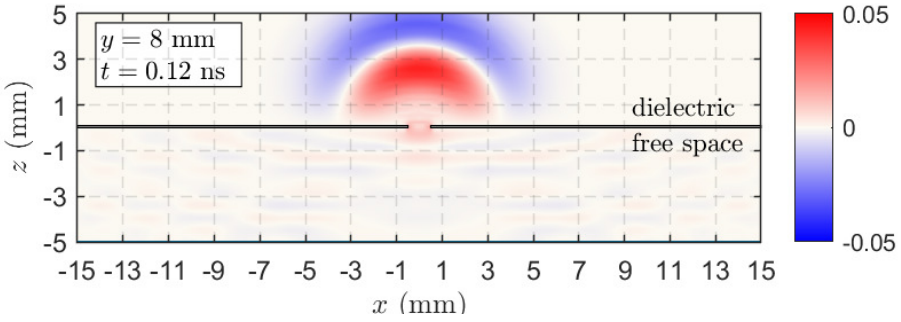

(b) $t = 0.12$ns

Figure 4.29: The normalized transverse snapshots at $y = 8$mm cross-section.

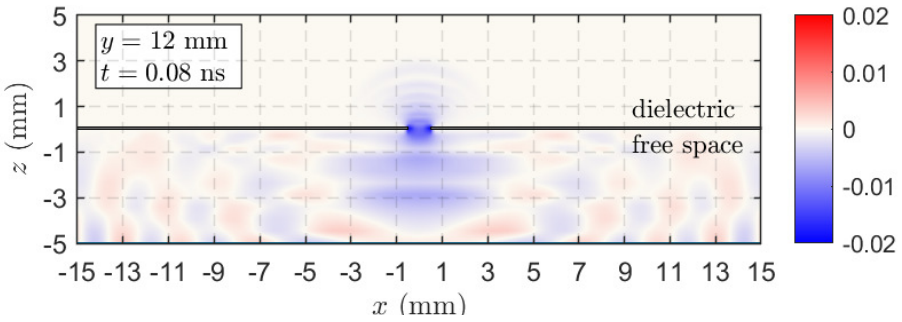

(a) $t = 0.08$ns

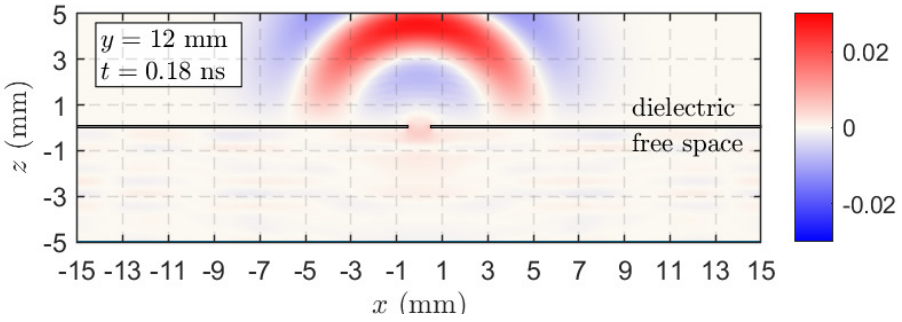

(b) $t = 0.18$ns

Figure 4.30: The normalized transverse snapshots at $y = 12$mm cross-section.

Chapter 5

3D Electric Current Excited Long Slot With an Air Gap

From this chapter on, the focus of study shifts to a new configuration, called Configuration B, which contains an additional air gap on top of the slot. Similarly, the account will begin with explaining the motivation and the investigated configuration, followed by the CST Set-ups and a few simulation choices. This chapter's major body once again consists of a section on feature analysis that covers both longitudinal and transverse analysis. Finally, this chapter will come to some significant conclusions.

5.1 Motivation

The analysis of configuration A reveals that the findings from the transverse analysis in the preceding configuration are unsatisfactory since the slot PEC will force all nearby horizontal electric fields to drop down to zero. However, the spatial and time analysis on the TD LW should not be restricted to the longitudinal cross-section. In this case, another common configuration of the leaky-lens antenna LLAs, which has an extra gap, seems to be a workaround. Through the study of this configuration, it is expected that the LW phenomenon in the transverse cross-section can also be observed. The observed features can form a good comparison with previous results to draw conclusions.

5.2 Investigated Configuration and Computational Choices

The investigated configuration of this chapter shown in Fig. 5.1 is similar to the previous one, and the only difference is an extra air gap on top of the slot. It contains a infinite slot

that occupies the space $\mathcal{S} = \{-w/2 < x < w/2, 0 < y < l, z = 0\}$, where $w > 0$ denotes its relatively small width and $l > 0$ its length. The PEC screen is located at the interface between the vacuum half-space and the air gap. The domains occupied by the two unbounded homogeneous half-spaces are $\mathcal{D}_0 = \{-\infty < x < \infty, -\infty < y < \infty, z < 0\}$ and $\mathcal{D}_1 = \{-\infty < x < \infty, -\infty < y < \infty, z > 0.5\text{mm}\}$, characterised by scalar parameters $\{\varepsilon_{0,1}, \mu_0\}$, with the height of the air gap equal to 0.5mm. Accordingly, the wave speeds are given by $c_0 = (\varepsilon_0\mu_0)^{-1/2}$ and $c_1 = (\varepsilon_1\mu_0)^{-1/2}$. Similarly, the two-media problem that will be solved in this chapter is not limited to x, y and z. Here the defined domains are just a specific case, and it can be extended to other cases.

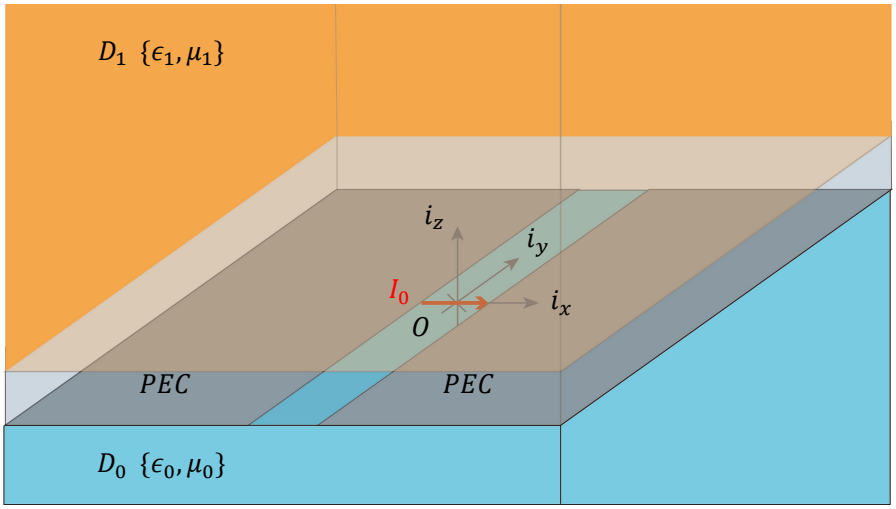

Figure 5.1: Configuration B: long slot with an extra air gap between a dielectric and a vacuum half-space.

For the same reasons mentioned in Chapter 4, the model space in CST studio should also be truncated in this chapter. In this case, the actual space occupied by the long slot with very thin PEC screen is $\mathcal{S} = \{-w/2 < x < w/2, 0 < y < l, 0 < z < 0.1\text{mm}\}$. The truncated domains occupied by the vacuum and dielectric half-spaces are $\mathcal{D}_0 = \{-w_\text{c}/2 < x < w_\text{c}/2, 0 < y < l_\text{c}, -5\text{mm} < z < 0\}$ and $\mathcal{D}_1 = \{-w_\text{c}/2 < x < w_\text{c}/2, 0 < y < l_\text{c}, 0.6\text{mm} < z < 5.6\text{mm}\}$, characterised by scalar parameters $\{\varepsilon_{0,1}, \mu_0\}$, with w_c referring to the configuration width and l_c the configuration length. Note that the heights of the dielectric and vacuum half-spaces are both set to 5mm. The other computational choices including the dielectric constant, the size of the slot, current source, observation points, frequency range, mesh size, the parameters of the WP pulse, and the monitored field constituent are exactly the same as those in Chapter 4.

One of the different parts is the ray trajectory because the additional air gap changes the trajectory of wave. Since the analytical equations to calculate the arrival times of each wave constituent under this structure do not exist, it will be hard to match the features in the TD signatures to the arrival of certain wave constituents. However, an

effective approach to analyze the effects of the extra air gap is through the comparison of time-aligned and normalized TD sigantures at the same observation points between configuration A and B.

5.3 Feature Analysis

In this section, the spatial and temporal analysis of the LW phenomena on the longitudinal and transverse cross-sections of configuration B will be provided and compared with the results in Chapter 4. The main focus of this chapter will be to observe the features of LWs and ringing phenomena on the transverse cross-sections that could not be properly observed in the previous chapter.

5.3.1 Longitudinal Analysis

TD Signatures

The time domain signatures of the electric field E_x at observation points A_1, B_1, C_1 and D_1 (same points as before) with a comparison with the results in Chapter 4 are shown in Fig. 5.2. The red and green signatures represent the fields in Configuration A and B, respectively, and are both time-aligned and normalized to their own maximum absolute values, so only the shapes of curves are concerned.

At point A_1, the shapes of the two signatures are quite similar since they are not affected by any waves that radiate from secondary sources. The waves are just body wave and the main difference you will see if you compare the unnormalized signatures is that the green curve's amplitude is much smaller than that of the red curve. The reason is that a large portion of the incident waves are reflected at the dielectric-air-gap interface due to the high contrast in electromagnetic properties between $\mathcal{D}_0$ and $\mathcal{D}_1$. At points B_1 to D_1, the shapes of the curves in different configurations start to differ significantly. Unlike the signatures in Configuration A, whose negative wiggles get wider as the observation points get farther from the origin, the negative wiggles of the signatures in Configuration B remain narrow. Apart from that, based on the previous experience, we tend to believe that the negative wiggle should be the correspondent of the LW. Furthermore, there are almost no significant peak points after the negative wiggles, which seemingly explains why Configuration B can be a better feed for the lens antenna in a Leaky-lens structure. In other words, starting from observation point B_1, the unwanted body waves in Configuration B become way less dominant than in the case of Configuration A.

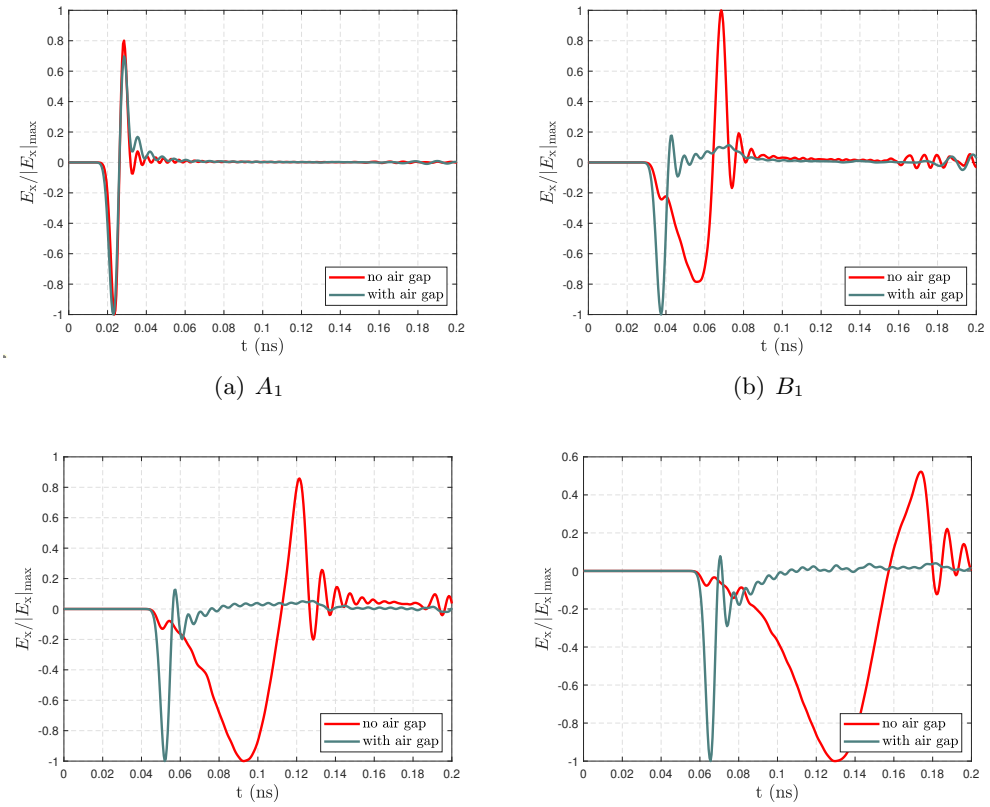

(a) A_1 (b) B_1

(c) C_1 (d) D_1

Figure 5.2: Normalized TD signatures at observation points A_1, B_1, C_1, D_1 compared with the results in Chapter 4.

Longitudinal Snapshots

The spatial analysis of the LW phenomena on the longitudinal cross-section $x = 0$ at instants 0.04ns, 0.08ns, 0.11ns, 0.16ns, and 0.18ns (same as before) is covered in this subsection. The snapshots can be found in Fig 5.3 to Fig. 5.7.

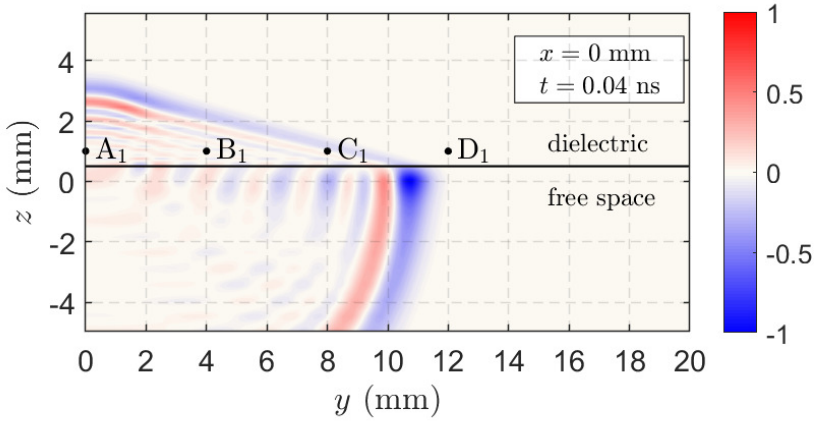

Figure 5.3: The normalized longitudinal snapshot at $x = 0$ cross-section at $t = 0.04$ns

At 0.04ns, a dark blue slanting wavefront can be clearly observed. In this case, the longitudinal snapshot can no longer be compared directly with the TD signatures, because the TD signatures were all time-aligned to be able to compare with the results in the previous chapter. However, the angle of the wavefront can still be measured and compared with the previous measured value. Here the measured angle is around 164.18°, which is almost the same as the previous measured value 164.77°. In the snapshot at 0.08ns, there are several parallel wavefronts propagating diagonally upwards. The amplitude of those waves which follow the first dark blue one gradually decreases, which explains those small oscillations after the large negative wiggle. Additionally, there are two main difference compared with the results in Chapter 4. First, at points B_1, C_1, and D_1, the body wave, which is quite dominant and can reach those observation points after the arrival of the LW in Configuration A, is largely smeared out in Configuration B. Second, there is no clear standing wave pattern and those "bullets" along the interface. The reason is that now the slot does not radiate directly in the dielectric half-space but has to go through an air gap first. According to the Snell's law, all the body waves from the slot are reflected at the interface and those waves which can arrive at those points are

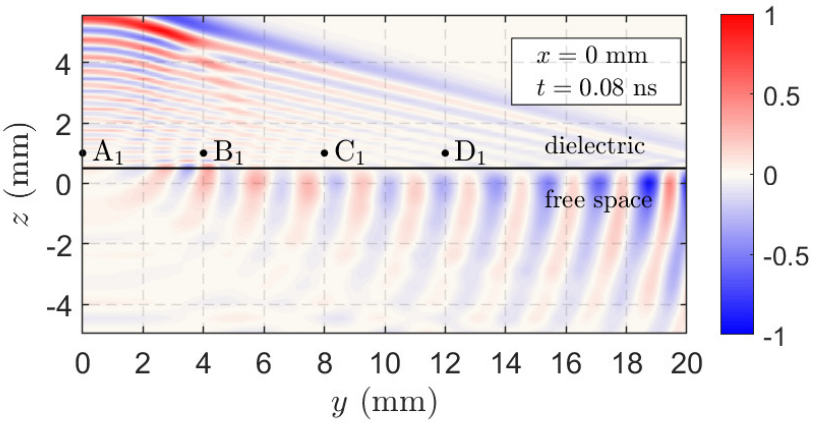

Figure 5.4: The normalized longitudinal snapshot at $x = 0$ cross-section at $t = 0.08$ns

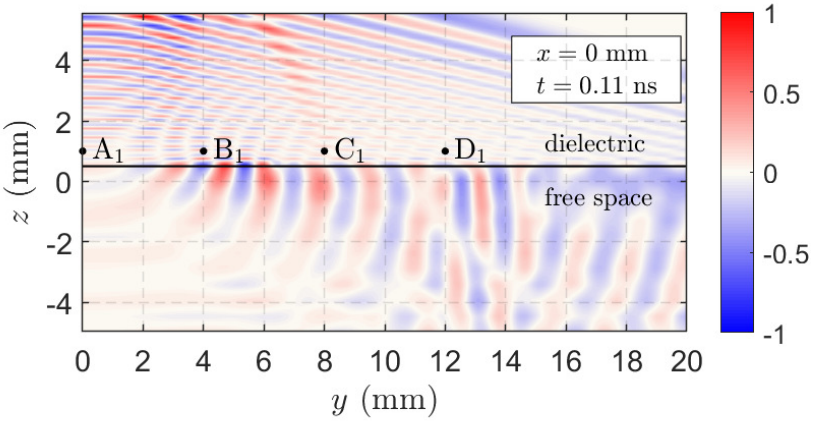

Figure 5.5: The normalized longitudinal snapshot at $x = 0$ cross-section at $t = 0.11$ns

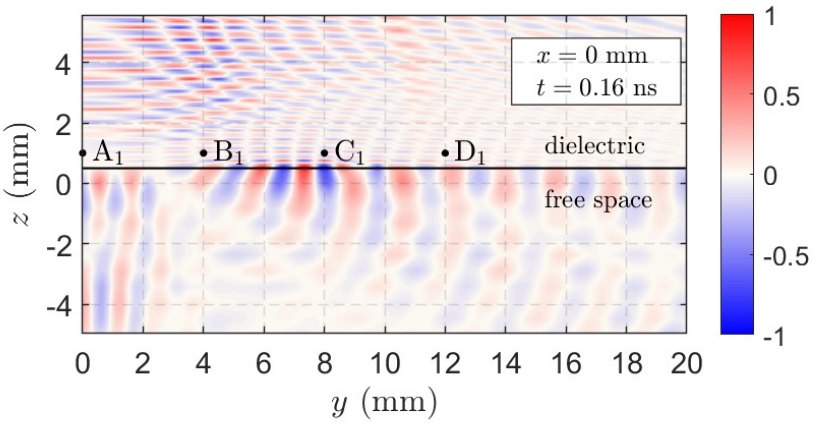

Figure 5.6: The normalized longitudinal snapshot at $x = 0$ cross-section at $t = 0.16$ns

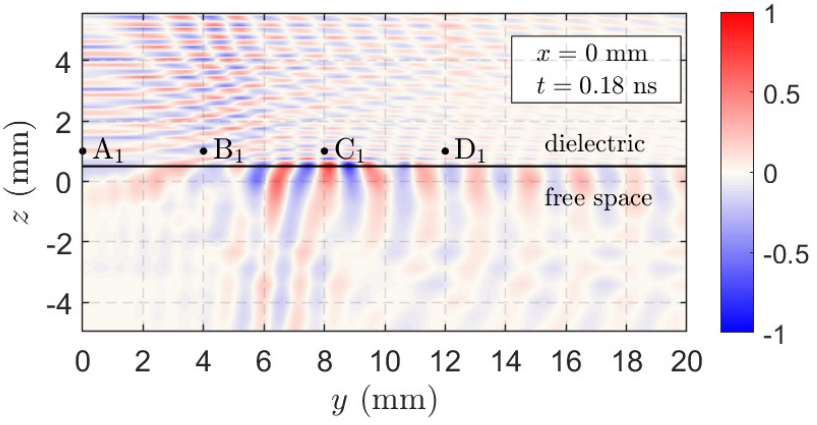

Figure 5.7: The normalized longitudinal snapshot at $x = 0$ cross-section at $t = 0.18$ns

nothing but the body waves and head waves radiating from the secondary sources along the interface. One can speculate that the disappearance of the "bullets" and, thus, of the ringing, is due to the slot now being sandwiched between domains with identical wave speed, and not highly contrasting as it was the case with Configuration A. At instants later than 0.11ns, the snapshots start to be affected by the reflections from the bottom boundary, and there is almost no new feature. Therefore, it is no longer meaningful to analyze them.

5.3.2 Transverse Analysis

TD Signatures

The comparison of the results of transverse analysis shown in Fig. 5.8 is the core of this paragraph. First of all, the results at point A_1 have been discussed in the longitudinal analysis subsection, while in the TD signatures at points B_1 to D_1 it can be seen that there is still a large difference in the shape of the curves. Similar to the longitudinal TD signature, the more significant point is that the time domain image in this chapter still does not have a significant rising segment, that is to say, the body wave radiated from the slot still does not exist at these points. A remarkable feature is that the TD signatures in this subsection still do not have significant rising segments. That is to say, the body wave radiating from the slot still does not exist at these points. However, since there is no formula for calculating the arrival times in Configuration B, there is no accurate explanation on the other characteristics of these curves.

Transverse Snapshots

The extra air gap in Configuration B offers a chance for the HW and LW to propagate and arrive at point B_1 to D_1, and thus the wave constituent is not only the spherical propagating body wave but also head wave and leaky wave. The transverse snapshots at exactly the same instants and cross-sections as in Chapter 4 are shown in Fig. 5.9 to Fig. 5.11.

Instead, in Fig. 5.9, we can see a clear slanting wavefront which smoothly connects the spherical wavefront around point A_1. Another interesting finding in Fig. 5.10 to Fig. 5.11 is that in Configuration B, although no ringing was observed in the longitudinal snapshots, it appeared in the transverse snapshots. We believe that it is due to the reflections between the slot PECs and the the interface. In Fig. 5.11(b), the pattern is too dominated by the boundary reflections, so it is no longer meaningful to analyze it. Some of the more complex explanations of the LW and ringing phenomena in the configuration of this chapter will be put in the future work section.

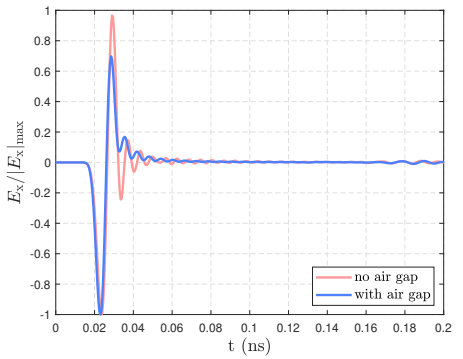

(a) A_1

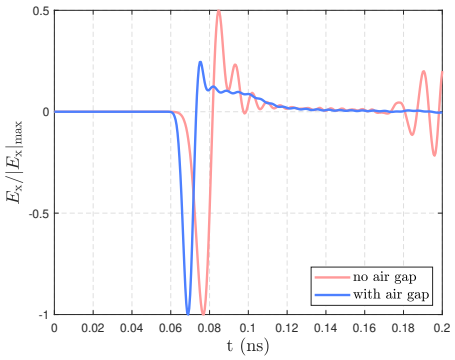

(b) A_2

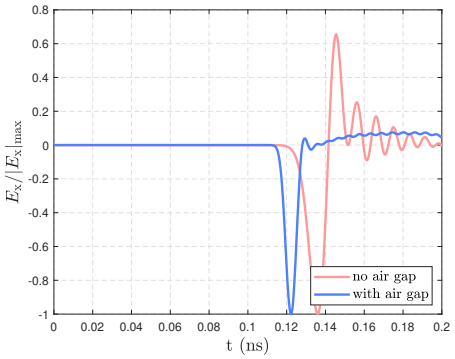

(c) A_3

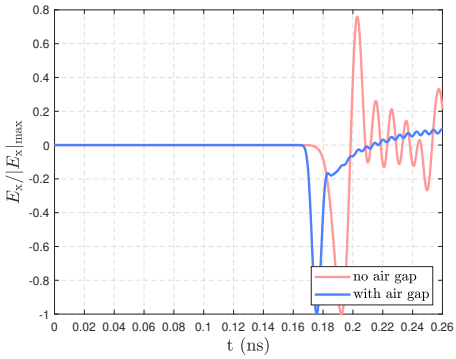

(d) A_4

Figure 5.8: Normalized TD signatures at observation points A_1, A_2, A_3, A_4 compared with the results in chapter 4.

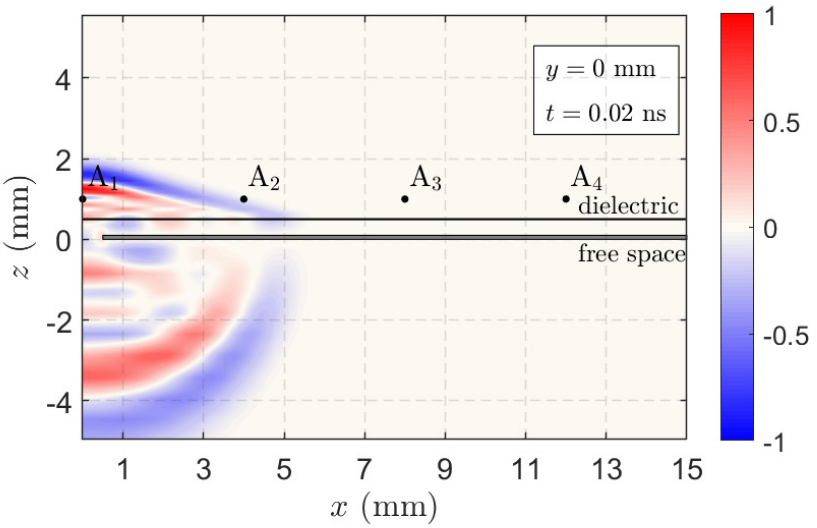

(a) $t = 0.02$ns

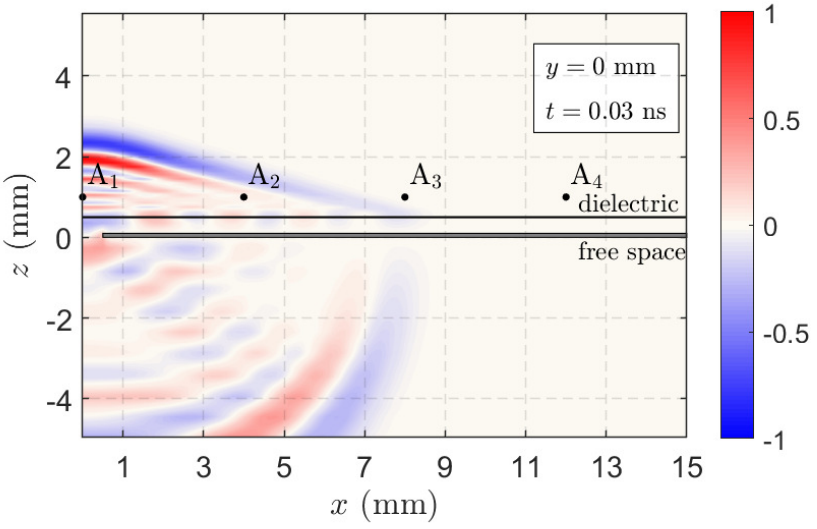

(b) $t = 0.03$ns

Figure 5.9: The normalized transverse snapshots at $y = 0$mm cross-section.

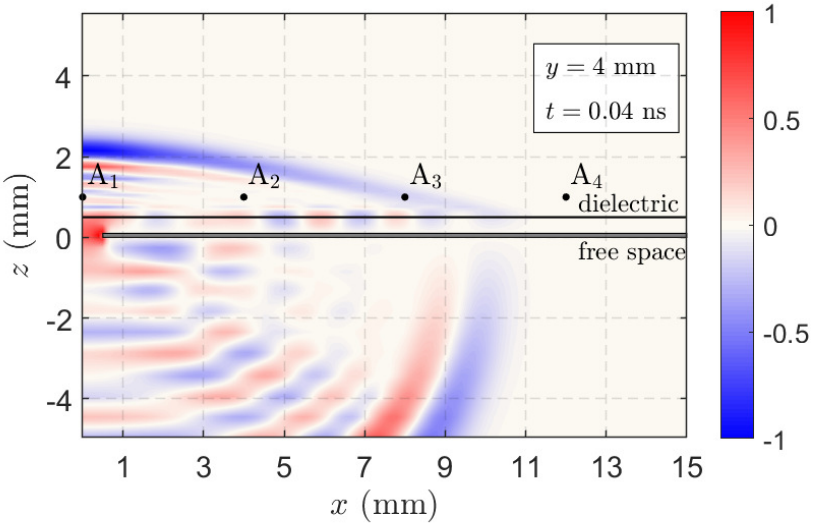

(a) $t = 0.04$ns

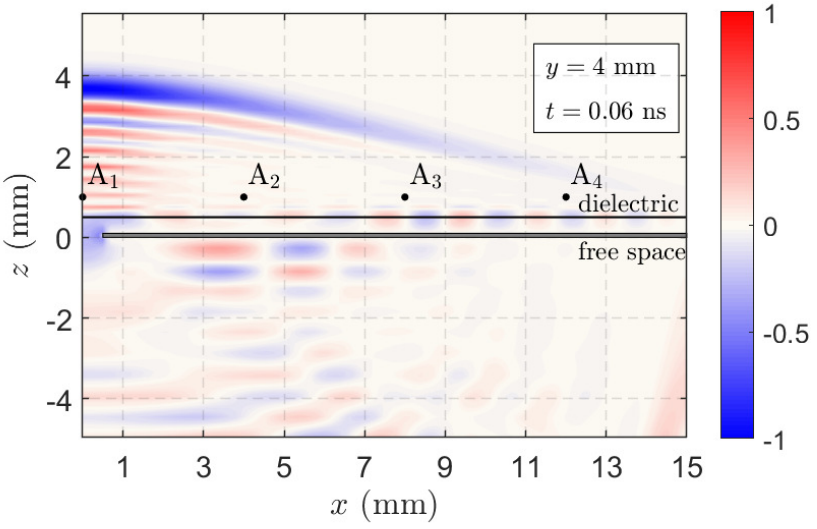

(b) $t = 0.06$ns

Figure 5.10: The normalized transverse snapshots at $y = 4$mm cross-section.

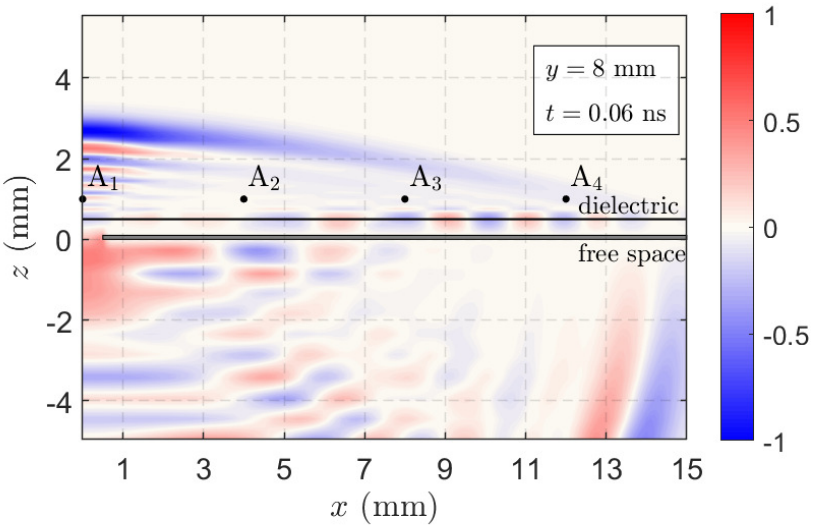

(a) $t = 0.06$ns

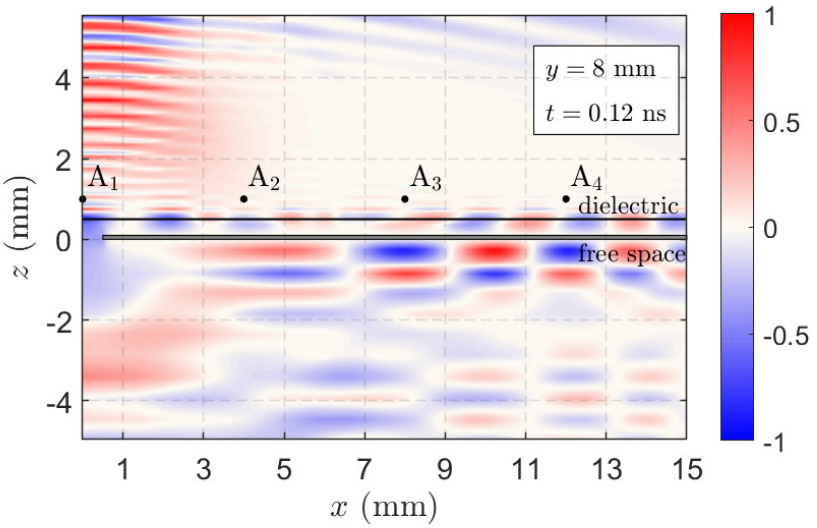

(b) $t = 0.12$ns

Figure 5.11: The normalized transverse snapshots at $y = 8$mm cross-section.

Chapter 6

Conclusions and Future Work

6.1 Summary and Conclusions

The objective of this thesis was to infer a time domain (TD) counterpart of the frequency domain (FD) leaky wave (LW) in two canonical configurations of the leaky-lens antenna (LLA) via numerical methods based on CST Microwave Studio ® simulations. To achieve that objective, a numerical validation tool and two successive studies on the TD LW in those two configurations of the LLA were provided in this thesis. First of all, in Chapter 2, some prerequisites of the experiments that have been done in this project were introduced. In order to build confidence in the CST simulation tool, Chapter 3 put forward a numerical tool for validation of the analytical pulsed electromagnetic (EM) field radiation from a wide slot with a dielectric layer. Then, in Chapter 4, the temporal and spatial analysis of the LW phenomena in a long slot antenna between a dielectric and a vacuum half-space was given, and the TD correspondent of the LWs on the snapshots was pointed out and matched with the TD signatures. Furthermore, the ringing phenomena in the longitudinal snapshots was also singled out and analyzed. Finally, in Chapter 5, the same analysis as in the previous chapter was carried out for a configuration with an extra air gap on top of the slot, and the results were compared with the results in Chapter 4 to draw conclusions. Additionally, the LW phenomena and ringing in the transverse snapshots was thoroughly investigated to complement the research that was done in Chapter 4. Finally, a notable and favorable wave front was noticed and explained with the help of the corresponding TD signatures. Overall, this thesis provides not only an effective numerical simulation tool for validating pulsed electromagnetic (EM) field radiation in specific antenna model whose analytical model has already existed, but also insights into the TD LWs in two different LLA configurations and the ringing phenomenon.

6.2 Scientific Output

The research reported in this thesis has already resulted in a published paper and is expected to be at the basis of a number of other publications:

1. J. Gu, R. van Krieken, M. Štumpf, and I. E. Lager, "Excitation in time-domain analyses: A pivotal element for accurate simulations," in *Proc. 52nd EuMC*, 2022, pp. 234–237.
2. M. Štumpf, J. Gu, and I. E. Lager, "Time-domain electromagnetic leaky waves," submitted to *IEEE Trans. Antennas Propag.*.
3. J. Gu, A. Neto, and I. E. Lager, and M. Štumpf, "Wave-front behaviour of the pulsed em field – Complexity and implications," submitted to *17th EuCAP*.
4. J. Gu, M. Štumpf, A. Neto, and I. E. Lager, "Time-domain electromagnetic leaky waves: Radiation from a long slot" under preparation, to be submitted to *IEEE Trans. Antennas Propag.*.

6.3 Future Work

This study's major objective was to suggest a causal equivalent of the LW with the intention of determining a lower constraint for the steady-state FD analysis of LW's applicability. This thesis launched a few impulse response models (single pulse excitation). The following stage is to precisely analyze pulse trains to determine how many identical pulses are required until a "steady-state" is created. Related issues to be resolved include:

- For Configuration A, how to handle the ringing following the BWs, and what effect it has on the required minimum distance between successive pulses.
- How to handle the "bullets" propagating down the interface in the event of Configuration A (also see below).
- In the event of a series of pulses, would the measured wavefronts for configuration B be affected?

Apart from the issues from a macro perspective mentioned above, some particular elements were noticed when investigating the canonical configurations A and B that could require further investigation.

For Configuration A, the problems to be solved are:

- By changing the pulse-width, several behaviors were seen. The configurational impulse response should, nonetheless, be identical. Therefore, the question arises on how to interpret the various results and how may the Green's function be defined in this situation?

- How to handle the "bullets" that show up in the longitudinal snapshots traveling along the slot for short pulses? Is it necessary to guarantee a minimum pulse width to stop the "bullets" from appearing? Do those "bullets" give more design options?

- According to the transverse analysis, the HW constituent is mostly restricted to the area above the slot. The PEC reduces the tangential E to zero, necessitating a commensurate distribution of electric current in the PEC. A follow-up investigation is needed since a thorough analysis of this current distribution may also be relevant for the far-field radiation in the two-media setup.

For Configuration B, the future work includes:

- In Chapter 5, a highly favorable wave front (in the longitudinal snapshot at 0.04ns) is shown to the reader, and several physical explanations were put forth. But in order to explore this phenomenon more accurately, both better numerical models and maybe analytical formulations are required. The initial step might be to find the analytical expression of the arrival times of different wave constituents, and after that the most significant (and challenging) follow-up on this topic may include developing a comprehensive, convincing model for pulsed-field propagation in the "slot + air gap" configuration.

References

[1] F. Monticone and A. Alù, "Leaky-wave theory, techniques, and applications: From microwaves to visible frequencies," *Proceedings of the IEEE*, vol. 103, no. 5, pp. 793–821, 2015.

[2] W. W. Hansen, "Radiating electromagnetic waveguide," 1946.

[3] D. R. Jackson, C. Caloz, and T. Itoh, "Leaky-wave antennas," *Proceedings of the IEEE*, vol. 100, no. 7, pp. 2194–2206, 2012.

[4] L. Goldstone and A. Oliner, "Leaky-wave antennas i: Rectangular waveguides," *IRE Transactions on Antennas and Propagation*, vol. 7, no. 4, pp. 307–319, 1959.

[5] A. Oliner, "Leaky waves: basic properties and applications," in *Proceedings of 1997 Asia-Pacific Microwave Conference*, vol. 1, pp. 397–400 vol.1, 1997.

[6] J. Esch, "Leaky-wave theory, techniques, and applications: From microwaves to visible frequencies," *Proc. IEEE*, vol. 103, pp. 789–792, 2015.

[7] A. Neto, "Uwb, non-dispersive radiation from the planarly fed leaky lens antenna—part 1: Theory and design," *IEEE Transactions on Antennas and Propagation*, vol. 58, no. 7, pp. 2238–2247, 2010.

[8] A. Neto and S. Maci, "Green's function for an infinite slot printed between two homogeneous dielectrics. i. magnetic currents," *IEEE Transactions on Antennas and Propagation*, vol. 51, no. 7, pp. 1572–1581, 2003.

[9] S. Maci and A. Neto, "Green's function of an infinite slot printed between two homogeneous dielectrics-part ii: uniform asymptotic solution," *IEEE Transactions on Antennas and Propagation*, vol. 52, no. 3, pp. 666–676, 2004.

[10] Z. Chen, C. Han, Y. Wu, L. Li, C. Huang, Z. Zhang, G. Wang, and W. Tong, "Terahertz wireless communications for 2030 and beyond: A cutting-edge frontier," *IEEE Communications Magazine*, vol. 59, no. 11, pp. 66–72, 2021.

[11] M. M. Azari, S. Solanki, S. Chatzinotas, and M. Bennis, "Thz-empowered uavs in 6g: Opportunities, challenges, and trade-offs," *IEEE Communications Magazine*, vol. 60, no. 5, pp. 24–30, 2022.

[12] L. Goldstone and A. Oliner, "Leaky wave antennas ii: Circular waveguides," *IRE Transactions on Antennas and Propagation*, vol. 9, no. 3, pp. 280–290, 1961.

[13] A. A. Oliner and D. R. Jackson, "Leaky-wave antennas," in *Antenna Engineering Handbook*, New York, NY, USA: McGraw-Hill, j. l. volakis ed., 2007.

[14] D. R. Jackson and A. A. Oliner, "Modern antenna handbook," in *Modern Antenna Handbook*, New York, NY, USA: Wiley, c. balanis ed., 2008.

[15] F. Scattone, M. Ettorre, B. Eddo, R. Sauleau, and N. J. G. Fonseca, "Truncated leaky-wave antenna with cosecant-squared radiation pattern," *IEEE Antennas and Wireless Propagation Letters*, vol. 17, no. 5, pp. 841–844, 2018.

[16] W. Fuscaldo, A. Galli, and D. R. Jackson, "Optimization of the radiating features of 1-d unidirectional leaky-wave antennas," *IEEE Transactions on Antennas and Propagation*, vol. 70, no. 1, pp. 111–125, 2022.

[17] A. Neto, S. Bruni, G. Gerini, and M. Sabbadini, "The leaky lens: a broad-band fixed-beam leaky-wave antenna," *IEEE Transactions on Antennas and Propagation*, vol. 53, no. 10, pp. 3240–3246, 2005.

[18] N. Llombart, G. Chattopadhyay, A. Skalare, and I. Mehdi, "Novel terahertz antenna based on a silicon lens fed by a leaky wave enhanced waveguide," *IEEE Transactions on Antennas and Propagation*, vol. 59, pp. 2160–2168, 2011.

[19] N. T. Nguyen, R. Sauleau, and L. Le Coq, "Reduced-size double-shell lens antenna with flat-top radiation pattern for indoor communications at millimeter waves," *IEEE Transactions on Antennas and Propagation*, vol. 59, no. 6, pp. 2424–2429, 2011.

[20] I. Vakili, L. Ohlsson, M. Gustafsson, and L. Wernersson, "Wideband and non-dispersive wavelet transmission using leaky lens antenna," *Electronics Letters*, vol. 49, no. 5, p. 321–322, 2013.

[21] A. Neto, N. Llombart, J. J. A. Baselmans, A. Baryshev, and S. J. C. Yates, "Demonstration of the leaky lens antenna at submillimeter wavelengths," *IEEE Transactions on Terahertz Science and Technology*, vol. 4, no. 1, pp. 26–32, 2014.

[22] L. Ohlsson, D. Sjöberg, and L.-E. Wernersson, "Codesign of compact iii–v millimeter-wave wavelet transmitters with on-chip antennas," *IEEE Transactions on Microwave Theory and Techniques*, vol. 66, no. 1, pp. 273–279, 2018.

[23] S. van Berkel, E. S. Malotaux, C. De Martino, M. Spirito, D. Cavallo, A. Neto, and N. Llombart, "Wideband double leaky slot lens antennas in cmos technology at submillimeter wavelengths," *IEEE Transactions on Terahertz Science and Technology*, vol. 10, no. 5, pp. 540–553, 2020.

[24] S. Bruni, A. Neto, and F. Marliani, "The ultrawideband leaky lens antenna," *IEEE Transactions on Antennas and Propagation*, vol. 55, no. 10, pp. 2642–2653, 2007.

[25] S. Hähnle, O. Yurduseven, S. van Berkel, N. Llombart, J. Bueno, S. J. C. Yates, V. Murugesan, D. J. Thoen, A. Neto, and J. J. A. Baselmans, "An ultrawideband leaky lens antenna for broadband spectroscopic imaging applications," *IEEE Transactions on Antennas and Propagation*, vol. 68, no. 7, pp. 5675–5679, 2020.

[26] M. Arias Campo, D. Blanco, S. Bruni, A. Neto, and N. Llombart, "On the use of fly's eye lenses with leaky-wave feeds for wideband communications," *IEEE Transactions on Antennas and Propagation*, vol. 68, no. 4, pp. 2480–2493, 2020.

[27] A. Garufo, N. Llombart, and A. Neto, "Radiation of logarithmic spiral antennas in the presence of dense dielectric lenses," *IEEE Transactions on Antennas and Propagation*, vol. 64, no. 10, pp. 4168–4177, 2016.

[28] H. Zhang, S. Bosma, A. Neto, and N. Llombart, "A dual-polarized 27 dbi scanning lens phased array antenna for 5g point-to-point communications," *IEEE Transactions on Antennas and Propagation*, vol. 69, no. 9, pp. 5640–5652, 2021.

[29] J. G. M. Stumpf and I. E. Lager, "Time-domain electromagnetic leaky waves," *IEEE Transactions on Antennas and Propagation.* submitted.

[30] L. Felsen and F. Niu, "Spectral analysis and synthesis options for short pulse radiation from a point dipole in a grounded dielectric layer," *IEEE Transactions on Antennas and Propagation*, vol. 41, no. 6, pp. 747–754, 1993.

[31] D. Duffy, "Response of a grounded dielectric slab to an impulse line source using leaky modes," *IEEE Transactions on Antennas and Propagation*, vol. 42, no. 3, pp. 340–346, 1994.

[32] G. Hanson, A. Yakovlev, and J. Hao, "Leaky-wave analysis of transient fields due to sources in planarly layered media," *IEEE Transactions on Antennas and Propagation*, vol. 51, no. 2, pp. 146–159, 2003.

[33] D. Duffy, *Green's Functions with Applications.* Applied Mathematics, CRC Press, 2001.

[34] G. W. Hanson, H. Xin, W. C. Chew, N. Engheta, C. Fumeaux, and S. C. Hagness, "The role of commercial simulators and multidisciplinary training in graduate-level electromagnetics education [education corner]," *IEEE Antennas and Propagation Magazine*, vol. 59, no. 6, pp. 127–130, 2017.

[35] T. P. Stefański, "Electromagnetic problems requiring high-precision computations," *IEEE Antennas and Propagation Magazine*, vol. 55, no. 2, pp. 344–353, 2013.

[36] "IEEE standard for validation of computational electromagnetics computer modeling and simulations," *IEEE Std 1597.1-2008*, pp. c1–41, 2008.

[37] M. S. Junhong Gu, Roy van Krieken and I. E. Lager, "Excitation in time-domain analyses: A pivotal element for accurate simulations," in *Proc. 52nd EuMC*, (Milan, Italy), pp. 234–237, 2022.

[38] A. T. De Hoop, M. Stumpf, and I. E. Lager, "Pulsed electromagnetic field radiation from a wide slot antenna with a dielectric layer," *IEEE Transactions on Antennas and Propagation*, vol. 59, no. 8, pp. 2789–2798, 2011.

[39] I. E. Lager, A. T. de Hoop, and T. Kikkawa, "Model pulses for performance prediction of digital microelectronic systems," *IEEE Transactions on Components, Packaging and Manufacturing Technology*, vol. 2, no. 11, pp. 1859–1870, 2012.

[40] A. K. Garg, *Classical Electromagnetism in a Nutshell.* Princeton N.J.: Princeton University Press, 2012.

[41] D. H. A. T., *Handbook of radiation and scattering of waves: Acoustic waves in fluids, elastic waves in solids, electromagnetic waves.* London: Academic Press, 1995.

[42] I. E. Lager, "Causal excitation in antenna simulations," *Radioengineering*, vol. 30, no. 1, p. 1–9, 2021.

[43] I. Lager and M. Stumpf, "Amplitude-modulated, cosine pe and wp pulses: Theory and applicability," *Radioengineering*, vol. 30, no. 2, pp. 443–448, 2021.

[44] M. Štumpf, A. T. de Hoop, and I. E. Lager, "Pulsed electromagnetic field radiation from a narrow slot antenna with a dielectric layer," *Radio Science*, vol. 45, no. 5, 2010.

[45] I. E. Lager and S. L. van Berkel, "Finite temporal support pulses for em excitation," *IEEE Antennas and Wireless Propagation Letters*, vol. 16, pp. 1659–1662, 2017.

[46] M. Štumpf, A. T. De Hoop, and G. A. E. Vandenbosch, "Generalized ray theory for time-domain electromagnetic fields in horizontally layered media," *IEEE Transactions on Antennas and Propagation*, vol. 61, no. 5, pp. 2676–2687, 2013.

[47] A. T. De Hoop, "A modification of cagniard's method for solving seismic pulse problems," *Applied Scientific Research, Section B*, vol. 8, no. 1, p. 349–356, 1960.

[48] M. Štumpf, "Time-domain analysis of rectangular power-ground structures with relaxation," *IEEE Transactions on Electromagnetic Compatibility*, vol. 56, no. 5, pp. 1095–1102, 2014.

[49] R. Courant, K. Friedrichs, and H. Lewy, "Uber die partiellen differenzengleichungen der mathematischen physik," *Mathematische Annalen*, vol. 100, no. 1, p. 32–74, 1928.

[50] N. V. TKACHENKO, "Huygens principle."

[51] M. STUMPF, *Cagniard-DeHoop technique*. INST OF ENGIN AND TECH, 2022.

[52] D. V. Widder, *The laplace transform*. Princeton, NJ: Princeton Univ. Press u.a., 1946.

[53] M. Abramowitz and I. A. Stegun, *Handbook of Mathematical Functions*. New York: Dover, 1968.

Appendix A

The Cagniard-de Hoop Method for the Generic Field Constituents

In wave field physics, the Cagniard-DeHoop (CdH) method, or modified Cagniard method, is a complicated mathematical method for resolving initial value issues. It may be thought of as a clever reduction of the complex joint transform operation attributed to Cagniard [51]. This method was initially developed for seismic problems, and later expanded to solving acoustic and electromagnetic problems, etc [41].

With the help of integral transformations done with regard to temporal and spatial variables, a broad class of initial value issues may be solved. The CdH approach first applies a one sided Laplace transform with respect to time of the type

$$F(s) = \int_{t=0}^{\infty} \exp(-st) f(t) \mathrm{d}t \tag{A.1}$$

in which s has a real and positive value based on the Lerch's uniqueness theorem [52]. The later theorem explicitly asserts that the weaker condition that $F(s)$ be defined at a succession of real s values $\{s \in \mathbb{R}; s_n = s_0 + nh, s_0 > 0, h > 0, n = 0, 1, 2, ...\}$ ensures the uniqueness of the inverse transformation. [38]. Then, it follows a spatial Fourier transform of the type

$$\mathscr{F}(\alpha, y, s) = \int_{-\infty}^{\infty} \exp(is\alpha x) F(x, y, s) \mathrm{d}x \tag{A.2}$$

in which $\alpha = -ip$ and p is a complex variable in the p-plane.

The time domain field quantities are transformed into the so-called slowness domain after the unilateral Laplace transform and spatial Fourier transform. In the slowness

domain, the solution of a certain wave function based on the configuration can be found. Then, with the aid of the inverse Fourier transform, the solution expressed in the Laplace domain can be obtained, which is exactly the so-called slowness domain representation. The electromagnetic problem at hand is then solved in the slowness domain that, in the majority of the cases, amounts to determining the transmission/reflection coefficients pertaining to some "generalized-rays" propagating through the layered configuration [46]. Arriving at the TD equivalent of the relevant slowness-domain solutions requires calculating an inverse Laplace transform. By starting from the definition of the inverse Laplace transform, and under the application of Cauchy's theorem and Jordan's lemma, the Bromwich integration contour is suitably deformed into a new one, the so-called *Cagniard–DeHoop path*. Under this deformation, the integrand transforms into an expression that is readily recognized as the Laplace transform of a function with respect to a real, positive parameter τ that is henceforth construed as the time coordinate. The Cagniard–DeHoop path has standardly the shape of two hyperbolic arcs. The TD solutions corresponding to those hyperbolic arcs are denoted as *body waves* and are associated to arrival times corresponding to the points where the arcs (or their analytic continuation) intersects the real, positive axis. However, depending on the specific expression of the slowness-domain expressions of the generalized-rays, the Cagniard–DeHoop path may intersect branch cuts along the real axis. The path must then be indented such that to circumvent those branch cuts. The TD solutions corresponding to those indentations are denoted as *head waves* and are also associated to arrival times corresponding to the intersections with the real, positive axis.

Appendix B

Causal Excitations

This appendix covers there different types of causal excitations including a power exponential (PE) pulse, a unipolar triangular pulse, and a windowed power (WP) pulse. The corresponding time-domain and spectral-domain expressions will be provided in the following subsections.

B.1 Power Exponential Pulse

The excitation signal applied in the wide slot configuration is a power exponential pulse [38, 44] illustrated by Fig. B.1. Its TD expression is given by

$$V_0(t) = V_{\max}(t')^{\nu}\exp[-\nu(t'-1)]H(t) \tag{B.1}$$

with $\nu = 0, 1, 2, ...$ in which $V_{\max}$ refers to the *pulse amplitude*, ν the *rising exponent* of the pulse, t' the time coordinate normalized to t_r and t_r the *pulse rise time*. The maximum value of $V_0(t)$ is obtained when $t = t_r$, or when $t' = 1$. The *pulse time width*, t_w, is calculated by

$$t_w = [(\nu-1)!/\nu^{\nu}]t_r\exp(\nu). \tag{B.2}$$

The expression of the power exponential pulse after the time-Laplace transform is

$$V_0(s) = \frac{V_{\max}}{t_r^{\nu}}\frac{\nu!}{(s+\nu/t_r)^{\nu+1}}\exp(\nu). \tag{B.3}$$

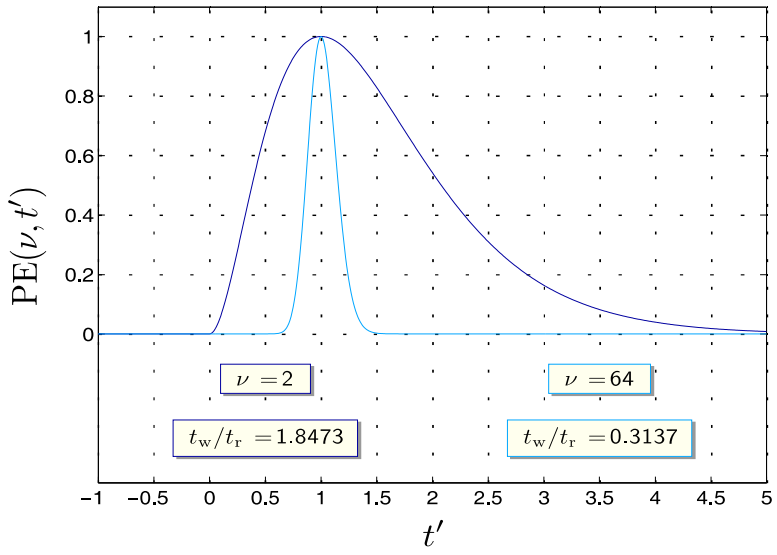

Figure B.1: Causal excitation: power exponential (PE) pulse.

In the spectral domain, it is expressed as

$$V_0(i\omega) = \frac{V_{\max}}{t_r^{\nu}} \frac{\nu!}{[\omega^2 + (\nu/t_r)^2]^{(\nu+1)/2}} \exp(\nu). \tag{B.4}$$

and following that, the corner frequency can be calculated by

$$\omega_{\text{corner}} = \nu/t_r. \tag{B.5}$$

B.2 Unipolar Triangular Pulse

The time domain expression of the unipolar triangular pulse from [48] shown in Fig. B.2 that was applied for the deconvolution is

$$V_0(t)/V_{\max} = \begin{cases} 0, & t < 0 \\ t', & 0 \le t \le t_r \\ 2 - t', & t_r < t \le t_w \\ 0, & t > t_w \end{cases} \tag{B.6}$$

where $V_{\max}$ denotes the *pulse amplitude*, t_w the *pulse time width* or the *base length*, $t_r = t_w/2$ the *pulse rise time*, and $t' = t/t_r = 2t/t_w$ refers to the normalized time coordinate. The maximum value is obtained if and only if $t = t_r$.

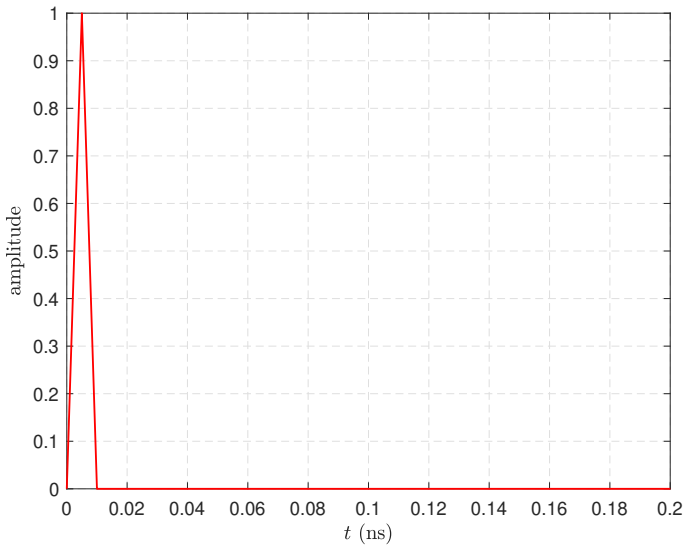

Figure B.2: Uni-polar triangular feeding pulse of unit amplitude with $t_{\mathrm{w}} = 0.01$ns.

The spectral domain expression of the triangular pulse is

$$V_0(s) = 1/(t_r s^2)[1–2\exp(-t_r s) + \exp(-2t_r s)] \tag{B.7}$$

with $s = j\omega = j2\pi f$. Therefore, it can also be written as

$$V_0(f) = -1/(2\pi f t_r)[1–2\exp(-j2\pi f t_r) + \exp(-j4\pi f t_r)] \tag{B.8}$$

which goes to zero when $f = n/t_r, n = 1, 2, 3....$

B.3 Windowed Power Pulse

As is shown in Fig. B.3, the windowed power (WP) pulse from [45] that was used to calculate the TD signatures (Impulse response) in Chapter 4 and 5 has the expression

$$V_0(t) = V_{\max}(t')^{\nu}(2 - t')^{\nu}H(t')H(2 - t') \tag{B.9}$$

in which $\nu = 2, 3, 4...$ is the pulse rising power, $V_{\max}$ is the *pulse amplitude*, t' is the time coordinate normalized to t_r, and t_r is the *pulse rise time*. Similarly, the maximum value

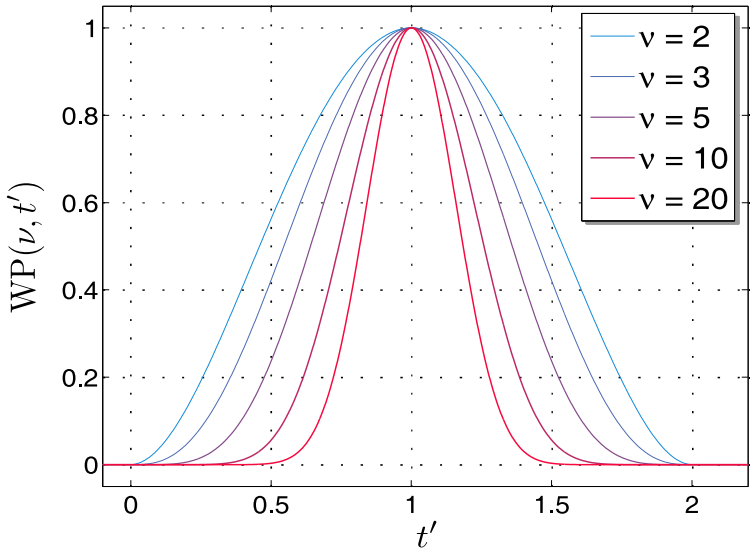

Figure B.3: Windowed power (WP) feeding pulses of unit amplitude with ν equal to different values.

of the WP pulse is obtained when $t = t_r$, or when $t' = 1$. The *pulse time width*, t_w is given by $t_w = 2t_r$.

The spectral domain expression of the WP pulse is given by

$$V_0(w) = \exp(-j\omega t_r) t_r 2^\nu \nu! \sqrt{2\pi} \frac{J_{\nu+1/2}(\omega t_r)}{(\omega t_r)^{\nu+1/2}} \tag{B.10}$$

where $\omega = 2\pi f$, f denotes the frequency, $J_{\nu+1/2}$ refers to the Bessel function of the first kind and fractional order [53].

Appendix C

MATLAB-based Analytical 2D Wide Slot Model

The MATLAB Code

```
function main_interface
close all; clear all;

% This file contains the main function for the fields at
% the interface for the pulsed electromagnetic field radiation
% from a wide slot antenna with a dielectric layer

% NOTE: the inverse square-root singularity is handled via
% the substitutions:
% τ = T_BW cosh(u)...BODY-WAVE CONTRIBUTIONS
% τ = T_BW cos(u)...HEAD-WAVE CONTRIBUTIONS

% Original Author: M. Stumpf
% Student: Junhong Gu
% Supervisor: Ioan Lager
% Date: 2009 August 20
% Revised: 2021 November 30
% Modified: 2022 Jan 6

% DEFINITION OF CONSTANTS
ep0 = 8.854*1e-12;              % electric permittivity of vacuum
mu0 = 4*pi*1e-7;                % magnetic permeability of vacuum
c0 = (ep0*mu0)^(-1/2);          % speed of light in vacuum
```

```
nu0 = (ep0/mu0)^(1/2);                % wave admittance of vacuum

global const;
const = struct('ep0',ep0,'mu0',mu0,'c0',c0,'nu0',nu0);

% DIELECTRIC SLAB PARAMETERS
ep1 = 4.0*ep0;                        % electric permittivity of slab
mu1 = mu0;                            % magnetic permeability of slab
c1 = (ep1*mu1)^(-1/2);                % speed of light in dielectric slab
nu1 = (ep1/mu1)^(1/2);                % wave admittance of dielectric slab
d = 5e-3;                             % dielectric slab thickness

global diel;
diel = struct('ep1',ep1,'mu1',mu1,'c1',c1,'nu1',nu1,...
    'd',d);

% HORIZONTAL SOURCE/FIELD POINT
% DISTANCE x1

global x1;


% VERTICAL SOURCE/FIELD POINT
% DISTANCE x3

global x3;

% SLOT WIDTH

global w;
w = 5.0e-3;

% REFERENTIAL TIMES

tnorm0 = d/c0;

% TIME PARAMETERS OF ANALYSIS

% tplot...time axis
% N...number of time points

Nt = 1001;
global tplot;
```

```
67  tplot = linspace(0,20.0*tnorm0,Nt);
68
69
70  % POWER-EXPONENTIAL PULSE
71
72  % Vmax...pulse amplitude
73  % power...rising exponent
74  % trise...pulse rise time
75  % ratio...pulse time width/pulse rise time
76  % tw...pulse time width
77
78  global Vmax;
79  Vmax = 1;
80  power = 2;
81  trise = 0.5*tnorm0;
82  ratio = power^(-power-1)*gamma(power+1)*exp(power);
83  tw = trise*ratio;
84
85  Pulse_version = 0; % Martin, original PE definition
86  % Pulse_version = 1;
87  global K;
88  if ( Pulse_version == 1 )
89     K = @(t) Vmax*PE_pulse_TD(trise,power,t);
90  elseif ( Pulse_version == 2 )
91     K = @(t) Vmax*WP_pulse_TD(trise,power,t);
92  elseif ( Pulse_version == 3 )
93     K = @(t) Vmax*dt_WP_pulse_TD(trise,power,t);
94  else
95     K = @(t) Vmax*exp(power)*((t/trise).^power).*exp(-(power/
           trise)*t).*(t>0);
96  end
97
98  % TIME DERIVATIVE OF POWER-EXPONENTIAL
99  % PULSE
100
101 global Kd;
102 if ( Pulse_version == 1 )
103    Kd = @(t) Vmax*dt_PE_pulse_TD(trise,power,t,0);
104 elseif ( Pulse_version == 2 )
105    Kd = @(t) Vmax*dt_WP_pulse_TD(trise,power,t,0);
106 elseif ( Pulse_version == 3 )
107    Kd = @(t) Vmax*d2t_WP_pulse_TD(trise,power,t);
108 else
```

```
109     Kd = @(t) Vmax*trise^(-power)*exp(power)*(power*t.^(power -
            1)...
110         - (power/trise)*t.^(power)).*exp(-(power/trise)*t).*(t
                >0);
111 end
112 %
113 clc;
114 %
115 %SOLUTION FOR THE CONFIGURATION
116 %WITH THE FINITE SLOT WIDTH
117
118 %NR...set of indices k (the reflections)
119 %Nw...number of weights in Gauss-Legendre
120 %quadrature
121
122 %CONFIGURATION WITH THE SLAB
123 %
124 Nw = 32;
125 %
126 NR = 0:1:4;
127 %
128 global N;
129 N = struct('NR',NR,'Nw',Nw);
130 %
131 %EVALUATION OF THE FIELDS AT THE INTERFACE
132 %
133 x3 = 1.0*d; x1 = 5*d;
134 [E1w, H2w] = SlabFiniteSlot_interface;
135 %
136
137 AE = load('E:\CST\txt_0.3334_delete\A_E.txt');
138 AH = load('E:\CST\txt_0.3334_delete\A_H.txt');
139 BE = load('E:\CST\txt_0.3334_delete\B_E.txt');
140 BH = load('E:\CST\txt_0.3334_delete\B_H.txt');
141 CE = load('E:\CST\txt_0.3334_delete\C_E.txt');
142 CH = load('E:\CST\txt_0.3334_delete\C_H.txt');
143 DE = load('E:\CST\txt_0.3334_delete\D_E.txt');
144 DH = load('E:\CST\txt_0.3334_delete\D_H.txt');
145
146 figure(1);
147 P1 = subplot(2,1,1);
148 plot(c0*tplot/d, H2w*sqrt(mu0/ep0)*w/Vmax,'b');
149 hold on
```

```
150 plot(DH(:,1)*60,DH(:,2)./max(DH(:,2))*max(H2w*sqrt(mu0/ep0)*w/
        Vmax))
151 hold off
152 grid on;
153 xlabel('Normalised Time')
154 ylabel('Normalised Magnetic Field')
155
156 P2 = subplot(2,1,2);
157 plot(c0*tplot/d, E1w*w/Vmax,'b');
158 hold on
159 plot(DE(:,1)*60,DE(:,2)*w/Vmax)
160 hold off
161 grid on;
162 xlabel('Normalised Time')
163 ylabel('Normalised Electric Field')
164 sgtitle('Normalised Fields at the Interface')
165 %
166
167 function [E1w,H2w] = SlabFiniteSlot_interface
168
169 % SOLUTION FOR THE CONFIGURATION
170 % WITH THE SLAB AND FINITE SLOT
171 % WIDTH
172
173 % SOLUTION FOR THE FIELDS AT INTERFACE. E3 COMPONENT
174 % IS NOT INCLUDED IN HERE, SINCE IS NOT CONTINUOUS
175 % ACROSS THE INTERFACE
176
177
178 % Original Author: M. Stumpf
179 % Student: Junhong Gu
180 % Supervisor: Ioan Lager
181 % Date: 2009 August 20
182 % Revised: 2010 November 2
183 % Modified: 2022 Jan 6
184
185 global const diel x1 tplot K N w;
186 %
187 ep0 = const.ep0;                % electric permittivity of vacuum
188 mu0 = const.mu0;                % magnetic permeability of vacuum
189 c0 = const.c0;                  % speed of light in vacuum
190 nu0 = const.nu0;                % wave admitance of vacuum
191 %
```

```
192 ep1 = diel.ep1;                    % electric permittivity of slab
193 mu1 = diel.mu1;                    % magnetic permeability of slab
194 c1 = diel.c1;                      % speed of light in dielectric slab
195 nu1 = diel.nu1;                    % wave admitance of dielectric slab
196 d = diel.d;                        % dielectric slab thickness
197 %
198 NR = N.NR;
199 Nw = N.Nw;
200 %
201 % FUNCTION HANDLES OF VERTICAL
202 % PROPAGATION PATH
203 % k...index
204 % hk...for the solution at interface
205 %
206 hk = @(k) (2*k + 1)*d;
207 %
208 % FUNCTION HANDLES FOR CONDITIONS
209 % OF EXISTENCE OF HEAD-WAVES
210 %
211 sinTH1 = @(k) ((x1-w/2)./sqrt((x1-w/2).^2 + hk(k).^2)).*((x1-w
        /2)>0);
212 % 1 represents the right side
213 sinTH2 = @(k) ((x1+w/2)./sqrt((x1+w/2).^2 + hk(k).^2));
214 % 2 represents the left side
215
216 % FUNCTION HANDLES OF TIME ARRIVALS
217 % OF BODY-WAVES (TBWx) AND HEAD-WAVES
218 % (THWx)
219
220 global TBW1;
221 TBW1 = @(k) sqrt((x1-w/2).^2 + hk(k).^2)/c1;
222 global TBW2;
223 TBW2 = @(k) sqrt((x1+w/2).^2 + hk(k).^2)/c1;
224 %
225 global THW1;
226 THW1 = @(k) (x1-w/2)/c0 + hk(k)*sqrt(c1.^(-2) - c0.^(-2));
227 global THW2;
228 THW2 = @(k) (x1+w/2)/c0 + hk(k)*sqrt(c1.^(-2) - c0.^(-2));
229
230 % PARAMETRIZATION OF BODY-WAVE PARTS
231 % OF CAGNIARD-DeHOOP PATHS
232
233 % subst.: \tau = T_{BW} \cosh(u)
```

```
234
235 pBW1 = @(u1,k) (x1-w/2)./((x1-w/2).^2 + hk(k).^2).*TBW1(k).*cosh(
        u1) + ...
236       1i*hk(k)./((x1-w/2).^2 + hk(k).^2).*TBW1(k).*sinh(u1);
237 %
238 pBW2 = @(u2,k) (x1+w/2)./((x1+w/2).^2 + hk(k).^2).*TBW2(k).*cosh(
        u2) + ...
239       1i*hk(k)./((x1+w/2).^2 + hk(k).^2).*TBW2(k).*sinh(u2);
240
241 % PARAMETRIZATION OF HEAD-WAVE PARTS
242 % OF CAGNIARD-DeHOOP PATH
243
244 % subst.: \tau = T_{BW} \cos(v)
245
246 pHW1 = @(v1,k) (x1-w/2)./((x1-w/2).^2 + hk(k).^2).*TBW1(k).*cos(
        v1) -...
247       hk(k)./((x1-w/2).^2 + hk(k).^2).*TBW1(k).*sin(v1) + 1i*1e
            -20;
248 %
249 pHW2 = @(v2,k) (x1+w/2)./((x1+w/2).^2 + hk(k).^2).*TBW2(k).*cos(
        v2) -...
250       hk(k)./((x1+w/2).^2 + hk(k).^2).*TBW2(k).*sin(v2) + 1i*1e
            -20;
251
252 % MAIN LOOP
253
254 H2w_HW = zeros(1,length(tplot));E1w_HW = zeros(1,length(tplot))
        ;
255 H2w_BW = zeros(1,length(tplot));E1w_BW = zeros(1,length(tplot))
        ;
256
257 % NUMBER OF HEAD-WAVES
258
259 global NH1;
260 NH1 = length(find((sinTH1(NR)/c1 > 1/c0)==1));
261 global NH2;
262 NH2 = length(find((sinTH2(NR)/c1 > 1/c0)==1));
263
264 for k = NR
265     IndHW1 = find(tplot >= THW1(k) & tplot < TBW1(k));
266     IndHW2 = find(tplot >= THW2(k) & tplot < TBW2(k));
267     %
268     indHW1 = find(tplot >= THW1(k));
```

```
269     indHW2 = find(tplot >= THW2(k));
270     %
271     indBW1 = find(tplot >= TBW1(k));
272     indBW2 = find(tplot >= TBW2(k));
273     %
274     if (sinTH1(k)/c1 > 1/c0)
275         %IF HEAD-WAVES EXIST, THEN...
276         acos_s = acos(tplot(IndHW1)/TBW1(k));
277         if ( length(acos_s) > 0 )
278         [weigths1, u1] = quadrM(acos(THW1(k)/TBW1(k)), acos_s,
                Nw);
279         %HEAD-WAVES (RIGHT EDGE)
280         weigths1 = - weigths1;
281         %DUE TO SUBSTITUTION: T_BW1 cos(u_1)
282         %
283         u1 = [u1 repmat(u1(:,end),[1 length(indHW1)-length(
                IndHW1)])];
284         %UPPER BOUND IS: min(t,T_BW1)
285         weigths1 = [weigths1 repmat(weigths1(:,end),[1 length(
                indHW1)-length(IndHW1)])];
286         %
287         gamma0 = sqrt(1/c0^2 - pHW1(u1,k).^2);
288         gamma1 = sqrt(1/c1^2 - pHW1(u1,k).^2);
289         %
290         RTM = (gamma1/ep1 - gamma0/ep0)./(gamma1/ep1 + gamma0/
                ep0);
291         TTM = (2*gamma1/ep1)./(gamma1/ep1 + gamma0/ep0);
292         argT =  repmat(tplot(indHW1),[Nw 1]) - TBW1(k)*cos(u1);
293         %
294         %H2-field (head-wave, right edge)
295         %
296         hlp = K(argT)...
297               .*imag((TTM.*RTM.^k)./pHW1(u1,k));
298         H2w_HW(indHW1) = H2w_HW(indHW1) + ...
299               (ep1/pi/w)*sum(weigths1.*hlp);
300         %
301         %E1-field (head-wave, right edge)
302         %
303         hlp = K(argT)...
304               .*imag((gamma0.*TTM.*RTM.^k)./pHW1(u1,k));
305         E1w_HW(indHW1) = E1w_HW(indHW1) + ...
306               (ep1/ep0/pi/w)*sum(weigths1.*hlp);
307         end
```

```
308         %
309     end
310     if (sinTH2(k)/c1 > 1/c0)
311         %IF HEAD-WAVES EXIST, THEN...
312         acos_s = acos(tplot(IndHW2)/TBW2(k));
313         if ( length(acos_s) > 0 )
314         [weigths2, u2] = quadrM(acos(THW2(k)/TBW2(k)), acos_s,
                Nw);
315         %HEAD-WAVES (LEFT EDGE)
316         weigths2 = - weigths2;
317         %DUE TO SUBSTITUTION: T_BW2*cos(u_2)
318         %
319         u2 = [u2 repmat(u2(:,end),[1 length(indHW2)-length(
                IndHW2)])];
320         %UPPER BOUND IS: min(t,T_BW2)
321         weigths2 = [weigths2 repmat(weigths2(:,end),[1 length(
                indHW2)-length(IndHW2)])];
322         %
323         gamma0 = sqrt(1/c0^2 - pHW2(u2,k).^2);
324         gamma1 = sqrt(1/c1^2 - pHW2(u2,k).^2);
325         %
326         RTM = (gamma1/ep1 - gamma0/ep0)./(gamma1/ep1 + gamma0/
                ep0);
327         TTM = (2*gamma1/ep1)./(gamma1/ep1 + gamma0/ep0);
328         %
329         argT =  repmat(tplot(indHW2),[Nw 1]) - TBW2(k)*cos(u2);
330         %
331         %H2-field (head-wave, left edge)
332         %
333         hlp = K(argT)...
334               .*imag((TTM.*RTM.^k)./pHW2(u2,k));
335         H2w_HW(indHW2) = H2w_HW(indHW2) - ...
336               (ep1/pi/w)*sum(weigths2.*hlp);
337         %
338         %E1-field (head-wave, left edge)
339         %
340         hlp = K(argT)...
341               .*imag((gamma0.*TTM.*RTM.^k)./pHW2(u2,k));
342         E1w_HW(indHW2) = E1w_HW(indHW2) - ...
343               (ep1/ep0/pi/w)*sum(weigths2.*hlp);
344         end
345         %
346     end
```

```
347         %
348         acos_s = acosh(tplot(indBW1)/TBW1(k));
349         if ( length(acos_s) > 0 )
350         %BODY-WAVES (RIGHT EDGE)
351         %
352         gamma0 = sqrt(1/c0^2 - pBW1(u1,k).^2);
353         gamma1 = sqrt(1/c1^2 - pBW1(u1,k).^2);
354         %
355         RTM = (gamma1/ep1 - gamma0/ep0)./(gamma1/ep1 + gamma0/ep0);
356         TTM = (2*gamma1/ep1)./(gamma1/ep1 + gamma0/ep0);
357         argT = repmat(tplot(indBW1), [Nw 1]) - TBW1(k)*cosh(u1);
358         %
359         %H2-field (body-wave, right edge)
360         %
361         hlp = K(argT)...
362               .*real((TTM.*RTM.^k)./pBW1(u1,k));
363         H2w_BW(indBW1) = H2w_BW(indBW1) + ...
364               (ep1/pi/w)*sum(weigths1.*hlp);
365         %
366         %E1-field (body-wave, right edge)
367         %
368         hlp = K(argT)...
369               .*real((gamma0.*TTM.*RTM.^k)./pBW1(u1,k));
370         E1w_BW(indBW1) = E1w_BW(indBW1) + ...
371               (ep1/ep0/pi/w)*sum(weigths1.*hlp);
372         end
373         %
374         %
375         acos_s = acosh(tplot(indBW2)/TBW2(k));
376         if ( length(acos_s) > 0 )
377         [weigths2, u2] = quadrM(0, acos_s,Nw);
378         %BODY-WAVES (LEFT EDGE)
379         %
380         gamma0 = sqrt(1/c0^2 - pBW2(u2,k).^2);
381         gamma1 = sqrt(1/c1^2 - pBW2(u2,k).^2);
382         %
383         RTM = (gamma1/ep1 - gamma0/ep0)./(gamma1/ep1 + gamma0/ep0);
384         TTM = (2*gamma1/ep1)./(gamma1/ep1 + gamma0/ep0);
385         argT = repmat(tplot(indBW2), [Nw 1]) - TBW2(k)*cosh(u2);
386         %
387         %H2-field (body-wave, left edge)
388         %
389         hlp = K(argT)...
```

```
390             .*real((TTM.*RTM.^k)./pBW2(u2,k));
391         H2w_BW(indBW2) = H2w_BW(indBW2) - ...
392             (ep1/pi/w)*sum(weigths2.*hlp);
393         %
394         % E1-field (body-wave, left edge)
395         %
396         hlp = K(argT)...
397             .*real((gamma0.*TTM.*RTM.^k)./pBW2(u2,k));
398         E1w_BW(indBW2) = E1w_BW(indBW2) - ...
399             (ep1/ep0/pi/w)*sum(weigths2.*hlp);
400     end
401 end
402 %
403 clear Weigths1 Weigths2 weigths1 weigths2 V1 V2 u1 u2;
404
405 % END OF MAIN LOOP
406
407 % ADDITIONAL FACTORS DUE TO
408 % THE FINITE WIDTH OF THE
409 % EXCITATION SLOT
410
411 TH0 = 2*nu0/(nu0 + nu1);
412 RH0 = (nu0 - nu1)/(nu0 + nu1);
413 %
414 for k = NR
415     if (abs(x1) < w/2)
416         H2w_BW = H2w_BW + nu1*TH0*(RH0)^k*K(tplot - hk(k)/c1)/w
                ;
417         E1w_BW = E1w_BW + (nu1/nu0)*TH0*(RH0)^k*K(tplot - hk(k)
                /c1)/w;
418     elseif (abs(x1) == w/2)
419         H2w_BW = H2w_BW + nu1*TH0*(RH0)^k*K(tplot - hk(k)/c1)/w
                /2;
420         E1w_BW = E1w_BW + (nu1/nu0)*TH0*(RH0)^k*K(tplot - hk(k)
                /c1)/w/2;
421     end
422 end
423 %
424 E1w = E1w_BW + E1w_HW;
425 H2w = H2w_BW + H2w_HW;
426 %
427
428 % Modified version of Gauss-Legendre integration method
```

```
% matched for the needs of Cagniard-DeHoop technique.

% Original version by:
% S. J. Orfanidis - 1999 - www.ece.rutgers.edu/ orfanidi/ewa

% Author of modification: M. Stumpf
% Date: 28 August 2009
% Revised: 29 August 2009

% a...lower bound of integration
% b...vector of the upper bounds
% N...number of weights

function [w,x] = quadrM(a,b,N)

if nargin==0, help quadr; return; end
if nargin==2, N=16; end

P = legendre(N,0);
% evaluate Legendre functions at x=0
m = (0:N)';
% coefficient index
P = (-1).^m .* P ./ gamma(m+1);
% order-N Legendre polynomial coefficients

z = sort(roots(flip(P)));
% sort roots in increasing magnitude

z = repmat(z, [1 length(b)]);
a = a*ones(1,length(b));
x = (z.*repmat((b-a), [N 1]) + repmat(a + b, [N 1]))/2;
% shifted Legendre roots

k = (0:N-1)';

c = (1 + (-1).^k) ./ (k+1);
% this is \int_{-1}^{1} t^k dt

A = [];
% coefficient matrix of the system A*w = c

for m=1:N,
    A = [A, z(m,1).^k];
```

```
472         % build the columns of A
473 end
474
475 w = repmat(A\c, [1 length(b)]) .* repmat((b-a)/2, [N 1]);
```

Appendix D

Propagation of the Waves in the Vicinity of a Planar Dielectric — Free-space Interface

D.1 Investigated configuration

This appendix covers the derivation of the head wave arrival times based on the ray trajectory shown in Fig. 3.2. To give a clearer interpretation on the head wave arrival times, the configuration and the ray trajectory of the head wave will be introduced here again. Let the configuration in Figure D.1.a consisting of a dielectric half-space with relative permittivity $\varepsilon_{\mathrm{r}} > 1$ and a free-space half-space interfacing in the $z = 0$ plane. The configuration is excited at the origin via a source $\mathcal{S}$ and the propagating field is examined at a field point $\mathcal{P}$ located at x and $z = h$. Apart from that, the value of γ in the two half-spaces can be calculated by $\gamma_{0,1} = (c_{0,1}^{-2} - p^2)^{1/2}$ with the slowness parameter $p = j\alpha$ [29].

From the electromagnetic (EM) field's spectral representation (see, *e.g.*, [29]), it can be inferred that the arrival time at $\mathcal{P}$ of the head wave (HW) τ_{HW} is

$$\tau_{\mathrm{HW}} = \frac{x}{c_0} + h(c_1^{-2} - c_0^{-2})^{\frac{1}{2}} = c_0^{-1}(x + h\sqrt{\varepsilon_{\mathrm{r}} - 1}) \tag{D.1}$$

in which $c_{0,1}$ are the wavespeeds in free-space (0) and the dielectric (1), and it was assumed, for simplicity, that $x > 0$ (otherwise one must use $|x|$ instead).

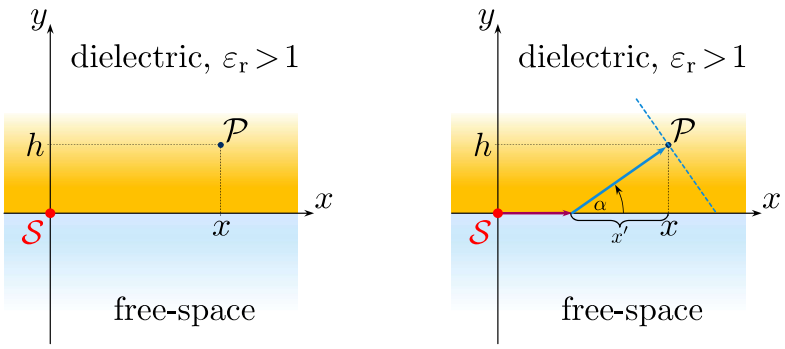

Figure D.1: Two-media configuration consisting of a dielectric half-space with relative permittivity $\varepsilon_r > 1$ and a free-space half-space. (a) Generic configuration; (b) ray representation of the HW reaching $\mathcal{P}$ - the cyan, dashed line represents the HW's front.

D.2 Physical interpretation of the HW

The physical interpretation of the HW is that of the first EM field disturbance propagating away from $\mathcal{S}$ that is sensed at $\mathcal{P}$. It must be stressed that HW can only be observed at field points located at angles that exceed the critical angle corresponding to the considered dielectric — vacuum interface. The path that this wave must follow is sketched in Fig. D.1.b. To understand this, one must recall that EM waves start from the source and travel in free-space at the wavespeed c_0 and in the dielectric at the wavespeed $c_1 = c_0/\sqrt{\varepsilon_r} < c_0$. The wave front propagating faster in the free-space will produce secondary sources at the interface which, in turn, will radiate spherical waves into the dielectric — those waves will reach some points in the dielectric before any wave propagating through the dielectric, only. Based on this reasoning, the HW is the wave that, combining propagation along the interface and through the dielectric, minimises the travel time between $\mathcal{S}$ and $\mathcal{P}$.

Based on the path in Fig. D.1.b, it can be stated that for a field point located at angles that exceed the critical angle, the time τ a wave needs to travel between $\mathcal{S}$ and $\mathcal{P}$ is

$$\tau = \frac{x - x'}{c_0} + \frac{\sqrt{\varepsilon_r}}{c_0}\sqrt{x'^2 + h^2} = \frac{1}{c_0}[(x - x') + \sqrt{\varepsilon_r}\sqrt{x'^2 + h^2}] = \frac{1}{c_0}\mathscr{F}(x') \tag{D.2}$$

The arrival time of the head wave can be obtained only if the first derivative of $\mathscr{F}(x')$ equals zero, when τ reaches its minimum value. By now taking the derivative of $\mathscr{F}(x')$ and equating it to zero, it is found that

$$\mathscr{F}(x') = -1 + \sqrt{\varepsilon_{\rm r}}\frac{x'}{\sqrt{x'^2 + h^2}} = \frac{-\sqrt{x'^2 + h^2} + \sqrt{\varepsilon_{\rm r}}x'}{\sqrt{x'^2 + h^2}} = 0 \tag{D.3}$$

this equation having the solution

$$x' = \frac{h}{\sqrt{\varepsilon_{\rm r} - 1}} \tag{D.4}$$

Substituting this quantity in (D.2) will yield the minimum time the wave takes from $\mathcal{S}$ and $\mathcal{P}$, namely

$$\tau_{min} = \frac{1}{c_0}[x - \frac{h}{\sqrt{\varepsilon_{\rm r} - 1}} + \sqrt{\varepsilon_{\rm r}}\sqrt{\frac{h^2}{\varepsilon_{\rm r} - 1} + h^2}] = \frac{1}{c_0}[x + h\sqrt{\varepsilon_{\rm r} - 1}] \tag{D.5}$$

which is the same expression as that in (D.1). In this manner, it was shown that the chosen path corresponds, indeed, to the path of the HW.

It should be observed that the direction in which the HW propagates through the dielectric is at the angle

$$\alpha = \arctan(\frac{h}{x'}) = \arctan(\sqrt{\varepsilon_{\rm r} - 1}) \tag{D.6}$$

in which (D.4) was used. Furthermore, the wavefront of the HW is formed by all points at which the HW arrives at the same time, which, from (D.1), corresponds to the line

$$z = -\frac{1}{\sqrt{\varepsilon_{\rm r} - 1}}x + \frac{c_0\tau_{\rm HW}}{\sqrt{\varepsilon_{\rm r} - 1}} \text{ for } z > 0 \tag{D.7}$$

that demonstrates (as expected) that the wavefront is orthogonal to the direction defined in (D.6).

D.3 Propagation of EM waves in the interval between the arrival of head and body waves

In the section above, it was shown that the HW path provides the fastest path for a disturbance to travel from $\mathcal{S}$ to $\mathcal{P}$ — this path is reproduced in Fig. D.2. The analysis also allowed inferring the orientation of the HW wave-front — that wave-front

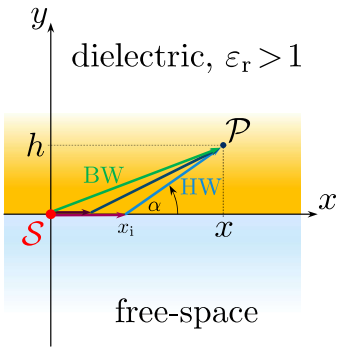

Figure D.2: Propagation paths from $\mathcal{S}$ to $\mathcal{P}$: "HW" stands for "HW path" = the fastest path for a disturbance to propagate from $\mathcal{S}$ to $\mathcal{P}$; "BW" stands for "BW path", the slowest path for a disturbance to propagate from $\mathcal{S}$ to $\mathcal{P}$.

was effectively evidenced in simulations of the instantaneous field distributions in the vicinity of $\mathcal{P}$.

The given physical interpretation clearly shows that other paths, comprising a shorter segment along the interface, will result in longer propagation times between $\mathcal{S}$ and $\mathcal{P}$ — an example of such a path is the one shown in dark plum and dark blue in Fig. D.2. The slowest path is the one of the waves travelling exclusively through the dielectric, namely the *bodywaves* (BW) — this path is marked in Fig. D.2 in green. Let us denote as τ_{BW} the arrival time of the first BW at $\mathcal{P}$.

Assume now that the feeding signal at $\mathcal{S}$ is not only causal (a requirement that is always pre-supposed) but also *continuous*. Such a feeding will then necessarily be just marginally non-vanishing immediately after its onset. As a result, it is clear that the signal level at the wave-front arriving at $\mathcal{P}$ at τ_{HW} must be extremely low. At subsequent instants $\tau_{\mathrm{HW}} + \Delta_t$, with $\Delta_t < \tau_{\mathrm{BW}} - \tau_{\mathrm{HW}}$, the effect of later (presumably, stronger) parts of the feeding signal will arrive at $\mathcal{P}$ via the HW path. Concomitantly, the effect of previous parts of the signal will also arrive at $\mathcal{P}$ via increasingly slow paths (akin to the intermediate path in Fig. D.2). Moreover, even the effect of secondary sources located at points *beyond* x_i along the interface may be sensed at $\mathcal{P}$. It is now evident that the aggregate field at $\mathcal{P}$ follows as the superposition of a multitude of propagating waves that are likely to produce both field enhancements and nulls. In any event, that aggregate effect contains no BW contributions.

This analysis demonstrates the complexity of the radiated EM field in the region preceding the arrival of the BW. The field modulation in the vicinity of the interface, without itself propagating, is bound to have an effect in the far-field.

Appendix E

MATLAB-based Deconvolution Tools

The MATLAB Code

```
1
2  clear all
3  close all
4  clc;
5
6  % Loading the CST data
7  data = load('E:\CST\C_tri_amp1.txt');
8  t = data(:,1)';
9  Ex = data(:,2)';
10
11 % Method 1: Laplace Transform Strategy
12
13 n = 1001;
14 dt = 0.5/(n-1);
15 Ex = dt*Ex;
16
17 kkk = 10;
18 t_m = linspace(0,0.5,n);
19
20 % Define the feeding Pulse
21 feed = zeros(1,n);
22 tw = kkk*dt;
23
```

```
for nn = 1:1001
    if t_m(nn) > 0 && t_m(nn) <= tw
        feed(nn) = 200*t_m(nn);
    elseif  t_m(nn) > tw && t_m(nn) <= 2*tw
        feed(nn) = -200*(t_m(nn) - 2*tw);
    end
end

% Integrations of the radiated field constituent Ex
int_Ex = cumtrapz(t,Ex);
sec_int_Ex = cumtrapz(t,int_Ex);

% Plot the feeding pulse
figure;
plot(t_m,feed)
xlabel('Time(ns)','Interpreter','latex');
ylabel('Amplitude','Interpreter','latex');
title('Feeding Pulse','Interpreter','latex')
grid on;box on;
xlim([0,0.2])

% Plot the radiated field constituent Ex
figure;
plot(t,Ex)
xlabel('Time(ns)','Interpreter','latex')
ylabel('E_x(t)','Interpreter','latex')
title('Electric Field Constituent $E_x$','Interpreter','latex')
grid on;box on;

% Second Time Integral
Green_Integral = zeros(1,1000);
yt = Ex;

for i = 0:100

    Green_Integral = Green_Integral + tw * (i+1) * yt;
    yt = [zeros(1,10), yt];
    yt = yt(1:1000);

end

% Second Time Derivative
Green_Integral = [0,Green_Integral,0];
```

```
67  Green_Derivative = diff(diff(Green_Integral))/(dt^2);
68  g_m = Green_Derivative(1:981);
69  g_m = [zeros(1,10),g_m];
70
71  % Plot the Green's function
72  figure;
73  plot(t(1:991),g_m)
74  xlabel('Time(ns)','Interpreter','latex')
75  ylabel('Amplitude','Interpreter','latex')
76  title('Green''s Function','Interpreter','latex')
77  grid on; box on;
78
79  % Smoothing the Green's function
80  mov_ave = movmean(g_m/dt,10);
81  mov_ave = movmean(mov_ave,10);
82  mov_ave = movmean(mov_ave,10);
83  mov_ave = movmean(mov_ave,10);
84
85  % Smoothing the CST result
86  mov_ave_cst = movmean(Ex,10);
87  mov_ave_cst = movmean(mov_ave_cst,10);
88
89  % Compare the smoothed Green's function with the smoothed Ex
90  figure;
91  plot(t(1:991),mov_ave,'r')
92  xlabel('Time(ns)','Interpreter','latex')
93  ylabel('Amplitude','Interpreter','latex')
94  title('Smoothed Green''s Function','Interpreter','latex')
95  grid on; box on;
96  xlim([0,0.2])
97
98  figure;
99  plot(t,mov_ave_cst)
100 xlabel('Time(ns)','Interpreter','latex')
101 ylabel('Amplitude','Interpreter','latex')
102 title('Smoothed Electric Field Constituent $E_x$','Interpreter'
        ,'latex')
103 grid on; box on;
104 xlim([0,0.2])
105
106 % Method 2: MATLAB in-built deconv function
107
108 feed(feed == 0) = [];
```

```
109 [g_d,r] = deconv(Ex,feed);
110 g_d(1) = [];
111 g_d = [zeros(1,10) g_d];
112
113 %Plot the Green's function
114 figure;
115 plot(t(1:991),g_d/dt)
116 xlabel('Time(ns)','Interpreter','latex')
117 ylabel('Amplitude','Interpreter','latex')
118 title('Green''s Function','Interpreter','latex')
119 grid on; box on;
120
121 %Smoothing the Green's function
122 mov_ave = movmean(g_d/dt,10);
123 mov_ave = movmean(mov_ave,10);
124 mov_ave = movmean(mov_ave,10);
125 mov_ave = movmean(mov_ave,10);
126
127 %Smoothing the CST result
128 mov_ave_cst = movmean(Ex,10);
129 mov_ave_cst = movmean(mov_ave_cst,10);
130
131 %Compare the smoothed Green's function with the smoothed Ex
132 figure;
133 plot(t(1:991),mov_ave,'r')
134 xlabel('Time(ns)','Interpreter','latex')
135 ylabel('Amplitude','Interpreter','latex')
136 title('Smoothed Green''s Function','Interpreter','latex')
137 grid on; box on;
138 xlim([0,0.2])
139
140 figure;
141 plot(t,mov_ave_cst)
142 xlabel('Time(ns)','Interpreter','latex')
143 ylabel('Amplitude','Interpreter','latex')
144 title('Smoothed Electric Field Constituent $E_x$','Interpreter'
    ,'latex')
145 grid on; box on;
146 xlim([0,0.2])
```

Appendix F

Deconvolution Strategy: Laplace Transform Method

The basic idea is to first convert the integral equation using the standard Laplace Transform and from the equation in the S-domain.

$$y(t) = \int_{-\infty}^{\infty} x(\tau)\Delta(t-\tau)d\tau \tag{F.1}$$

$$Y(s) = X(s)\Delta(s) \tag{F.2}$$

$$X(s) = \frac{Y(s)}{\Delta(s)} \tag{F.3}$$

The triangular pulse in the time domain and in the s domain can be expressed as

$$\Delta(t) = \frac{1}{t_\mathrm{r}}t\mathrm{H}(t) - \frac{2}{t_\mathrm{r}}(t-t_\mathrm{r})\mathrm{H}(t-t_\mathrm{r}) + \frac{1}{t_\mathrm{r}}(t-2t_\mathrm{r})\mathrm{H}(t-2t_\mathrm{r}) \tag{F.4}$$

$$\Delta(s) = \frac{1}{t_\mathrm{r}}\frac{1}{s^2} - \frac{2}{t_\mathrm{r}}\exp(-t_\mathrm{r}s)\frac{1}{s^2} + \frac{1}{t_\mathrm{r}}\exp(2t_\mathrm{r}s)\frac{1}{s^2} \tag{F.5}$$

$$\Delta(s) = \frac{1}{t_\mathrm{r}}\frac{1}{s^2}[1 - 2\exp(-t_\mathrm{r}s) + \exp(-2t_\mathrm{r}s)] \tag{F.6}$$

Therefore, $X(s)$ can be written as

$$X(s) = \frac{Y(s)s^2t_\mathrm{r}}{[1-\exp(-st_\mathrm{r})]^2} \tag{F.7}$$

The expression of $X(s)$ can be expanded by a convergent geometric series.

$$\frac{1}{(1-x)^2} = 1 + 2x + 3x^2 + 4x^3 + ... \tag{F.8}$$

$$\frac{X(s)}{s^2} = Y(s)t_\mathrm{r}[1 + 2\mathrm{exp}(-st_\mathrm{r}) + 3\mathrm{exp}(-2st_\mathrm{r}) + 4\mathrm{exp}(-3st_\mathrm{r}) + ...] \tag{F.9}$$

Finally, an inverse Laplace Transform is performed, which yields the final deconvolution equation.

$$\partial_t^{-2}x(t) = t_\mathrm{r}\sum\nolimits_{n=0}^{\infty}(n+1)y(t-nt_\mathrm{r}) \tag{F.10}$$

$$x(t) = \partial_t^2[\partial_t^{-2}x(t)] = \partial_t^2[t_\mathrm{r}\sum\nolimits_{n=0}^{\infty}(n+1)y(t-nt_\mathrm{r})] \tag{F.11}$$

Note that, in the equations above, $x(t)$ denotes the time domain green function, $y(t)$ represents the time domain radiated field $E_x(t)$, and $\Delta(t)$ represents the excitation triangular pulse with a pulse width of t_w.